

Crystal Growth and Investigation of CeCu_2Si_2 and
 YbRu_2Ge_2 : Competition/Co-existence of
Superconducting, Dipolar and Quadrupolar order

Dissertation

zur Erlangung des akademischen Grades

Doctor rerum naturalium

(Dr. rer. nat.)

vorgelegt

der Fakultät Mathematik und Naturwissenschaften
der Technischen Universität Dresden

von

Hirale S. Jeevan

geboren am 23. July 1973, in Shimoga, India

MAX-PLANCK INSTITUT FÜR CHEMISCHE PHYSIK FESTER STOFFE
DRESDEN, 2010

Table of Contents

Table of Contents	1
Abstract	3
1 Introduction to f-electron physics	1
1.1 Kondo effect and Ruderman-Kittel-Kasuya-Yosida interaction	2
1.2 Heavy-fermion systems	6
1.3 Crystal-electric-field effects	8
Bibliography	11
2 Single crystal growth of $\text{CeCu}_2(\text{Si}_{1-x}\text{Ge}_x)_2$ and YbRu_2Ge_2 systems	14
2.1 Introduction	14
2.2 Bridgman method	15
2.3 Synthesis of YbRu_2Ge_2	25
2.4 Experimental methods	28
Bibliography	31
3 Magnetism and superconductivity in CeCu_2Si_2	33
3.1 Introduction	33
3.2 Different physical ground states in CeCu_2Si_2	37
3.2.1 A-type CeCu_2Si_2	37
3.2.2 AS-type CeCu_2Si_2	49
3.2.3 SA-type CeCu_2Si_2	58
3.2.4 S-type CeCu_2Si_2	63
3.3 Discussion	72
3.4 Conclusions	87

Bibliography	89
4 Evolution of magnetism and superconductivity in $\text{CeCu}_2(\text{Si}_{1-x}\text{Ge}_x)_2$	93
4.1 Introduction	93
4.2 $\text{CeCu}_2(\text{Si}_{0.98}\text{Ge}_{0.02})_2$	95
4.3 $\text{Ce}_y\text{Cu}_2(\text{Si}_{0.9}\text{Ge}_{0.1})_2$	104
4.4 Discussion and Conclusions	113
Bibliography	117
5 Magnetic and Quadrupolar ordering in YbRu_2Ge_2	120
5.1 Introduction	120
5.2 Sample preparation	124
5.3 Physical properties	126
5.3.1 Magnetic susceptibility of YbRu_2Ge_2	126
5.3.2 Specific heat of YbRu_2Ge_2	136
5.3.3 Resistivity of YbRu_2Ge_2	145
5.4 Investigation of YbRu_2Ge_2 with μSR and Neutron scattering	153
5.4.1 Zero field muon spin measurements	153
5.4.2 Neutron diffraction	161
5.4.3 Inelastic Neutron Scattering	165
5.5 Discussion and Conclusion	171
Bibliography	175
6 Summary and Conclusions	179
Acknowledgements	184

Abstract

Strongly correlated systems represent one of the major topics in modern solid-state physics. The rare-earth intermetallic compounds belonging to this class provide rich grounds for investigation of various phenomena. They show one of the most fascinating types of ground states in condensed-matter physics. Among them are: Kondo-lattice effects, heavy fermion behavior, superconductivity, magnetic order, non-Fermi liquid behavior, and quantum phase transition. Those properties occur mainly due to two competing interactions, the Kondo effect and the Ruderman-Kittel-Kasuya-Yosida interaction.

The study of unconventional superconductivity in heavy fermion systems attracted great interest over the last two decades. The exotic pairing mechanism (e.g. mediated by spin fluctuations) and the symmetry of the order parameter have been intensively discussed especially for superconducting Ce- and U-based compounds. The discovery of superconductivity below 0.65 K in the heavy-electron system CeCu_2Si_2 appeared unexpected as magnetic moments were known to destroy superconductivity. The pronounced anomaly of the electronic specific heat at T_c , however, strongly suggests that the unusual low temperature properties of heavy-electron systems indicate an unconventional origin of the superconducting phase. Since the discovery of superconductivity in CeCu_2Si_2 , the question of the exact nature and origin of this phenomenon has been the subject of great interest in research. It has been postulated, that the superconductivity in these materials is not caused primarily by the usual electron-phonon mechanism but rather by some magnetic interaction. CeCu_2Si_2 shows a rich phase diagram with different phases competing, depending on slight changes of the

interactions. These properties are also strongly sample dependent. Small changes in composition eventually lead to changes in the electron interactions. These unique properties make this compound a fascinating subject of study. On the other hand it is difficult to synthesis the single crystals with defined physical properties. During the last three decades CeCu_2Si_2 has been an active research topic, from single crystal growth to sophisticated experiments like high-pressure measurements, neutron experiments etc. This thesis involved systematic investigations of the phase diagram, starting with the single crystal growth of different ground state and catheterized their physical properties including neutron experiments. The second part of the thesis contains, for the first time (to our knowledge), detailed investigations of the very interesting physical properties on YbRu_2Ge_2 , which shows a quasi-quartet crystal-electric-field ground state with quadrupolar ordering at 10 K.

The first chapter is an overview of the underlying physics of heavy-fermion systems, including a description of the Doniach phase diagram. The second part of this chapter gives a brief introduction of crystalline-electric-field effect in rare-earth intermetallic compounds. Chapter 2. describes the experimental methods and crystal growth details. This chapter provides the main focus of this dissertation, presenting detailed experimental results for the different types of CeCu_2Si_2 crystals. Magnetic, thermodynamic and transport measurements on the new generation of large high-quality single crystals were conducted by our research group. Furthermore, complimentary neutron investigations have been performed, which allowed to conclude that both magnetic and superconducting phases compete with each other. The effect of Ge doping on the Si site and possible coexistence of magnetic and superconducting phase is discussed in chapter 4. Chapter 5 provides a detailed investigation of the physical properties of YbRu_2Ge_2 single crystals. In addition, neutron experiments as well as the determination the magnetic structure and crystalline-electric-field scheme of YbRu_2Ge_2 are presented. The μSR experiments were also performed as a complimentary method to the neutron experiments. Chapter 6 ends the dissertation with a conclusion and summary.

Chapter 1

Introduction to f-electron physics

Electronic correlations which occur due to many-body effects can cause interesting phenomena such as electronic localization, magnetism, and charge ordering. Different types of strongly correlated systems are at the forefront of experimental and theoretical research in condensed matter physics, e.g. high-temperature superconductors, heavy-fermion systems, manganites, ruthenates and vanadates. Among those, heavy-fermion compounds play a major role in current research. CeAl_3 was the first reported heavy-fermion compound based on its unusual low-temperature specific heat [1] with a Sommerfeld coefficient of 1500 mJ/mol.K^2 and sparked strong interest in heavy-fermion materials. This behavior predominantly occurs in compounds with elements with partially filled 4f and 5f electrons, since the 4f- and 5f-electrons can switch from localized to delocalized states. The discovery of heavy-fermion superconductivity in CeCu_2Si_2 in 1979 [2] was the decisive step which established these systems at the core of strongly correlated physics. Heavy-fermion superconductivity has meanwhile been observed in several Cerium [3, 4, 5, 6], Praseodymium [7], Uranium [8,9], and has recently been discovered in Plutonium [10] and Ytterbium [11] compounds as

well. Nevertheless, the nature and the mechanism of heavy-fermion superconductivity are still not settled. The physics of heavy-fermion is caused by two main effects: The Kondo effect [12,13] with a tendency to screen the moments and produce a non-magnetic ground state and the Ruderman-Kittel-Kasuya-Yosida interaction [14, 15, 16] which favors long-range magnetic order.

1.1 Kondo effect and Ruderman-Kittel-Kasuya-Yosida interaction

The Kondo effect was observed for a single magnetic impurity in a non-magnetic metallic host. Below a characteristic temperature, the so-called Kondo temperature, a strong coupling occurs between the magnetic impurity and the conduction electrons leading to the disappearance of the local magnetism. The coupling of the localized spin \vec{S} and the spin of the conduction electron \vec{s} can be reduced to an exchange term given by the Hamiltonian:

$$H = -J\vec{S}\cdot\vec{s} \quad (1.1.1)$$

where J is the coupling term between the local spin and the conduction electrons. The Kondo temperature T_K is the temperature where a spin-singlet state forms through the antiferromagnetic coupling between the conduction electrons and the localized spins. It is related to the coupling term J and to the density of states of the conduction electrons $N(E_F)$ at the Fermi level.

$$k_B T_K \simeq 1/N(E_F)\exp(-1/JN(E_F)) \quad (1.1.2)$$

The physical properties can be described within the Fermi-liquid theory with strongly renormalized parameters. The large density of states is reflected in an enhanced mass of the heavy quasiparticles. For $T \rightarrow 0$ K, the specific heat, C , the susceptibility, χ , and the resistivity, ρ , vary as:

- The Sommerfeld coefficient γ of the electronic specific heat $\Rightarrow \gamma = C_{el}/T \sim 1/T_K$
- Susceptibility $\Rightarrow \chi \simeq 1/T_K$
- Resistivity $\Rightarrow \rho = \rho_0(1 - a[T/T_K]^2)$

One can expand the concept of the Kondo-impurity effect to the Kondo-lattice effect by placing a magnetic ion at every lattice site. In the Kondo lattice, magnetic ions are no longer impurities. The Kondo-lattice Hamiltonian can then be described as follows:

$$H = \sum_{k\sigma} \epsilon_{k\sigma} c_k \epsilon^\dagger c_{k\sigma} + (2J/N) \sum_i \vec{s}_i \vec{S}_i \quad (1.1.3)$$

The first term is the kinetic energy of conduction electrons and the second term is the exchange interaction between conduction electrons and the localized spins. $\epsilon_{k\sigma}$, $c_{k\sigma}^\dagger$ and $c_{k\sigma}$ are the conduction electron energy, the creation operator of a conduction electron with spin σ and the annihilation operator of a conduction electron with spin σ , respectively.

The Ruderman-Kittel-Kasuya-Yosida (RKKY) exchange interaction between localized magnetic impurities embedded in a host metal has played an important role in the theory of magnetism. The magnetic moment of one impurity scatters the conduction electrons, which are then seen by a different impurity. It is an indirect exchange

interaction which couples moments over relatively large distances. The RKKY exchange interaction dominates in rare-earth metals where little or no direct overlap between neighboring magnetic f-electrons appears. The RKKY interaction is the basic ingredient for many phenomena in heavy-fermions systems. The interaction is characterized by an energy scale, given by

$$k_{\text{B}}T_{\text{RKKY}} \simeq J^2N(E_{\text{F}}) \quad (1.1.4)$$

where J is the same exchange term as introduced for the Kondo interaction and k_{B} is the Boltzmann constant. The heavy-fermion systems are governed by the interplay of the two energy scale; the Kondo scale and the RKKY interaction. Both scales depend on the strength of the exchange coupling, the density of conduction electrons, and the dimensionality of the lattice. While the Kondo effect tends to compensate the localized spin, the RKKY interaction develops magnetic order between the localized spins. The competition of these two interaction leads to the popular Doniach diagram (Fig.1.1) [17].

This diagram (in an extended version of original Doniach diagram) displays the variation of the RKKY interaction and of the Kondo temperature with increasing J . The resulting ordering temperature T_{N} grows initially with increasing J , then passes through a maximum and is eventually suppressed to zero at a critical value J_{c} corresponding to a "quantum critical point" (QCP). This kind of behavior of T_{N} has been experimentally observed with increasing pressure or chemical doping in many cerium compounds.

For J values smaller than the value J_{c} , the compounds are in a magnetically ordered state. For Ce and Yb-based compounds, the magnetic ordering temperature

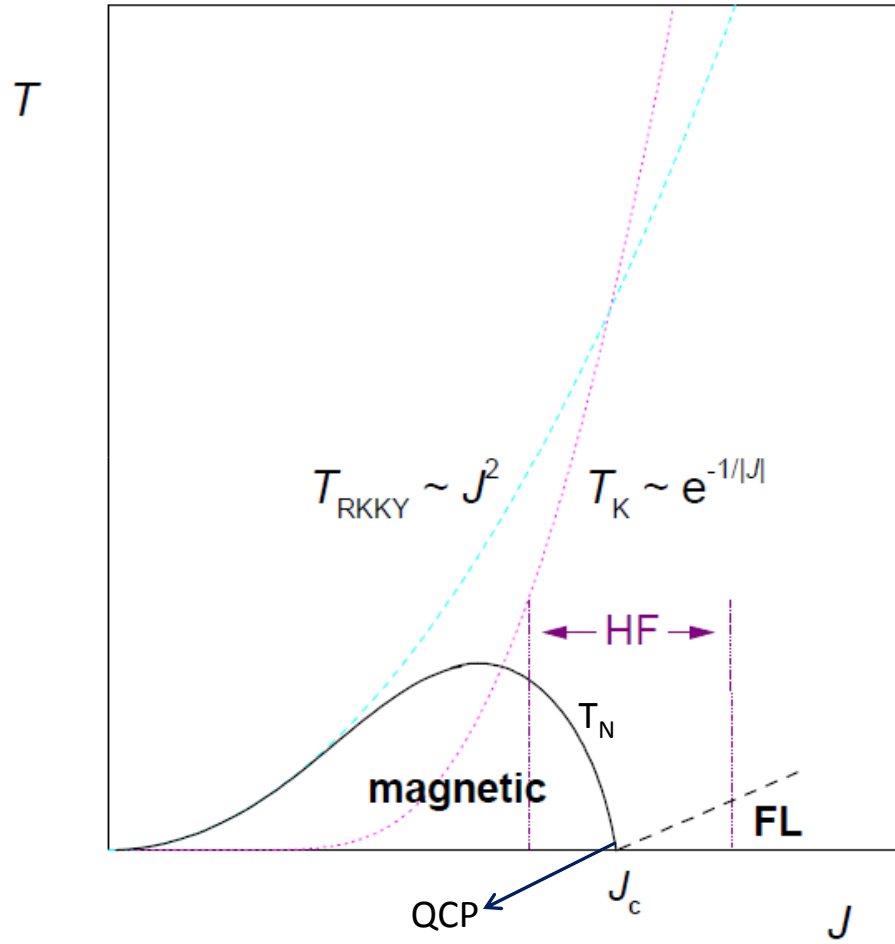


Figure 1.1: Extended Doniach phase diagram (FL = Fermi liquid, HF = heavy-fermion). The dotted lines represent T_{RKKY} (blue) and T_K (red). The full line represents the ordering temperature T_N and the dashed line the temperature below which FL behavior is expected [17].

is of the order of 2 K to 20 K and 1 K to 5 K, respectively. They present heavy-fermion character only in the vicinity of J_c . For $J > J_c$, the compounds are paramagnetic and can exhibit a very strong heavy-fermion character with a Sommerfeld coefficient γ in the order of 1 J/(mol.K²). The coupling term J might be tuned by the application of hydrostatic pressure. In the case of Ce-based heavy-fermion systems, the magnetic Ce³⁺ state is destabilized upon applying pressure since its volume is smaller than that of the non-magnetic Ce⁴⁺ ion. By contrast, the magnetic Yb³⁺ state is favored over the non-magnetic Yb²⁺ with pressure. Thus, pressure stabilizes the Kondo effect (large J) in Ce compounds whereas it yields magnetic ordering (small J) for Yb systems.

1.2 Heavy-fermion systems

The heavy-fermion state corresponds to one possible type of ground states of Kondo-lattice systems. The term heavy-fermion originates from the huge increase of the Sommerfeld coefficient γ of the electronic specific heat at low temperatures. The specific heat coefficient is proportional to the effective electron mass and the density of states. This huge increase of γ results from the Kondo resonance. When conduction electrons interact with a scattering potential which is not sufficiently attractive to produce a bound state below the conduction band, they tend to be localized only for a short time in the vicinity of the scattering center. This resonant scattering induces a narrow peak in the conduction-band density of states very close to the Fermi energy. As a result the specific heat coefficient and the Pauli paramagnetic susceptibility are enhanced below the characteristic Kondo temperature T_K . The scattering

amplitudes from the Kondo ions start to superimpose coherently according to the periodicity of the crystallographic lattice below the so-called "coherence temperature". As Bloch-wave states of Kondo scatterers form below the coherence temperature a strong decrease of the resistivity is observed at low temperatures. Well below the coherence temperature, the resistivity usually shows a Fermi-liquid behavior: $\rho = \rho_0 + AT^2$. The coefficient A is related to the electronic specific heat coefficient through the Kadowaki-Wood relation, i.e. $A \propto \gamma^2$. Since heavy-fermion systems have huge γ values, the coefficient A also exceeds that of simple metals by several orders of magnitude.

Most low- T properties of paramagnetic heavy-fermion systems are found to be in good agreement with Landau's Fermi-liquid theory. However, a new class of compounds has emerged in recent years whose physical properties at low temperatures show remarkable deviations from the Fermi-liquid theory, and are therefore called "non-Fermi liquid" (NFL) systems. NFL behavior in f-electron systems is characterized by weak power-law or logarithmic temperature dependences of the physical properties at low temperatures as follows

$$\text{Resistivity: } \rho = \rho_0(1 + aT^n), n \simeq 1 - 1.5$$

$$\text{Electronic specific heat: } C_{\text{el}}/T \simeq bT^{(-m)}, 0 < m < 1$$

$$\text{Susceptibility: } \chi \simeq cT^{(-k)}$$

NFL behavior is often observed to occur near a second-order phase transition that has been suppressed to zero by pressure, chemical substitution or magnetic field. A wide variety of f-electron materials display NFL behavior, e. g., CeCu_2Si_2 , CeRhIn_5 , YbRh_2Si_2 , $\text{CeCu}_{6-x}\text{Au}_x$.

1.3 Crystal-electric-field effects

One of the main factors responsible for the considerable anisotropy of the magnetic properties in compounds with rare-earth metals is the effect of the crystal-electric field on the 4f electron shell of rare-earth ions. Magnetic properties of rare-earth intermetallics result to a large extent from the interplay of crystalline-electric-field (CEF) and exchange interactions. The CEF removes the degeneracy of the ground state multiplet of the rare-earth ion. This results in specific magnetic properties of the corresponding compound. When the rare-earth ion has an even number of 4f electrons, the lowest level of the ground state multiplet is in particular cases a singlet. In this case, the rare earth ion may behave like a nonmagnetic ion. Therefore, the study of CEF effects is an important subject in the field of rare-earth magnetism.

The 4f electrons of a rare-earth ion in a solid are well localized, but nevertheless experience an electrostatic potential that originates from the surrounding charge distribution. The CEF Hamiltonian, describing the electrostatic interaction of the aspherical 4f charge distribution with the aspherical electrostatic field arising from its surrounding, can be written as

$$H_{CEF} = - \sum_{i=1}^{nf} eV(r_i) \quad (1.3.1)$$

where $V(r_i)$ is the electrostatic potential due to the surrounding ions at the location r_i of the 4f electron i . The most convenient way to deal with this Hamiltonian is to expand it in spherical harmonics Y_m^n .

$$H_{CEF} = - \sum_{n=0}^{\infty} \sum_{m=-n}^n A_n^m \sum_{i=1}^{nf} r_i^n Y_n^m(\theta_i \varphi_i) \quad (1.3.2)$$

where A_m^n are coefficients of this expansion and regarded as the structural CEF parameters. Their values depend only on the crystal structure and determine the strength of the CEF interaction. n is a positive number restricted to the range $n \leq 2J$, where J is the total angular momentum of the ion. The calculation of the matrix elements of the Hamiltonian (1.12) can be performed by direct integration. However, the technique called the Stevens operator equivalent method is much more convenient and is widely used. This method by Stevens [18] is described in detail by Hutchings [19]. In this method, the x ; y ; z coordinates of a particular electron are replaced by the components J_x , J_y , J_z of the multiplet of J . The CEF Hamiltonian (1.12) then takes the form

$$H_{CEF} = - \sum_{n=0}^{2J} \sum_{m=-n}^n B_n^m O_n^m(J) \quad (1.3.3)$$

Here, the coefficients B_m^n are called the CEF parameters and O_m^n are the Stevens equivalent operators, which have all been tabulated [18]. CEF interactions have been analyzed for many compounds. The situation becomes increasingly more complex for systems with low crystal symmetry. For cubic symmetry the CEF can be described by only two parameters B_4 and B_6

$$H_{CEF} = B_4(O_4^0 + 5O_4^0) + B_6(O_6^0 - 21O_6^4) \quad (1.3.4)$$

For tetragonal symmetry in general, five CEF parameters B_m^n are needed

$$H_{CEF} = B_2^0 O_2^0 + B_4^0 O_4^0 + B_4^4 O_4^4 + B_6^0 O_6^0 + B_6^4 O_6^4 \quad (1.3.5)$$

However for Ce ions the sixth order parameter is zero. These CEF parameters B_m^n are usually evaluated from the analysis of experimental data. The method includes fitting the magnetization curves, inelastic neutron scattering spectra, and the

temperature dependence of the specific heat or of the susceptibility.

Bibliography

- [1] K. Andres, J. E. Graebner, and H. R. Ott, *Phys. Rev. Lett.* **35**, 1779 (1975).
- [2] F. Steglich, J. Aarts, C. D. Bredl, W. Lieke, D. Meschede, W. Franz and H. Schäfer, *Phys. Rev. Lett.* **43**, 1982 (1979).
- [3] C. Petrovic, P. G. Pagliuso, M. F. Hundley, R. Movshovich, J. L. Sarrao, J. D. Thompson, Z. Fisk, and P. Monthoux, *J. Phys.: Condens. Matter* **13**, L337 (2001).
- [4] H. Hegger, C. Petrovic, E. G. Moshopoulou, M. F. Hundley, J. L. Sarrao, Z. Fisk, and J. D. Thompson, *Phys. Rev. Lett.* **84**, 4986 (2000).
- [5] N. D. Mathur, F. M. Grosche, S. R. Julian, I. R. Walker, D. M. Freye, R. K. W. Haselwimmer, G. G. Lonzarich, *Nature* **394**, 39 (1998), I. R. Walker, F. M. Grosche, D. M. Freye, G. G. Lonzarich, *Physica C* **282**, 303 (1997).
- [6] D. Kaczorowski, A. P. Pikul, D. Gnida, and V. H. Tran. *Phys. Rev. Lett.* **103**, 027003 (2009).
- [7] M. B. Maple, E. D. Bauer, V. S. Zapf, E. J. Freeman, N. A. Frederick, R. P. Dickey, *Acta Physica Polonica B* **32**, 3291 (2001).

- [8] H. R. Ott, H. Rudigier, Z. Fisk, and J. L. Smith: Phys. Rev. Lett. **50**, 1595 (1983), R. A. Fisher, S. Kim, B. Woodfield, N. E. Phillips, L. Taillefer, K. Hasselbach, J. Flouquejt, A.L. Giorgia and J.L. Smith, Phys. Rev. Lett. **62**, 1411 (1989), M. B. Maple, J. W. Chen, Y. Dalichaouch, T. Kohara, C. Rossel, M.S. Torikachvili, M.W. McElfresh, J. D. Thompson, Phys. Rev. Lett. **56**, 185 (1986), S. Adenwalla, S. W. Lin, Q. Z. Ran, Z. Zhao, J. B. Ketterson, J. A. Sauls, L. Taillefer, D. G. Hinks, M. Levy, and B. K. Sarma, Phys. Rev. Lett. **65**, 2298 (1990).
- [9] C. Geibel, C. Schank , S. Thies, K. Kitazawa, C. D. Bredl, A. Boehm, M. Rau , A. Grauel, R. Caspari, R. Helfrich, U. Ahlheim, G. Weber and F. Steglich, Z. Phys. B **84**, 1 (1991).
- [10] J. L. Sarrao, L. A. Morales, J. D. Thompson, B. L. Scott, G. R. Stewart, F. Wastin, J. Rebizant, P. Boulet, E. Colineau and G. H. Lander, Nature **420**, 297 (2002).
- [11] S. Nakatsuji, K. Kuga , Y. Machida, T. Tayama, T. Sakakibara, Y. Karaki, H. Ishimoto, S. Yonezawa, Y. Maeno, E. Pearson, G. G. Lonzarich, L. Balicas, H. Lee and Z. Fisk, Nature Physics **4**, 603 (2008).
- [12] J. Kondo, Prog. Theor. Phys. **32**, 37 (1964) .
- [13] B. Coqblin, C. Lacroix, M. A. Gusmão, J. R. Iglesias, Phys. Rev. B **67**, 064417 (2003).
- [14] M. A. Ruderman and C. Kittel, Phys. Rev. **96**, 96 (1954).
- [15] T. Kasuya, Prog. Theor. Phys. **16**, 45 (1956).

- [16] Yosida, Phys. Rev. **106**, 893 (1957).
- [17] S. Doniach, Physica B **91**, 231 (1977).
- [18] K. W. H. Stevens, Proc. Phys. Soc. A **65**, 209 (1952).
- [19] M. T. Hutchings, Solid State Phys. **16**, 227 (1964).

Chapter 2

Single crystal growth of $\text{CeCu}_2(\text{Si}_{1-x}\text{Ge}_x)_2$ and YbRu_2Ge_2 systems

2.1 Introduction

Heavy-fermion systems are generally intermetallic compounds containing unstable f-shell elements like Cerium, Ytterbium and Uranium etc. These compounds show anomalous low temperature properties like a large electronic specific heat coefficient, a large Pauli paramagnetic susceptibility, non-Fermi-liquid behavior, quantum phase transitions, and unconventional superconductivity. In order to study these properties it is important to possess samples of very good quality. High crystal purity is essential since some of these properties, like e.g. superconductivity, are extremely sensitive to actual composition, impurity phase and defects. Furthermore, large single crystals are desired for some specific investigations like neutron experiments.

The techniques used for crystal growth depend strongly on the compounds, e.g., on its thermal properties and on the related solid-liquid-vapor phase diagram. Crystals can be grown by a variety of different methods, e.g., growth from the melt, solution,

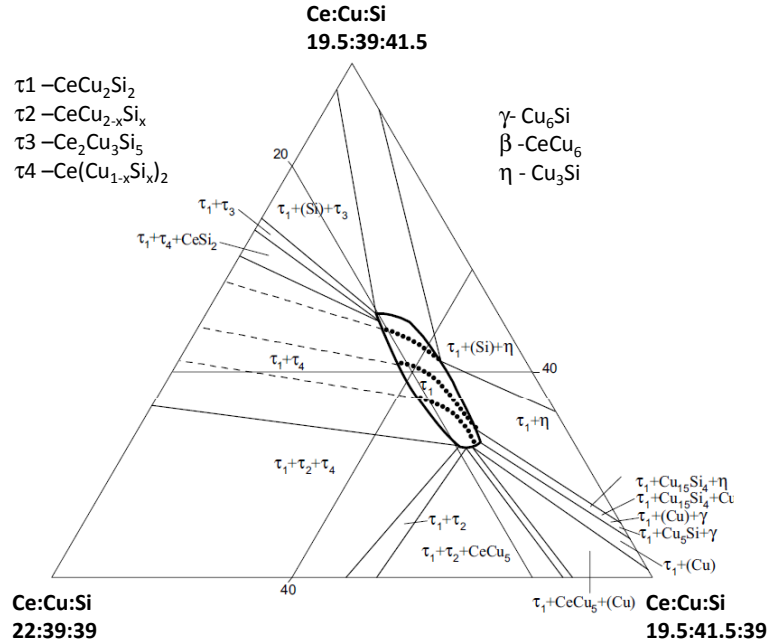


Figure 2.1: Partial ternary phase diagram of Ce-Cu-Si, part marked with τ_1 shows the homogeneity region of CeCu_2Si_2 [6].

vapor, and from the solid state. Crystal growth from the melt is the most widely used method for preparation of large single crystals. In the present work a combination of Bridgman and flux method for growing Ce and Yb based compounds has been applied.

2.2 Bridgman method

The investigation of the ternary phase diagram provides the basis for the choice of an appropriate starting composition for the crystal growth. The phase relations in

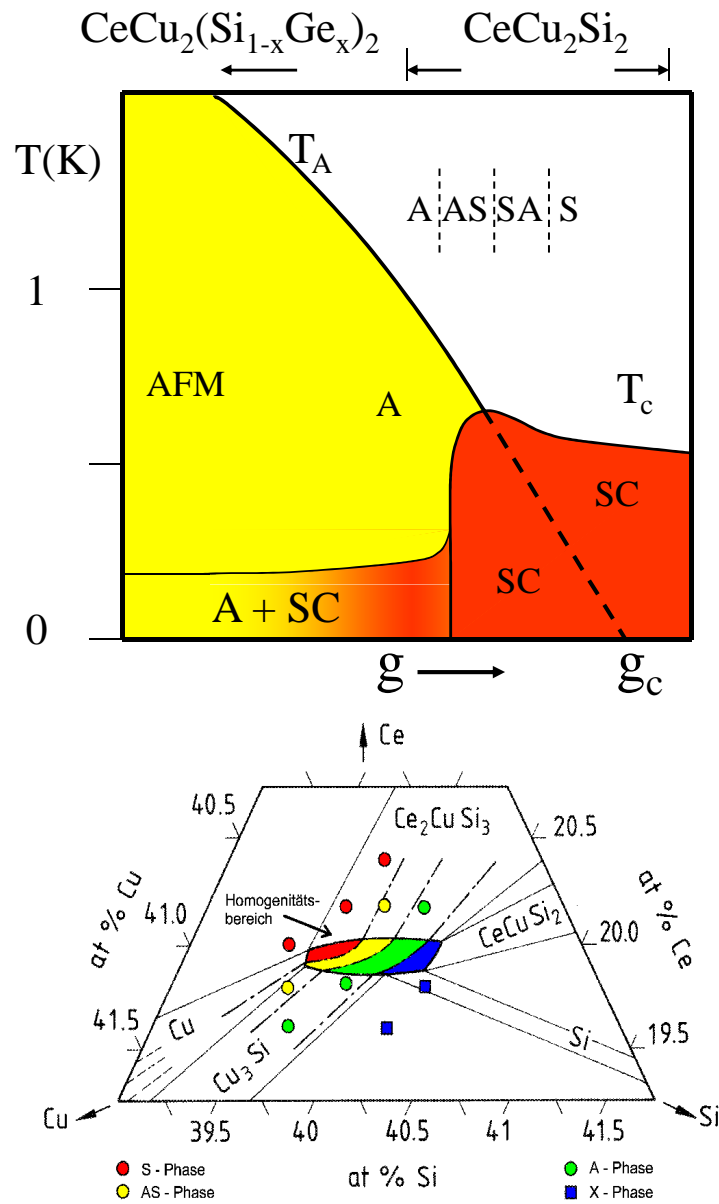


Figure 2.2: Upper part shows schematic magnetic and superconductivity phase diagram as a function of f-hybridization g , investigated by doping and isostatic pressure experiments. Lower part shows the effect of composition on the occurrence of different (magnetic or superconducting) ground states in pure $CeCu_2Si_2$.

the ternary Ce-Cu-Si system have been established in isothermal sections by several research groups [1, 2, 3]. The isothermal section of the Ce-Cu-Si system at 600°C, as shown in Fig. 2.7, is based on an early investigation and was complemented by data obtained in the group of C. Geibel. The phase CeCu_2Si_2 with the ThCr_2Si_2 structure type forms peritectically at 1545 °C (± 15 °C) [2]. Thus, a melt composition should be used that is located within the primary solidification area (i.e. the composition region where CeCu_2Si_2 is the first phase to solidify out of melt) not too far from the peritectic composition, which according to early reports is close to 30 % excess Cu [4, 2]. Otherwise, a crystal growth starting with a melt of CeCu_2Si_2 composition would lead to the formation of Ce_2CuSi_3 . The second problem is the extreme sensitivity of the low- T properties of CeCu_2Si_2 on tiny changes in composition. Thus, one observes within the small homogeneity region of CeCu_2Si_2 different types of ground states, a magnetic (A-type), a superconducting (S-type), a phase with competing magnetism - superconductivity (A/S-type) and a disordered magnetic state (X). This result is attributed to the fact that CeCu_2Si_2 is located very close to a quantum critical point where magnetic order is suppressed and replaced by superconductivity. This is demonstrated in the upper part of Fig. 2.2, which shows a schematic phase diagram of the ground states vs. the c-f hybridization strength here named g . This schematic phase diagram was drawn using the data from pressure experiments and chemical doping experiments. It shows three different phases. The AFM phase is a more local-moment antiferromagnetic (AFM) phase. It is possible to obtain this AFM phase by replacing Si by isoelectronic Ge, which acts as negative chemical pressure. The A phase is a spin-density-wave type of magnetic order [8] while the S phase corresponds to the superconducting phase. Further on, this phase diagram shows the

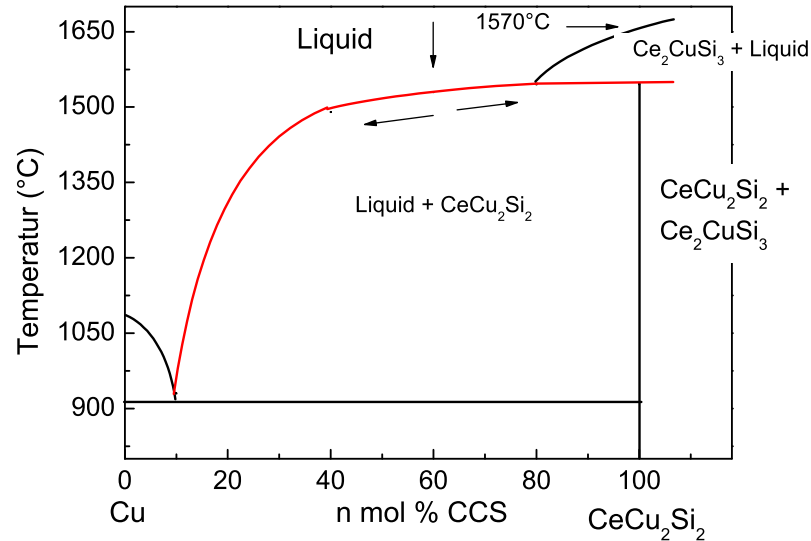


Figure 2.3: Peritectic formation of CeCu_2Si_2 single crystals from Cu rich melt, melt concentration is 60 mol % $\text{Ce}_y\text{Cu}_2\text{Si}_2$ + 40 mol % Cu [5].

possible coexistence of the magnetic and the superconducting phase on the left side, while on the right side superconductivity and magnetic order compete, the former one expelling the latter one below T_c . These different phases are obtained under isostatic pressure or by varying the Cu to Si ratio.

The aim of the present work was set to grow large single crystals for all these different ground states, in order to perform neutron experiments and to investigate the nature of the A phase, the interactions between the unconventional magnetic state and the superconducting phase, and also to look at the possible competition or coexistence of superconductivity and magnetism in pure CeCu_2Si_2 and Ge-doped single crystals.

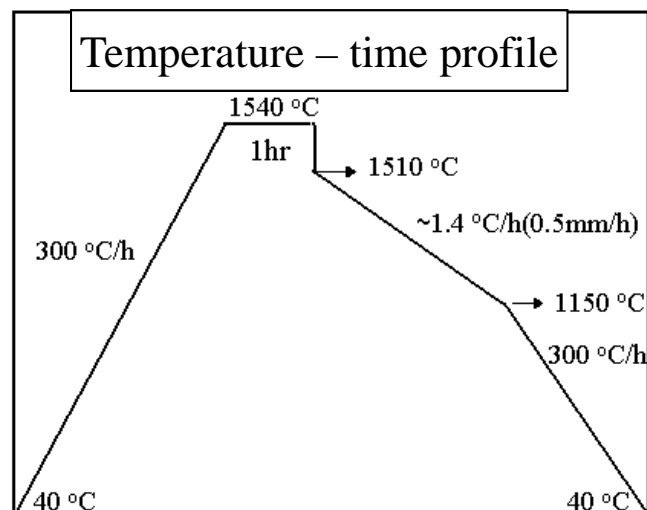
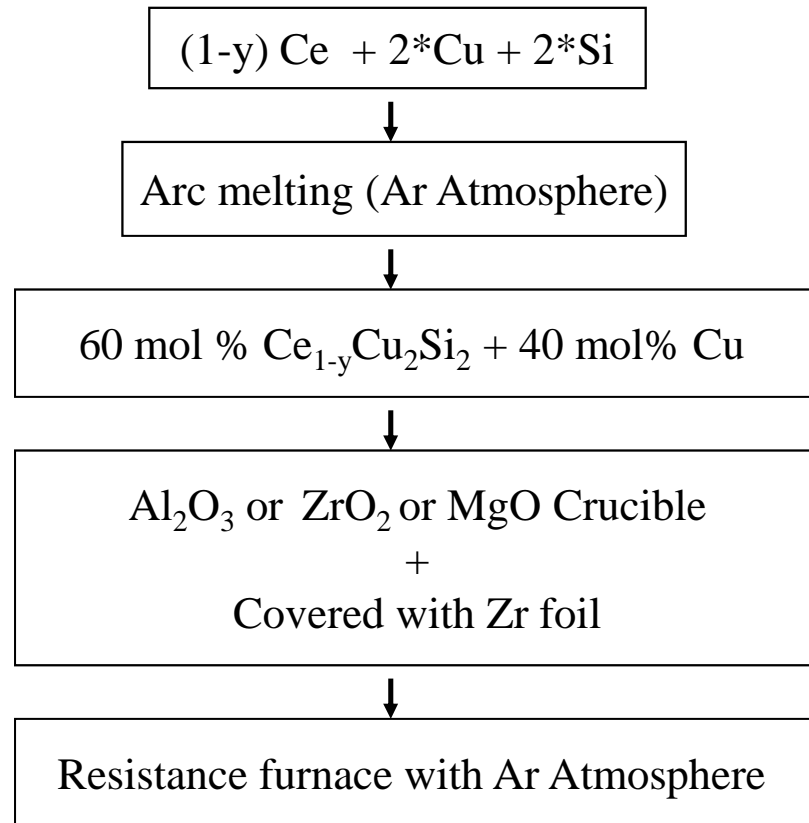


Figure 2.4: The flow chart of the steps involved in single crystal growth of CeCu_2Si_2 .

It was known that in polycrystalline samples the different ground states can be obtained by taking different Cu to Si ratio. For example, the Cu rich side, $\text{CeCu}_{2.05}\text{Si}_2$ leads to a superconducting ground state (S-type). By contrast, excess of Si leads to the so called disorder state (X-type), which is short range magnetic ordered. The lower part of Fig. 2.2 shows the location of the different ground states in different colors within the homogeneity region in partial phase diagram of Ce-Cu-Si. In S type e.g., some of the Si sites are replaced by Cu which leads to an increase of the hybridization between the conduction electrons and f electrons. Therefore, it is essential to control the Cu-to-Si ratio in the single crystal growth in order to control the physical properties. For this purpose we modified the crystal growth method. Instead of growing single crystals from the melt with the exact 1:2:2 composition (pure Bridgman method), we used a combination of the flux and the Bridgman method. Basically we used a self-flux method with Cu as flux. We cooled the melt by moving the crucible slowly from high temperatures towards low temperatures. Thus, one can call this technique a modified Bridgman method or self-flux Bridgman method. When using Cu as flux, it is not possible to control the Cu-to-Si ratio directly. Therefore, we used Ce as tuning element, which basically tunes the Cu-to-Si ratio indirectly. In order to get a CeCu_2Si_2 single crystal with Cu excess, we start with $\text{Ce}_{1.05}\text{Cu}_2\text{Si}_2$ and Cu flux, which effectively corresponds to a Si deficiency in the melt. Fig. 2.3 shows how CeCu_2Si_2 forms peritectically out of a Cu-rich melt. In M. Deppe's thesis [5], he developed the growth technique for Ge-doped single crystals. He studied the influence of the amount of Cu excess and found that 40 mol % of Cu flux is best to obtain large single crystals of good quality. In this work we used 40 mol % for all the synthesis of pure and Ge-doped CeCu_2Si_2 . We initially worked with different crucible materials in

order to study the effect on the ground state properties. It was known that in Al_2O_3 crucible Al slightly dissolves in the flux and might enter the main phase. In order to look for better possibilities we tried different crucibles, for example ZrO_2 crucible, which have to be stabilized by e.g. Yttrium oxide. The problem is that our chemical analysis showed some amount of Yttrium in single crystals. Then one expects Yttrium to substitute Ce ions, which should result in a change in physical properties like e.g. the destruction of the coherence. We also attempted to use MgO crucibles, however, this results in a strong reaction between the melt and the crucible. Thus, finally we used large and conical shaped Al_2O_3 crucible. The aluminum contamination is reduced by taking a large (about 50 gm) melt, which reduced the ratio between contact surface between melt and crucible compare to the volume of the melt. The conically shaped crucibles allowed for the formation of initial crystals which act as seeds for further crystal growth.

Table 2.1: Starting composition and expected ground state for the final series of growth.

Sample	Starting composition	Expected –Type
#57004Al2	$\text{Ce}_{0.90}\text{Cu}_2\text{Si}_2$ (polycrystalline) + Cu flux	A–type
#57010Al1	$\text{Ce}_{0.925}\text{Cu}_2\text{Si}_2$ (polycrystalline) + Cu flux	AS–type
#57004Al3	$\text{Ce}_{0.95}\text{Cu}_2\text{Si}_2$ (polycrystalline) + Cu flux	AS–type
#57009Al1	$\text{Ce}_{0.975}\text{Cu}_2\text{Si}_2$ (polycrystalline) + Cu flux	SA–type
#57006Al1	$\text{Ce}_{1.0}\text{Cu}_2\text{Si}_2$ (polycrystalline) + Cu flux	SA–typ
#57008Al1	$\text{Ce}_{1.05}\text{Cu}_2\text{Si}_2$ (polycrystalline) + Cu flux	S-type

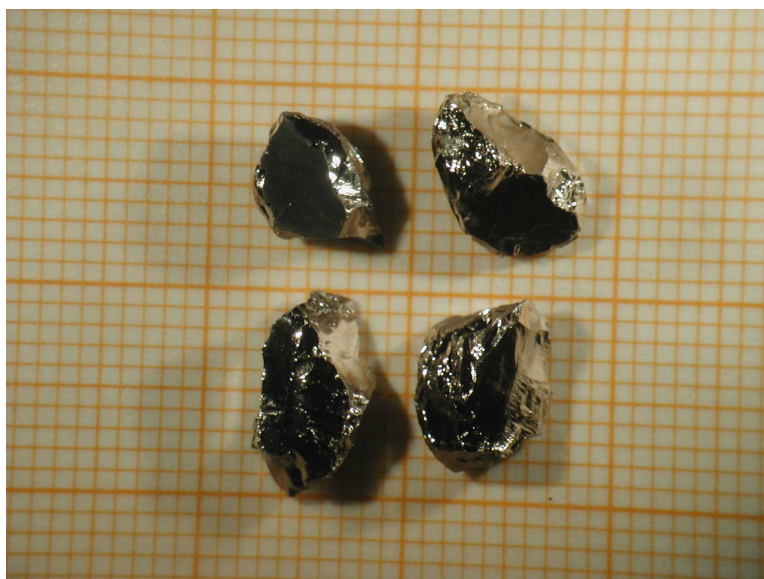


Figure 2.5: As-grown single crystals with a size of approximately 4 mm \times 5 mm \times 10 mm.

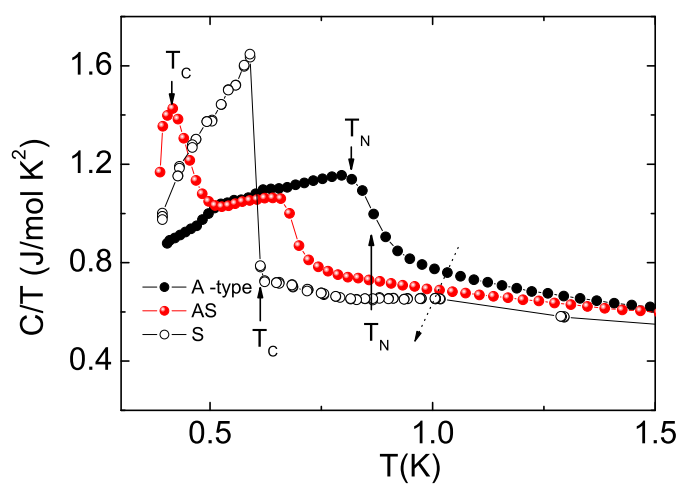


Figure 2.6: Low-temperature specific heat for for three different types of CeCu_2Si_2 single crystals.

Fig 2.4 shows the flow chart of the steps involved in single crystal growth. Polycrystalline $Ce_yCu_2Si_2$ samples with different y in order to get different ground states are prepared by arc melting in Ar atmosphere (table 2.1). The weight loss during the arc melting is less than 1 %. Ce (4N) from Ames lab as well as commercial Cu (5N) and Si (5N) served as starting material. The pre-alloyed samples are mixed with the appropriate amount of Cu (40 mol%) and put into an Al_2O_3 crucible, which is covered with Zirconium foil to act as an oxygen getter. The single-crystal growth time-temperature profile is shown in the lower part of Fig. 2.4. The time-temperature profile is based on results of Differential Scanning Calorimetry (DSC) investigations for samples with different amount of Cu flux. Based on these results, we were able to determine the exact liquidus temperature, i.e. where the whole batch is completely melted. The determination of the liquidus temperature is of importance to avoid overheating of the melt which would cause a stronger contamination with aluminum. The crucibles are heated to 1540 °C and kept for 1hr to ensure that the whole batch is melted, then the melt is cooled down to 1510 °C by pulling down the crucible while keeping the furnace temperature constant. This initial fast cooling process avoids to keep the melt for too long at high temperature, which would also results in a higher Al-content. The crystals were grown by pulling down the crucible at a rate of 0.25 mm/hr, which corresponds to approximately 0.75 °C/hr. The total crystal growth takes place in approximately 6 to 7 days. More details of the furnaces can be obtained in M. Deppe's thesis [5]. After the growth the crystals were extracted mechanically. With this method it is possible to synthesize large single crystals of mass ranging from a few hundred milligram to a few grams. Fig 2.5 shows the as-grown single crystals of size approximately 4 mm \times 5 mm \times 10 mm. After optimizing the

growth process we performed a series of growth attempts where only the y parameter was changed. Batch number, starting composition and the expected ground state are listed in table 2.1. These single crystals were the basis for detailed studies of the physical properties presented and discussed in chapter 3 and chapter 4. To provide an idea we display here the low-temperature specific heat for three single crystals with different ground states. Fig 2.6 shows the low-temperature specific heat divided by temperature versus temperature of an A-type, an AS-type and an S-type single crystals below 1.5 K. The three curves show different kind of anomalies. The shape of the anomaly at 0.85 K in the data of the A-type crystal indicates a transition to long-range AFM order [8]. The AS-type sample undergoes two subsequent phase transitions, the first one at $T_N = 0.7$ K with a small anomaly indicating the formation of long-range AFM order and a transition to a superconducting state at $T_c = 0.5$ K with a larger anomaly. In the case of the S-type crystal, the superconducting phase-transition anomaly is rather sharp and large with a step size of nearly 1 J/mol.K². Although these three different single crystals show different physical ground state, we did not find substantial differences in lattice constants nor in chemical analysis, see discussion in chapter 3.

The same growth procedure was adopted for Ge-doped $Ce_yCu_2Si_2$ single crystals. With increasing Ge content the melting temperature decreases. Therefore, we started the crystal growth at a slightly lower temperature (1500 °C) instead of 1510 °C. We also studied the effect of the Ce-to-Si ratio on the physical properties and the ground states by varying the initial Ce content y as in undoped sample. We grew single crystals of $Ce_yCu_2(Si_{1-x}Ge_x)_2$ and Cu flux for $y = 0.8, 0.9, 0.98, 1.05$ and $x = 0.02$ and 0.1. The structural and the physical properties of the Ge-doped single crystals

are reported and discussed in chapter 4.

2.3 Synthesis of YbRu_2Ge_2

The sensitivity of ytterbium to air and moisture required the sample handling to be carried out in an argon-filled glove box. The polycrystalline YbRu_2Ge_2 samples were prepared by a sintering method. A stoichiometric (with 2 % excess of Yb) amount of the three elements (99.99 % pure) were put in an Alumina crucible, which was then sealed inside a tantalum crucible using arc welding in Ar atmosphere. The element mixture inside the sealed Ta crucible was reacted at 1200 °C for four days in Ar atmosphere and then cooled to room temperature at 300 °C/h. The sample was subsequently powdered and pressed into pellets and heated (in a sealed Ta crucible) to the same temperature for 6 more days. X-ray powder diffraction and energy dispersive X-ray analysis (EDAX) was used to check the composition and the structure of the sample, confirming the formation of polycrystalline of YbRu_2Ge_2 with lattice parameter $a = 4.2105 (10) \text{ \AA}$ and $c = 9.7567 (20) \text{ \AA}$.

Single crystals of YbRu_2Ge_2 were prepared using the flux method (both Sn- and In-flux). In Indium flux we got comparatively larger and good quality single crystals. A stoichiometric amount of Yb (4N), Ru (5N), Ge (5N) and 98 mol% In were put in an Al_2O_3 crucible which was then covered with Zirconium foil and heated to 1550 °C. It was kept there for 12 hr, then cooled slowly to 1400 °C at 3 °C/hr cooling rate before cooling to room temperature at 250 °C per hour. The single crystals were mechanically extracted from the melt at 300 °C temperature, basically picking the single crystals from the flux melted on a hot plate. Finally, the remaining flux was chemically etched from the surfaces. The upper part of Fig. 2.8 shows the extracted

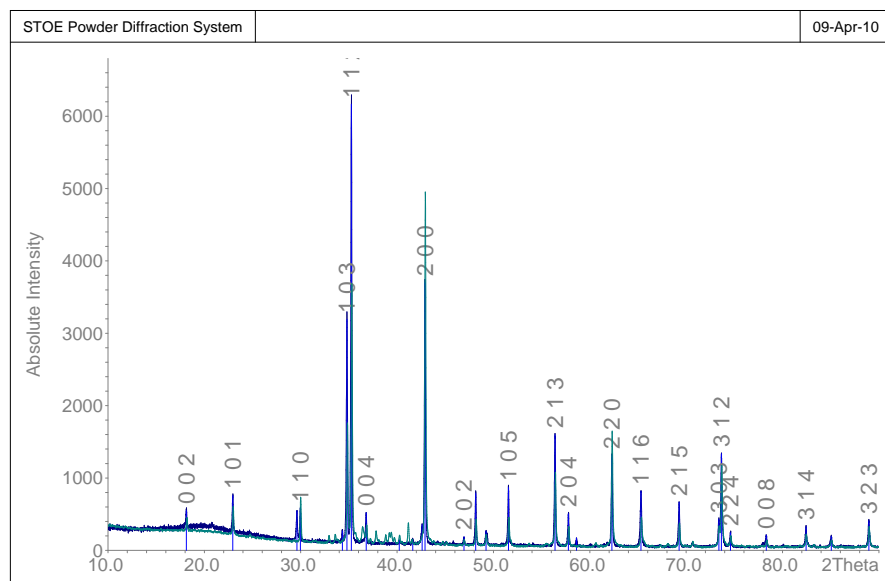


Figure 2.7: X-ray power diffraction pattern of YbRu_2Ge_2 , both polycrystals (blue) and single crystals (green). The vertical bars mark the expected Bragg peaks positions, un-indexed peaks correspond to impurity phases.

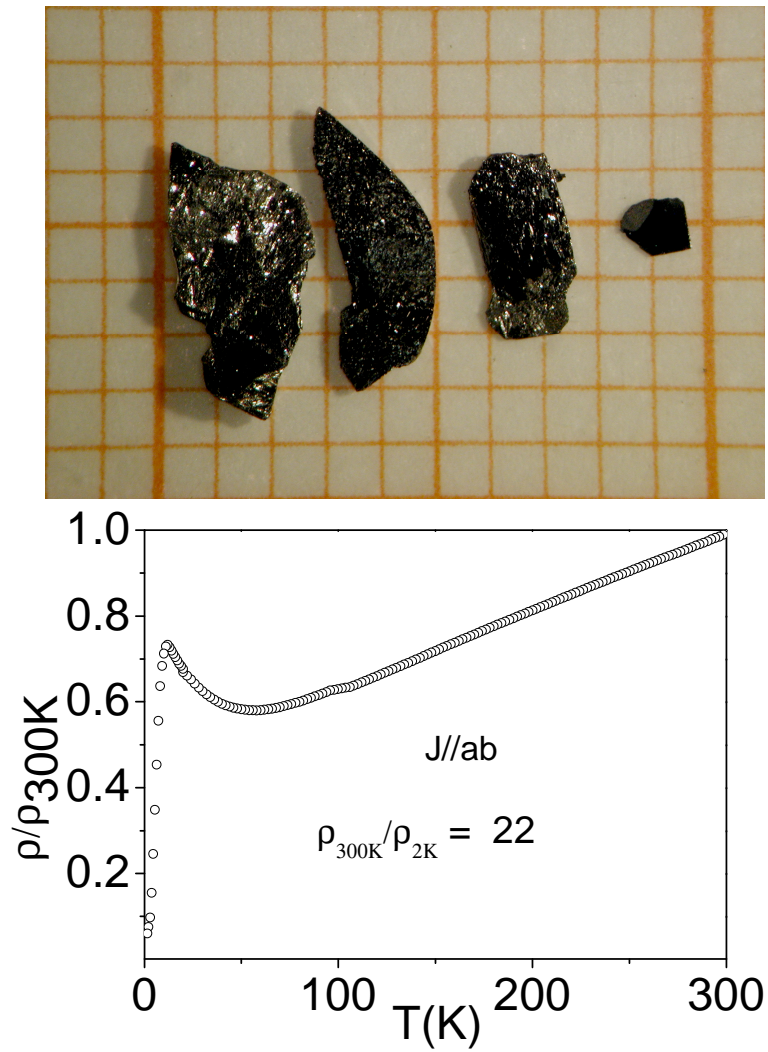


Figure 2.8: Upper part shows single crystals of YbRu₂Ge₂ after etching in acid. The lower part shows the resistivity measured in the temperature range 2K to 300K.

single crystal. Some single crystals were crushed into powder and performed X-ray powder diffraction (Fig. 2.7). The results confirm the formation of YbRu_2Ge_2 with lattice parameter $a = 4.2116(10) \text{ \AA}$ and $c = 9.7545(20) \text{ \AA}$. These lattice parameters correspond to those obtained in the analysis of our polycrystals, $a = 4.2105(10) \text{ \AA}$ and $c = 9.7567(20) \text{ \AA}$, but differed significantly from those reported in the literature, $a = 4.203(4) \text{ \AA}$ and $c = 9.763(9) \text{ \AA}$ [7]. With this method it is possible to get comparatively large single crystals of 5 mg to 50 mg with good quality, see upper part of Fig. 2.8. The lower part of Fig. 2.8 shows the resistivity measured from room temperature down to 2 K. The residual resistivity ratio is about 22, which is comparatively high for Yb transition-metal compounds indicative of good quality. The detailed investigation of YbRu_2Ge_2 using resistivity, susceptibility and specific heat measurements as well as local probes like neutron and μSR experiments is presented in chapter 5.

2.4 Experimental methods

The crystal structure and phase purity was investigated by standard X-ray powder diffraction. The orientation of the single crystals was determined with a Laue camera. Physical properties like resistivity and specific heat were measured down to 400 mK and up to 14 T magnetic field in standard Quantum Design Physical Property Measurement Systems (PPMS) with ^3He option. Resistivity and specific heat were determined using a standard four-lead method and a thermal relaxation method, respectively. DC susceptibility and isothermal magnetization measurements up to 5T were performed in a commercial Superconducting Quantum Interference

Device (SQUID) magnetometer (Quantum Design). The angle dependent magnetization measurements on single crystals were carried out using the rotator option of the SQUID magnetometer.

The zero field (ZF) μ SR (Muon Spin Rotation, Relaxation and Resonance) measurements were performed at the pulsed neutron and muon facility at ISIS (Rutherford Appleton Laboratory, UK). In this spectrometer the sample was mounted into an Oxford Instruments Variox cryostat (1.2 K-300 K). 100 % spin polarized muons with an energy of approximately 3.2 MeV were implanted into the sample. These muons come to rest rapidly (in 10^{-10} s). After thermalizing in the sample the spin of the muons precess in the magnetic field at the muon site and subsequently decay into positrons [9, 10]. These positrons are emitted preferentially along the spin direction of the muon at the time of decay. The sample was mounted onto a silver plate. Any muon implanted into the silver will give a time and temperature independent signal in the asymmetry. The asymmetry is determined by the equation

$$G_z(t) = \frac{N_F - \alpha N_B}{N_F + \alpha N_B} \quad (2.4.1)$$

where N_F is the counts in the forward detectors, N_B is the counts in the backward detectors, and α is a calibration constant

The elastic neutron diffraction measurements on polycrystalline samples of YbRu_2Ge_2 was carried out using D20, a two-axis diffractometer at the reactor at Institute Laue-Langevin (ILL) in Grenoble, and neutrons with a wavelength of 2.41 Å. The inelastic neutron experiments on YbRu_2Ge_2 to determine the crystal field scheme were performed in the HET spectrometer at the pulsed neutron and muon facility at ISIS (Rutherford Appleton Laboratory, UK). The neutron scattering experiments on pure and Ge-doped CeCu_2Si_2 were performed in various experimental facilities at ILL in

Grenoble, with the two-axis diffractometer E6 at the HMI Berlin, and the three-axis spectrometer PANDA at the Forschungsneutronenquelle Heinz Maier-Leibnitz FRM - II, Garching [8].

Bibliography

- [1] O. I. Bodak, Ya. M. Kalychak, E. I. Gladyshevskii, *Inorg. Mater.* (Engl. Trans.), **10(3)**, 388 (1974).
- [2] H. F. Braun, J. L. Jorda, *Physica B* **135**, 72 (1985).
- [3] R. Modler, M. Lang, C. Geibel, C. Schank, R. Müller-Reisener, P. Hellmann, A. Link, G. Sparn, W. Assmus and F. Steglich, *Physica B* **206-207**, 586 (1995).
- [4] S. Nuettgens, G. Keyser, F. Ritter and W. Assmus, *J. Phys.: Condensed Matter* **12**, 4807 (2000).
- [5] M. Deppe, PhD Thesis, Technische Universität Dresden.
- [6] O. Bodak, P. Rogl, vol-11C2: Non-Ferrous Metal Systems. Part 2, Landolt-Boernstein New Series IV/11C2, (2007).
- [7] M. Francois, G. Venturini, J. F. Mareche, M. Malaman, and M. Roques, *J. Less-comm. Metal* **113**, 231 (2005).
- [8] O. Stockert, E. Faulhaber, G. Zwicknagl, N. Stuesser, H. S. Jeevan, M. Deppe, R. Borth, R. Kuechler, M. Loewenhaupt, C. Geibel and F. Steglich. *Phys. Rev. Lett.* **92**, 136401 (2004).

- [9] A. Schenck, in *Muon Spin Rotation* (Hilger, Bristol, 1985).
- [10] Muon Science: Muons in Physics, Chemistry and Materials (ed S.L. Lee, S.H. Kilcoyne and R. Cywinski) (Pub: Scottish University Summer School and IOP) 1998.

Chapter 3

Magnetism and superconductivity in CeCu_2Si_2

3.1 Introduction

In 1979, the discovery of superconductivity in CeCu_2Si_2 being the first heavy-fermion superconductor [1] has opened up a new field of research in condensed matter physics. Yet, the nature and the mechanism of the superconducting phase is still under debate. CeCu_2Si_2 crystallizes in the tetragonal ThCr_2Si_2 structure type (see Fig. 3.1). The Ce ion is in a nearly trivalent state with a total angular momentum $J = 5/2$. The resistivity increases below room temperature with lowering the temperature indicative of the Kondo effect. Below 20 K, it drops due to the onset of coherent scattering of the conduction electron by the Kondo ions.

Besides the superconducting state in CeCu_2Si_2 exhibits further ground states even at ambient pressure. Nearly 10 years after the discovery of superconductivity (SC), NMR and μSR measurements observed a second phase called A phase, which was suggested to be of magnetic origin [2, 3]. It is believed that the compound is close to an antiferromagnetic quantum critical point (QCP) at slightly negative pressure

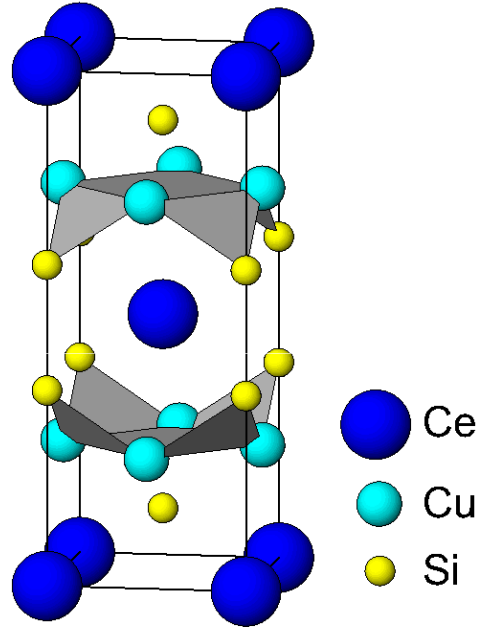


Figure 3.1: Crystal structure of CeCu₂Si₂, ThCr₂Si₂ structure type.

at which the A phase disappears [4, 5, 6, 7, 8, 9, 10, 11]. The QCP is accessible, for example, by partial substitution of Si by Cu in non-stoichiometric sample or by a small pressure. When applying pressure, T_c initially remains close to its ambient pressure value, followed by a sudden increase at 3 GPa up to 1.5 K. Further increase of the pressure results in a slow suppression of T_c . Many of the superconducting properties of CeCu₂Si₂ cannot be understood in terms of the BCS theory, which was established to describe the physics of conventional superconductors. One of the exceptional features in CeCu₂Si₂ is the fact that heavy quasiparticles condense into heavy Cooper pairs.

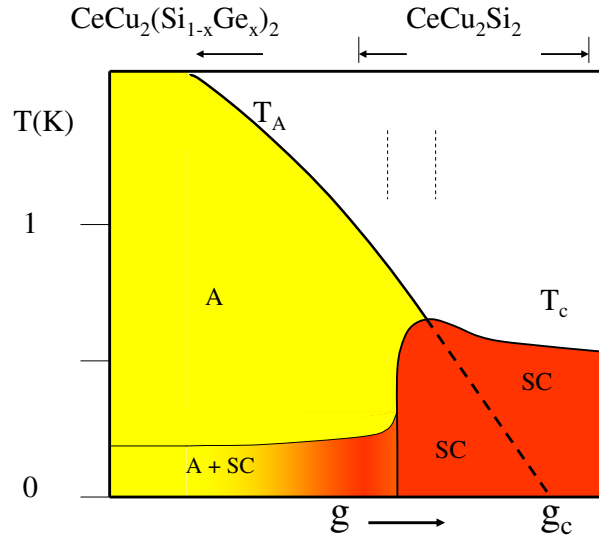


Figure 3.2: Complex phase diagram of CeCu_2Si_2 as a function of the hybridization strength g using the results of pressure and chemical doping experiments.

Ce-based heavy-fermion superconductors, however, are still scarce. The application of pressure in the 10 to 100 kbar range to members of this structure family such as CeCu_2Ge_2 [4, 5, 7], CePd_2Si_2 [12] and CeRh_2Si_2 [13] is necessary to induce superconductivity. Recently a new family of cerium compounds, CeMIn_5 , was added where at ambient pressure heavy fermion superconductivity occurs for $M = \text{Co}$ and Ir at $T_c = 2.3$ and 0.4 K, respectively [14, 15]. In CeRhIn_5 , pressure initiates superconductivity, below $T_c^{\text{max}} = 2.1$ K [16]. The crystal structure of these latter compounds can be considered as quasi-two-dimensional variants of CeIn_3 [17, 12]. CePt_3Si is a very recent heavy fermion SC with $T_c = 0.75$ K that orders magnetically at $T_N = 2.25$ K. Specific heat [18], NMR [19, 20] and μSR [21] studies indicate that superconductivity and long range magnetic order coexist on a microscopic scale.

As mentioned earlier CeCu_2Si_2 presents a complex phase diagram with different ground states (cf. Fig. 3.2). The label g plotted at the abscissa marks the tuning parameter, which represents the hybridization strength between local f-electron and conduction electrons. This hybridization strength can be varied by fine tuning the Cu to Si ratio, by applying isostatic pressure, and also by replacing Si by Ge, which acts as negative chemical pressure. It shows three different phases, including AF-type (localized antiferromagnetic Ce moments), A-type (Spin Density Wave) and SC phases (superconducting phase)[22, 23, 24, 25]. In this work we aim at growing large single crystal with precise ground-state properties in order to study the physical properties and to perform neutron experiments.

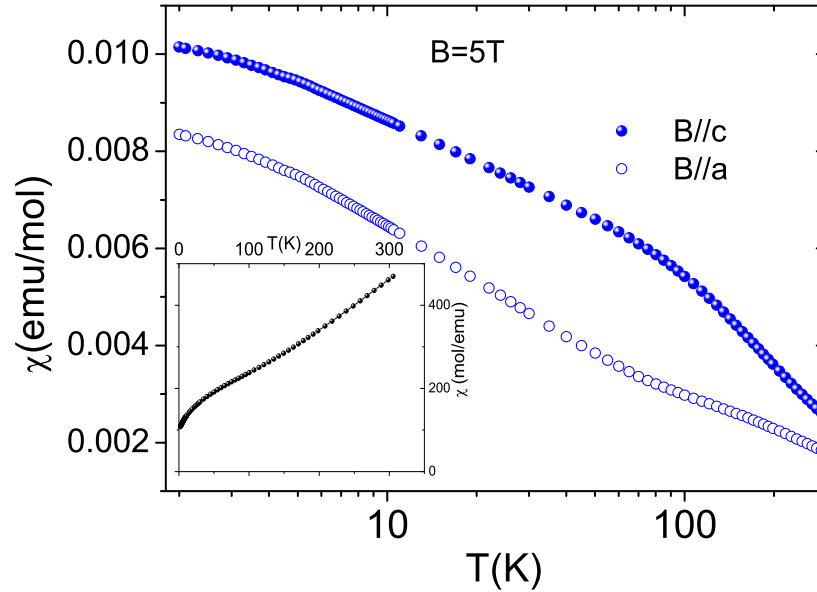


Figure 3.3: Temperature dependence of magnetic susceptibility χ in an applied field of 5 T, measured along the two crystallographic axis a and c. Inset: Inverse of the average susceptibility χ_{avg} as a function of T .

3.2 Different physical ground states in CeCu_2Si_2

3.2.1 A-type CeCu_2Si_2

As explained in the crystal growth chapter and introduction of this chapter, the low temperature properties of CeCu_2Si_2 are very sensitive to the stoichiometry, for e.g., Ce:Cu:Si ratio [24, 26]. It is possible to get different type of single crystals by tuning the initial composition. By starting with a deficit of Ce, which leads to a deficit of Cu in the resulting single crystal, we succeeded to grow large (0.1 to 1.4 g) A-type CeCu_2Si_2 single crystals and investigated their properties.

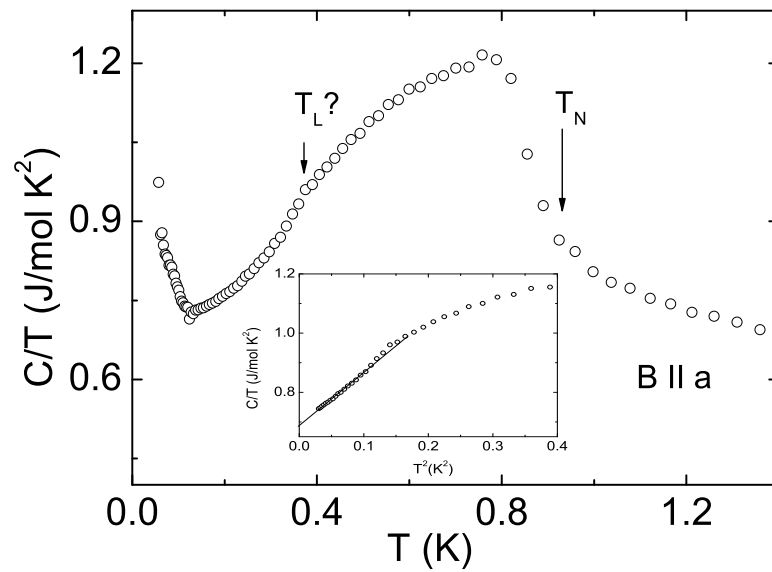


Figure 3.4: Temperature dependence of the specific heat C/T of $CeCu_2Si_2$ A-type single crystal, in zero applied magnetic field. The plot shows a pronounced anomaly at 0.85 K and a second one around 0.4 K. The anomaly at 0.85 K is due to magnetic transition while the weak anomaly at 0.4 K is possibly due to a "Lock in" transition. The strong increase in the specific heat below 100 mK is attributed to the nuclear contribution. The inset shows C/T vs. T^2 in the range $0.15 \text{ K} < T < 0.65 \text{ K}$ for which the low- T part dominated by the upturn of the nuclear contribution is omitted.

The temperature dependence of the magnetic susceptibility of an A-type single crystal measured in the temperature range 2 K to 300 K at fixed magnetic field is shown in Fig. 3.3, where the temperature axis is displayed in a log scale. The susceptibility was measured along both crystallographic axis. No difference was observed between zero field-cooled and field-cooled measurements. Upon cooling from room temperature, the magnetic susceptibility increases showing a magnetic anisotropy between a and c axis. A broad anomaly is observed at approximately 100 K being more prominent along c- axis, which is attributed to the crystal electric field (CEF) effect. Both, the anisotropy and the broad anomaly can be accounted for by the CEF. The inset of Fig 3.3 shows that the inverse average magnetic susceptibility, $1/\chi_{avg}T$ roughly follow a Curies-Weiss law in the temperature range 300 K to 200 K. The average susceptibility $\chi_{avg} = [2\chi_a + \chi_c]/3$ allows us to calculate the effective magnetic moment μ_{eff} and the Weiss constant. The estimated values of μ_{eff} and Weiss constant are $2.54\mu_B$ and -73 K, respectively. μ_{eff} corresponds to the expected Ce^{+3} moment while the large Weiss constant reflects the strong hybridization of f-electron and conduction electron. At low temperatures below 4 K, the susceptibility reaches an enhanced constant value expected for a paramagnetic Kondo-lattice system.

The specific heat is one of the important quantity which allows to determine the bulk nature of any phase transition. Fig. 3.4 shows the specific heat of an A-type $CeCu_2Si_2$ single crystal measured in zero-field in the temperature range from 2.5 K to 0.05 K. The specific heat was measured using a quasi-adiabatic heat pulse method [27]. The total specific heat of $CeCu_2Si_2$ contains a phonon part (which is important only at higher temperature and thus can be completely neglected in the following analysis), a nuclear part, an electronic and a magnetic part. The nuclear

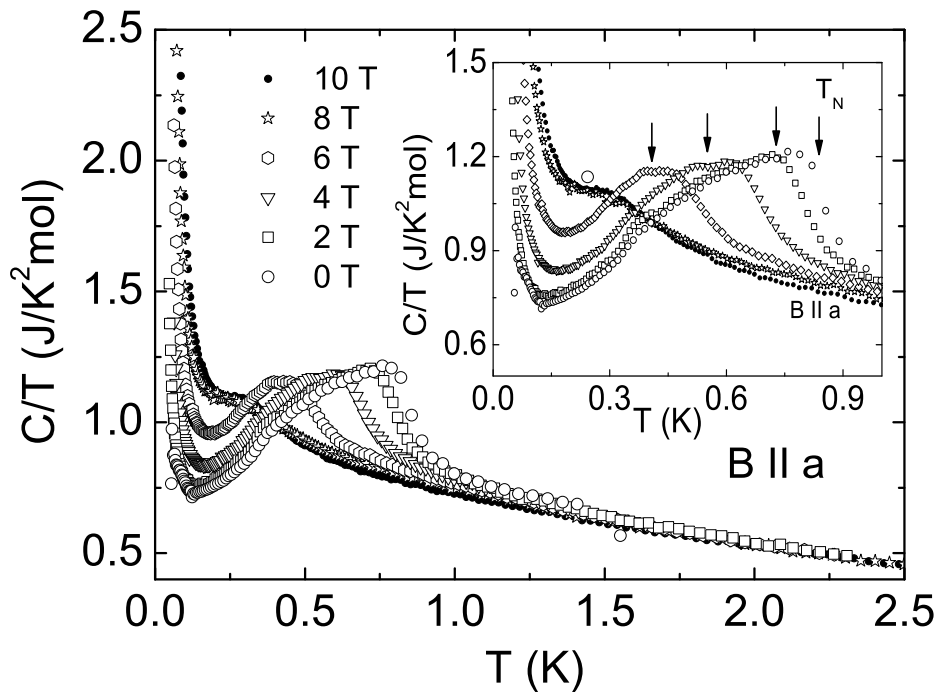


Figure 3.5: Temperature and magnetic field dependence of the specific heat of CeCu_2Si_2 A-type single crystal. The phase transition into the magnetic A-phase becomes broader and shifts to lower T for fields applied along the a-direction. The inset shows the magnified part of the low-temperature specific heat.

contribution of the specific heat from the hyperfine field is only important at very low temperatures (below 100 mK). It is clear from the C/T results that the electronic specific heat increases rapidly upon decreasing temperature and reaches a value of 0.75 J/mol K² just before the transition. A broad anomaly with a jump height of 0.3 J/mol K is observed at 0.85 K. The field dependence (see below) proves that this anomaly is connected with the antiferromagnetic (AFM) A-phase. The nature of this AFM phase will be described in more details below. The increase of the specific heat below 100 mK is attributed to the nuclear Zeeman effect on the Cu and Si nuclei due to an internal field in the antiferromagnetic state. The inset of Fig. 3.4 shows the C/T versus T^2 plot in the temperature range 0.15 K < T < 0.65 K (for T < 0.15 K the specific heat is deleted due to the upturn of the nuclear contribution). The coefficient of electronic specific heat γ estimated by extrapolating C/T versus T^2 is 690 mJ/mol.K². The small anomaly in the specific heat at 0.4 K is possibly due to a lock-in transition of the antiferromagnetic phase. More details about the lock-in transition will be discussed later.

Figure 3.5 shows the temperature dependence of the specific heat of the A-type CeCu₂Si₂ under magnetic fields between 0 T to 10 T, applied parallel to the a-axis. Upon applying 2 T, the anomaly at 0.85 K shifts only very slightly to 0.8 K, and therefore rules out the possibility of a superconducting phase transition because in 2 T field superconductivity should be completely suppressed [28]. With increasing field up to 8 T the peak gets broaden and its position shifts to lower temperature. Above 8 T, there is no shift anymore, which is likely due to a transition from the A-Phase to the so called B phase. The nature of this high field B-phase is yet unknown, but it is likely to also be a magnetic state.

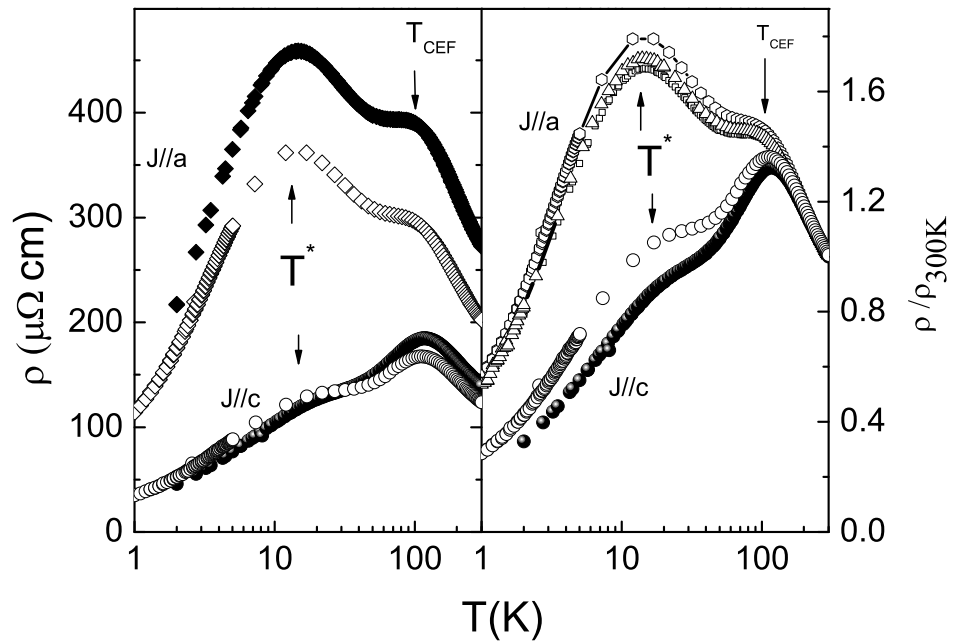


Figure 3.6: The electrical resistivity below 300 K shows a clear anisotropic behavior. $\rho(T)$ measured with the current J parallel to the crystallographic c -direction is lower than for the in-plane measurement ($j // a$). The two maxima in $\rho(T)$ are denoted as T^* and T_{CEF} . (a) Plot of the absolute resistivity versus temperature and (b) normalized to its value at 300 K (different symbols represent different crystals from same batch).

The electrical resistivity between 1 K and 300 K is shown in Fig. 3.6 for two different A-type single crystals where the temperature is plotted on a logarithmic scale. The resistivity was measured with the current along a- and c- axes on two different A-type single crystals. Due to the uncertainty in the absolute values of the resistivity for different single crystals, we also plot the electrical resistivity normalized to its room temperature. The uncertainty in absolute values is possibly due to probe contacts, micro cracks and grain boundary contributions etc. The resistivity for $J//a$ is larger than for $J//c$, in accordance with earlier reports [29]. The resistivity shows two broad maxima, a first one at 100 K (T_{CEF}) and a second one at 10 - 15 K. The resistivity maximum at 100 K is associated with the Kondo scattering of excited CEF levels. The broad peak with maximum at $T^* = 20$ K is connected with the scattering by the ground-state CEF level. The drop in ρ at lower T is due to the formation of the coherent Kondo lattice. The Kondo temperature T_K can be estimated by $T_K \simeq T^*/2$. The low-temperature resistivity maxima at T^* , for current J parallel to the a-axis is sharp compared to the one for J parallel to c-axis. The difference can be attributed to the wave function of the ground-state and excited CEF levels [30]. The resistivity ratio at 2K $\rho(300K)/\rho(2K) \simeq 1.26$ for $J//a$ and $\simeq 2.03$ for $J//c$, shall be discussed later.

In Fig. 3.7 the low-temperature electrical resistivity measured for current J parallel to a- and c-axis is plotted in the temperature range 4 K to 0.4 K. The solid line shows fit to a power-law $\rho = \rho_0 + AT^n$. The resistivity measured with current J parallel to a can be well fitted with $\rho_0 = 5 \mu\Omega\text{cm}$, $A = 35 \mu\Omega/\text{K}^n$ and $n = 0.85$ in the temperature range 1 K to 4 K. It should be noted here that below 0.85 K, A-type single crystals exhibit magnetic ordering. The resistivity $J//a$ shows a kink

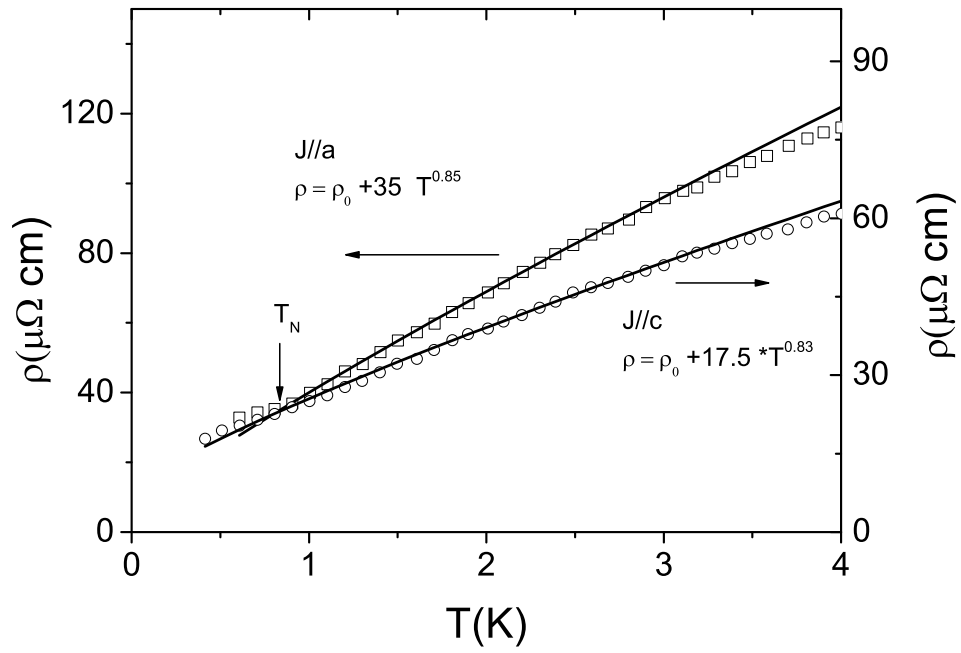


Figure 3.7: Low-temperature electrical resistivity of the A-type single crystal measured below 4K, measured both along $J//a$ and $J//c$ as a function of temperature. Solid lines show the fit to $\rho = \rho_0 + AT^n$ with $\rho_0 = 5 \mu\Omega \text{ cm}$, $A = 35 \mu\Omega/\text{K}^n$ and $n = 0.85$ along the a axis and $\rho_0 = 8 \mu\Omega \text{ cm}$, $A = 17.5 \mu\Omega/\text{K}^n$ and $n = 0.83$ along the c axis.

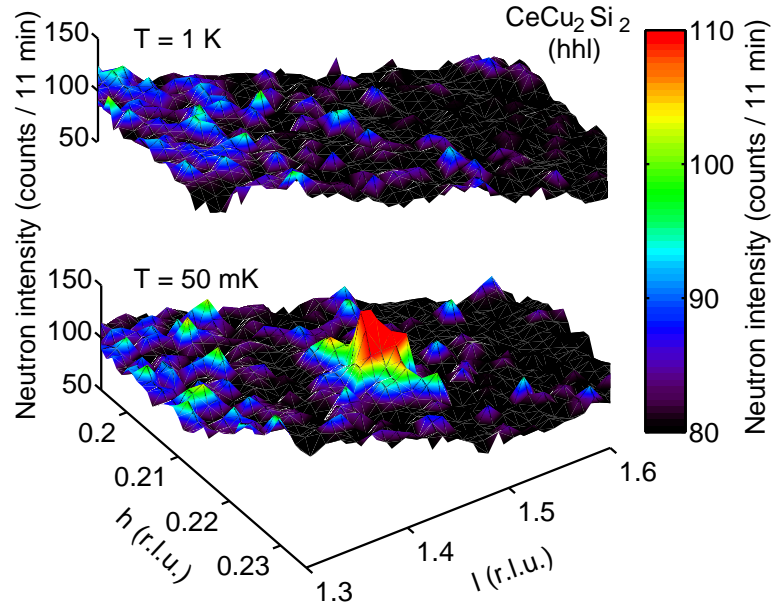


Figure 3.8: Neutron diffraction intensity map for the reciprocal $(h h l)$ plane both above and below Néel temperature. A clear magnetic satellite peak is visible at the position $(0.215 \ 0.215 \ 1.47)$ at 50 mK.

at the Néel temperature $T_N = 0.85$ K which is marked by an arrow (see also Fig. 3.5). This small increase marks the formation of a spin-density wave (SDW). Similarly the resistivity $J//c$ can be best fit with a residual resistivity value of $\simeq 8\mu\Omega\text{cm}$, which was again calculated using extrapolating the resistivity plot from 3 K to 1 K. In the temperature range 1 K to 4 K resistivity obeys a power-law dependence, $\delta\rho(T) \simeq AT^n$ with $n = 0.83$. The deviation from quadratic temperature dependence of the electrical resistivity above antiferromagnetic state is a classical feature of non-Fermi liquid behavior. The coefficient A (which is the measure of quasiparticle - quasiparticle scattering cross-section in the Landau Fermi liquid state where $n = 2$) has a larger value for $J//a$ than $J//c$.

Nearly a decade after the discovery of superconductivity in CeCu_2Si_2 , Cu NMR

[2] and μ SR [3] measurements revealed the A phase and lead to the prediction that this A phase is a SDW-like ordering. Recent electrical resistivity measurement [31] showed a small increase in resistivity for $J//a$ but a drop in the resistivity for $J//c$. The increase for $J//a$ suggested the formation of a gap in the A phase, supporting a SDW origin for the A-phase.

In order to prove the real nature of the A-phase we performed neutron diffraction experiments. The details about these experiments are given elsewhere [32]. Due to the lack of large single crystals with precise ground-state properties, neutron experiments failed to observe magnetic Bragg reflection thus far. Only recently, we successfully found the magnetic Bragg peak in A-type single crystals since large crystals with different ground states became available. The single crystal with dimensions $3 \times 4 \times 4 \text{ mm}^3$ and mass of about 450 mg, oriented using Laue-backscattering were used for the neutron diffraction experiment. Based on the knowledge from previous neutron diffraction experiments on Ge-doped samples [33], the neutron diffraction intensity maps of the reciprocal (hhl) plane around $q = (0.21, 0.21, 1.45)$ (it is basically a satellite peak of the (002) nuclear peak) were measured at 50 mK and 1 K, well below and above the transition. Fig. 3.8 shows the intensity maps at these two temperatures. The 1 K map which is above the magnetic transition show nothing but the q -independent background due to incoherent scattering of the sample. By contrast, a well resolved magnetic peak is visible at the position $(0.21, 0.21, 1.46)$ for $T = 50 \text{ mK}$. To look in more details at the width of the magnetic Bragg peak we also performed rocking scans, i.e integration of the data over the scattering angle 2θ and then plotted as a function of sample rotation ω as shown in Fig. 3.9. These results evidenced that the magnetic Bragg peaks are resolution limited, i.e that the

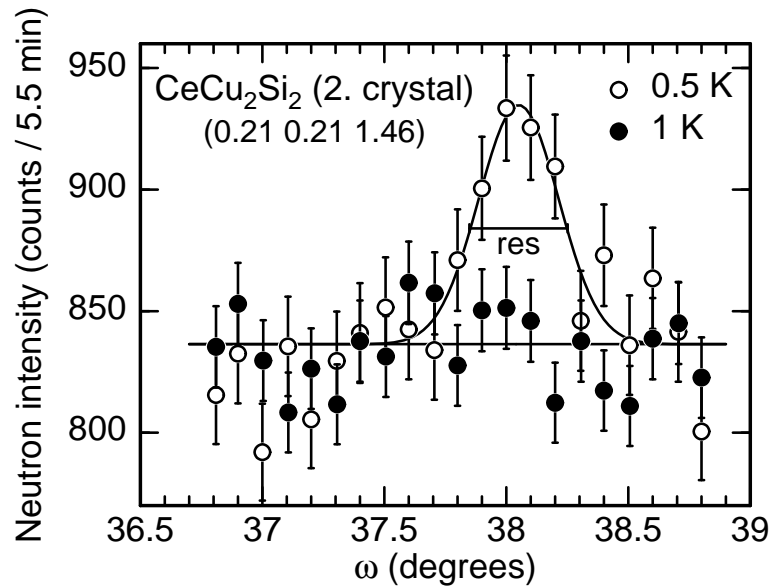


Figure 3.9: Rocking scan across the position of the magnetic satellite peak (0.21, 0.21, 1.46), both below and above the magnetic transition.

ordered state corresponds to a long range ordered state. At 50 mK, the position of the magnetic Bragg peaks with respect to nuclear peaks is found to be at $\delta Q = \pm(0.215, 0.215, 0.530)$. In order to confirm these results we measured different single crystals in different diffractometer. We always observed magnetic peaks at the same position $q = (0.21, 0.21, 1.46)$ and related ones at 500 mK, while no peaks were observed at 1 K. More detailed investigations of the magnetic A-phase was done using large single crystals at IN12 (ILL, Grenoble). In order to study the temperature dependence of the magnetic phase, we measured the temperature dependence of the intensity of magnetic Bragg peaks and of its position. The temperature dependence of this intensity and of the components h and l of the propagation vector are shown in Fig. 10.

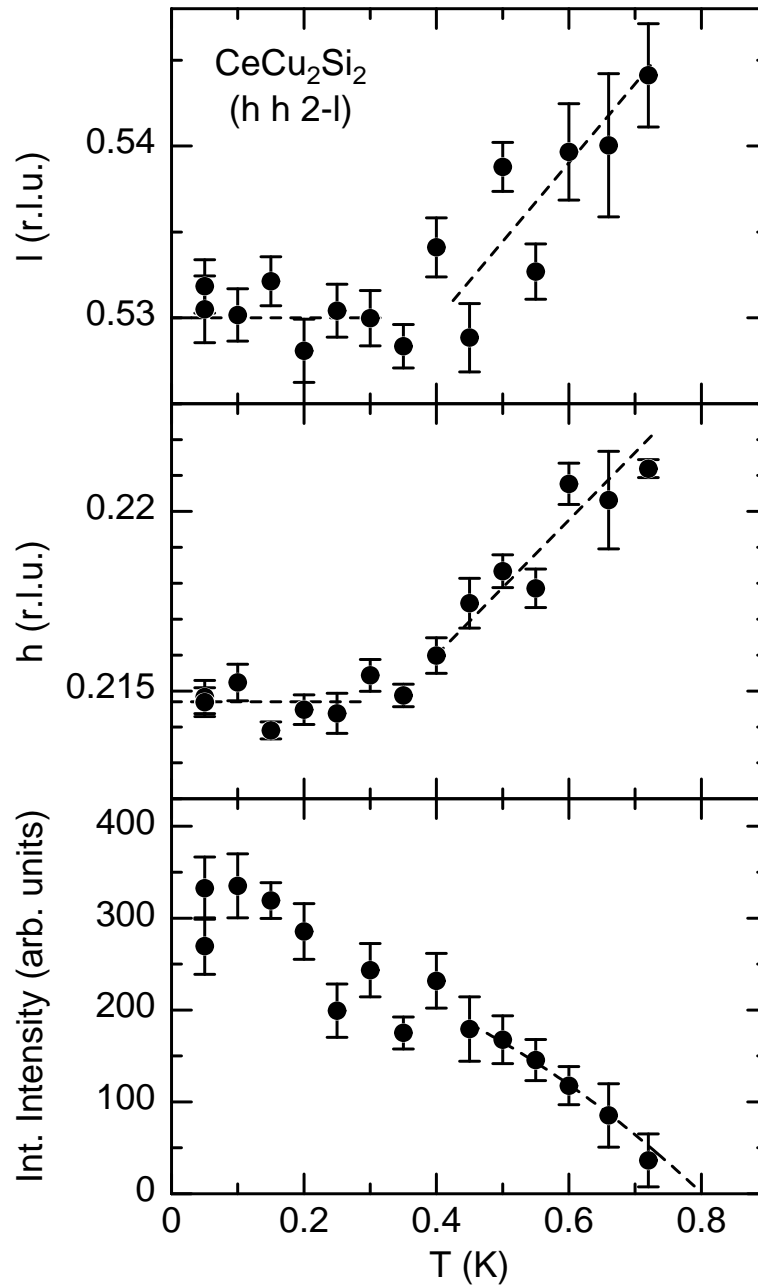


Figure 3.10: Upper part shows the temperature dependence of the components of the propagation vector and lower part the temperature dependence of integrated intensity of the magnetic peak. Dashed lines are guides to the eye.

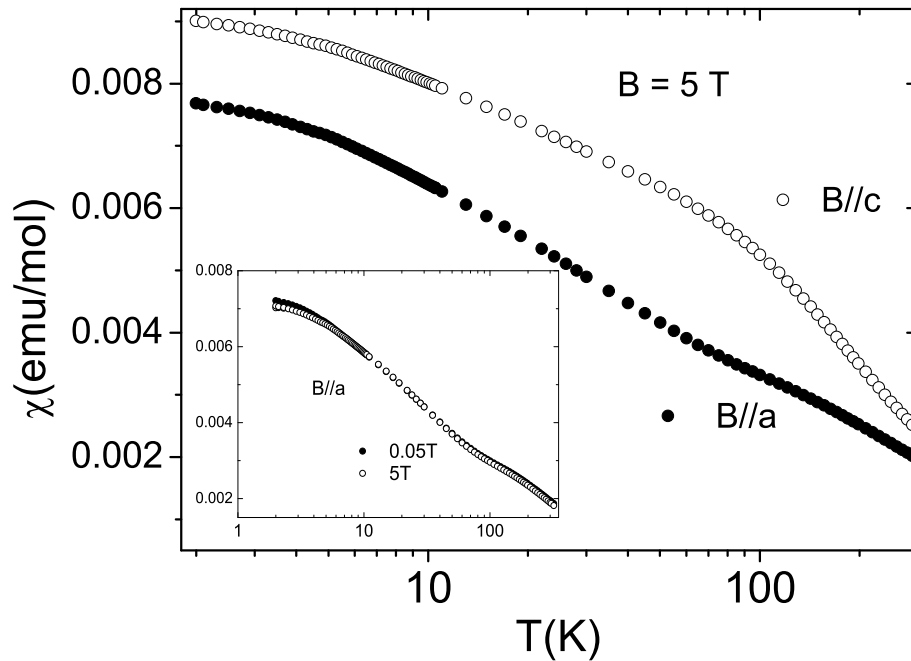


Figure 3.11: Temperature dependence of the magnetic susceptibility of an AS-type CeCu_2Si_2 single crystal in an applied field of 5 T, measured along the two crystallographic axis. Inset shows the field dependence of the magnetic susceptibility measured with $B//a = 0.05$ T and 5 T.

3.2.2 AS-type CeCu_2Si_2

In order to investigate the interconnection between the magnetic and the superconducting phase, we grew single crystals of AS-type, for which the magnetic phase transition occurs at a higher temperature than the superconducting one ($T_N > T_c$). Starting with the $\text{Ce}_{0.95}\text{Cu}_2\text{Si}_2$ composition in Cu flux, we successfully prepared large AS-type single crystals. In this section we describe the physical properties of these AS-type single crystals and their macroscopic and microscopic nature.

The temperature dependence of the magnetic susceptibility of an AS-type single crystal measured in the temperature range 2 K to 300 K is shown in Fig. 3.11, where the temperature axis is plotted in log scale. The susceptibility was measured along both crystallographic axis in an applied magnetic field of 5 T. The susceptibility of the AS single crystals is almost identical to those of the A-type described previously. The only difference is a slight reduction (by 10%) of the absolute value at 2K, in agreement with a slightly weaker magnetic character. The inset shows the magnetic field dependence of the susceptibility measured for two fields, 0.05 T and 5 T along the *a* axis. The high-temperature susceptibility is independent of field while at low temperature below 4 K it weakly decreases with increasing magnetic field. At high magnetic fields the susceptibility saturates suggesting that the system goes from non-Fermi liquid behavior to Fermi liquid behavior.

In order to determine the real ground state we studied the specific heat, the ac-susceptibility and the resistivity below 2 K. Fig. 3.12 shows the electronic specific heat (C_p/T) versus temperature in the temperature range 0.4 K to 2 K. Below 2 K the electronic specific heat increases with decreasing temperature and it shows two well separated transitions at 0.75 K and 0.55 K. The transition at 0.75 K has a small jump height and its field dependence (see below) proves that it is due to a magnetic transition. The sharper transition at 0.55 K is attributed to the superconducting phase transition, as evidence by ac-susceptibility (right-scale) and resistivity (inset) measurements, which show a pronounced diamagnetic signal and a zero resistivity, respectively. The electronic specific heat coefficient at 0.8 K amounts to $C/T = 0.75$ J/mol K². Thus all these measurements shows the existence of both the magnetic (A-phase) and the superconducting phase (S-phase) in the AS-type single crystal.

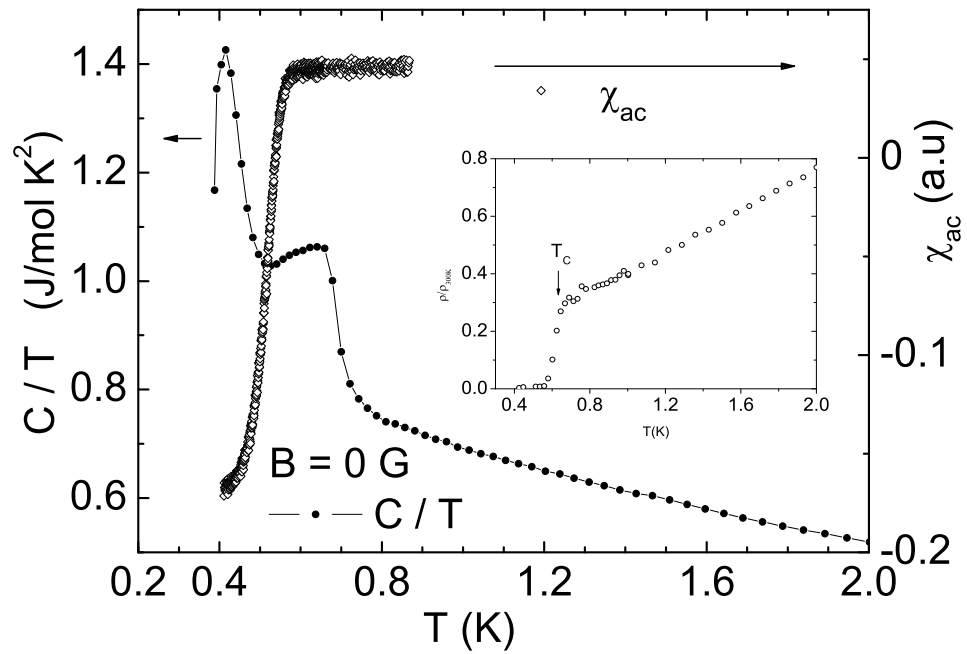


Figure 3.12: Temperature dependence of the specific heat of an A/S type single crystal. It clearly shows two anomalies, a broader one at 0.75 K due to magnetic ordering and a sharp one at 0.5 K due to superconductivity confirmed by ac-susceptibility and electrical resistivity (inset).

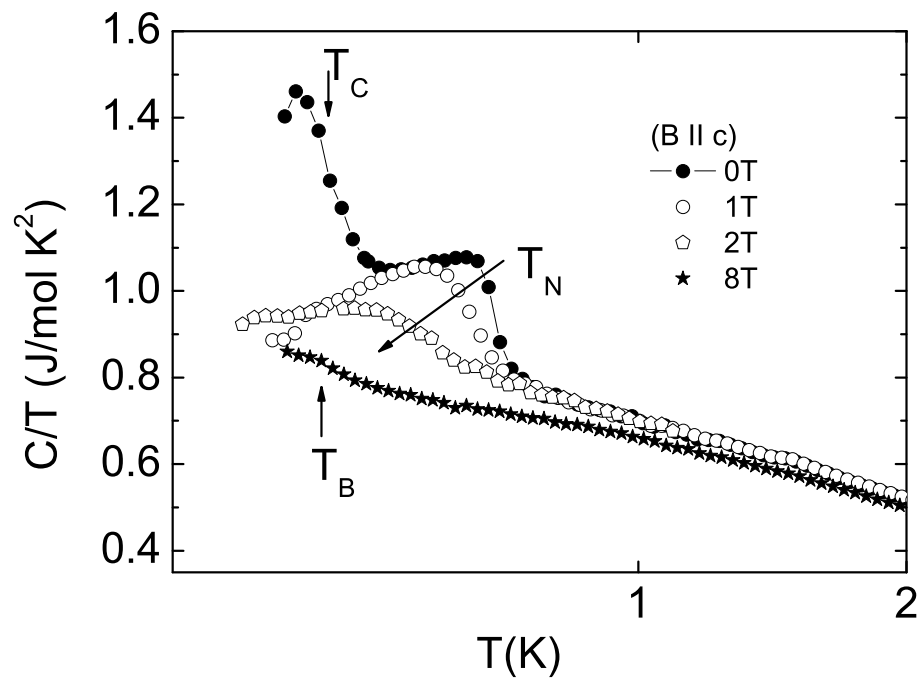


Figure 3.13: Magnetic field dependence of the specific heat of an AS-type CeCu_2Si_2 single crystal. The magnetic ordering anomaly at 0.75 K shifts smoothly to lower temperatures with increasing field and vanishes in a field of 6 T, while the anomaly due to superconductivity disappears already in an applied field of 1 T.

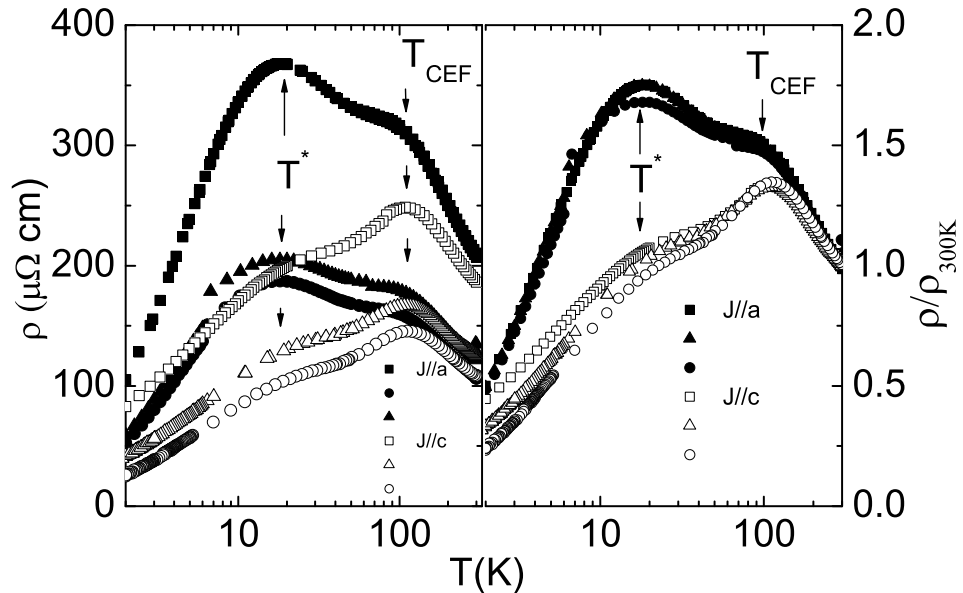


Figure 3.14: The high-temperature electrical resistivity of an AS-type CeCu_2Si_2 single crystal shows the same behavior as that of the A-type. Different symbols represent different crystals from the same batch.

The magnetic field dependence of the specific heat of an AS-type CeCu_2Si_2 single crystal is shown in Fig. 3.13. C/T is plotted as a function of $\log T$ for different field applied along the c axis. With increasing field, the AF transition smoothly shifts to lower temperatures and completely disappears at about 6 T (not shown). On further increasing the magnetic field to 8 T a new phase appears which is likely the B-phase.

The electrical resistivity of AS-type CeCu_2Si_2 was measured on different single crystals from the same batch. Fig. 3.14 shows the high temperature (in the temperature range 2 K to 300 K) electrical resistivity measured with current J both parallel to the a and c axis. On the left side the absolute values are shown while on the right

side the data were normalized to the room-temperature values. The temperature dependencies are similar to those of the A-type CeCu_2Si_2 , with two broad anomalies at $T_{\text{CEF}} \simeq 100$ K and at $T^* \simeq 20$ K, respectively. As for the A-type single crystal, discrepancies of a factor of 2 are observed, while the normalized results are almost identical for different samples of the same batch. The AS-type CeCu_2Si_2 single crystal was annealed at 900 °C for 6 days in order to check the influence on defects by monitoring the resistivity, but no change was observed in the residual resistivity. This shall be discussed in more details later.

In order to study the power law behavior in the resistivity below 4 K, we investigated the low temperature electrical resistivity for both crystallographic directions in the temperature range 0.4 K to 4 K and in zero applied magnetic field (Fig. 3.15). To avoid the anomalies at the transitions we fit the resistivity from 0.9 K to 4 K. The solid lines in Fig. 3.15 show the fit according to $\rho = \rho_0 + AT^n$ with $\rho_0 = 4 \mu\Omega\text{cm}$, $A = 26 \mu\Omega/\text{K}^n$ and $n = 1.07$ for J along a axis and $\rho_0 = 7.4\mu\Omega\text{cm}$, $A = 19.4 \mu\Omega/\text{K}^n$ and $n = 0.822$ for J along the c axis. These power law fits well describe the electrical resistivity from 1 K to 4 K for $J//c$, while for $J//a$ deviations occur above 3.5 K. The values of the residual resistivities and A coefficients will be discussed later.

In order to study the interplay between superconductivity and antiferromagnetic phase, we performed the neutron scattering experiment both as a function of temperature and magnetic field. The propagation vector of the magnetic phase $Q_{AF} = (0.215, 0.215, 0.530)$ in the AS single crystal was determined to be the same as in the A-type single crystal. From the specific heat measurement it becomes obvious that the AS-type CeCu_2Si_2 single crystal has a magnetic phase transition at 0.75 K and a superconducting phase transition at 0.55 K. The neutron diffraction experiments

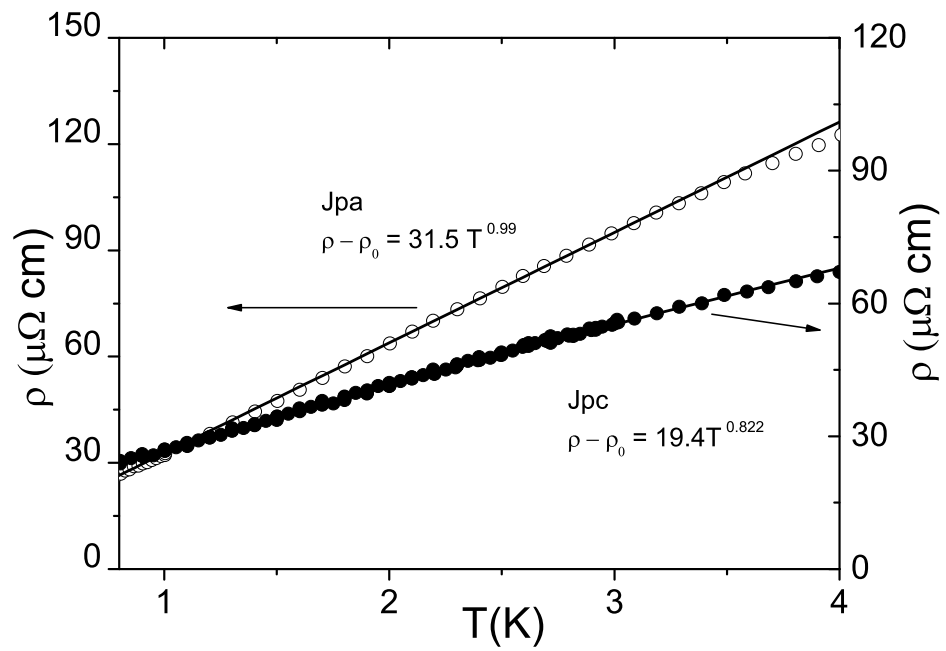


Figure 3.15: Low-temperature electrical resistivity of AS-type single crystal measured below 4 K both for $J//a$ and $J//c$ as a function of temperature. Solid lines show the fits to $\rho = \rho_0 + AT^n$ with $\rho_0 = 4 \mu\Omega\text{cm}$, $A = 26 \mu\Omega/\text{K}^n$ and $n = 1.07$ along the a axis and $\rho_0 = 7.4\mu\Omega\text{cm}$, $A = 19.4 \mu\Omega/\text{K}^n$ and $n = 0.822$ along the c axis.

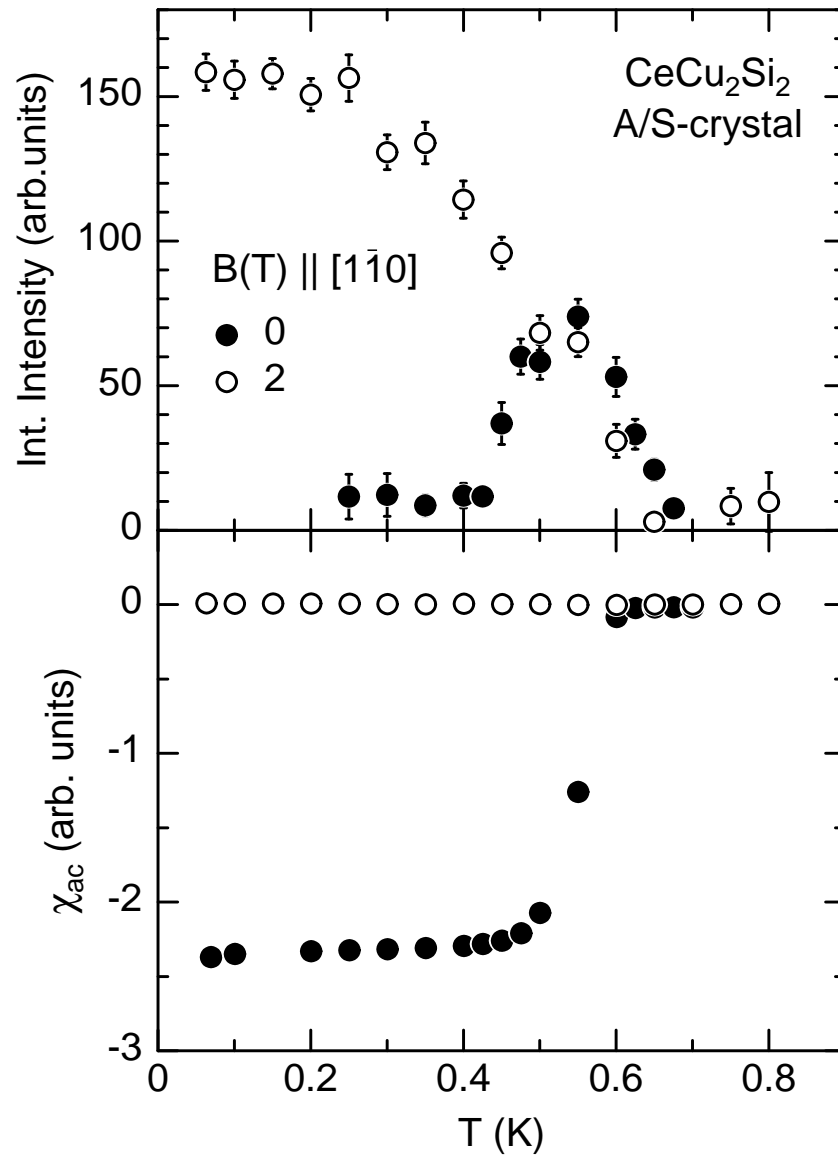


Figure 3.16: Temperature dependence of the integrated magnetic intensity (upper panel) observed at the propagation vector $q = (0.21, 0.21, 0.55)$ for an AS-type CeCu_2Si_2 single crystal in applied fields of 0 T and 2 T, and ac-susceptibility simultaneously measured (lower part).

were performed below temperatures $T = 1$ K and in magnetic fields up to $B = 2$ T at the E4 and E6 diffractometer at the Hahn-Meitner institute, Berlin. In order to control the presence of the superconducting phase we measured the ac susceptibility in-situ, i.e. while doing the neutron diffraction experiment. The summary of the results is shown in Fig. 3.16, where the integrated magnetic peak intensity is plotted as a function of temperature. In zero applied magnetic field the magnetic Bragg peak appears below the Néel temperature, which increases with decreasing T down to 500 mK. However, with further cooling the intensity of magnetic Bragg peak decreases again and disappears at $T = 400$ mK, well inside the superconducting phase. The in-situ ac susceptibility clearly shows the sharp drop due to superconducting diamagnetism and confirms the superconducting phase transition with a midpoint at around 550 mK. Upon applying an upper critical field of 2 T the magnetic Bragg peak reappears. These two measurements confirm the competition of the magnetic and the superconducting phase. However, in an applied field of 1 T and at 50 mK both the superconducting phase and magnetic Bragg peaks can be observed in ac susceptibility and neutron data, respectively. This indicates some coexistence, likely in different parts of the sample, due to phase separation as expected for a first order transition.

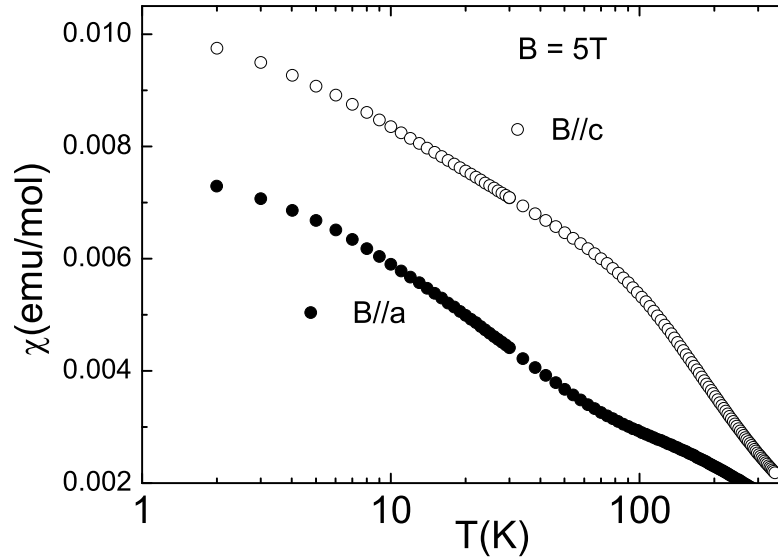


Figure 3.17: Temperature dependence of the magnetic susceptibility of a SA-type CeCu_2Si_2 single crystal in an field of 5 T, applied along both crystallographic axis.

3.2.3 SA-type CeCu_2Si_2

The SA-type CeCu_2Si_2 single crystals were prepared with the initial stoichiometry $\text{Ce}_{1.00}\text{Cu}_2\text{Si}_2$ and Cu flux. These single crystals show superconductivity below 0.7 K in zero applied magnetic field. Detailed results presented below show that in these SA single crystals superconducting transition temperature and magnetic transition temperature are degenerated, i.e. $T_N \simeq T_c \simeq 0.7$ K.

The dc magnetic susceptibility of AS-type CeCu_2Si_2 single crystal in the temperature interval from 2 K to 300 K measured in field of 5 T applied along both crystallographic axis is shown in Fig. 17. The results are again very similar to those observed for the A and the AS single crystals, the absolute values being close to

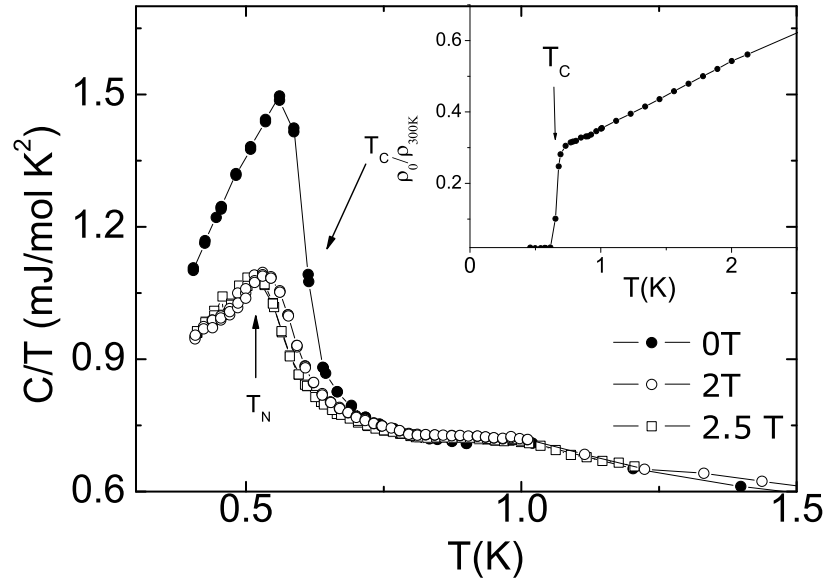


Figure 3.18: Temperature dependence of the specific heat of single crystalline SA-type CeCu_2Si_2 for different fields. The anomaly at 0.65 K for $B = 0$ is due to superconductivity. In field, the transition marks the onset of magnetic order. The inset shows the electrical resistivity confirming that the 0.65 K anomaly is due to superconductivity

those found for the latter one. The high-temperature electrical resistivity of SA-type CeCu_2Si_2 single crystals shows the same behavior as those of the A and AS single crystal (Fig. 3.19).

In order to study the nature of the ground state, we measured the specific heat in zero and finite magnetic fields, applied along an arbitrary direction because of the shape of the single crystal. The low-temperature specific heat in zero, 2 T and 2.5 T is shown in Fig. 3.18 as C/T versus T . The small and broad hump at 1 K which is field independent is of extrinsic origin due to the sample holder. With

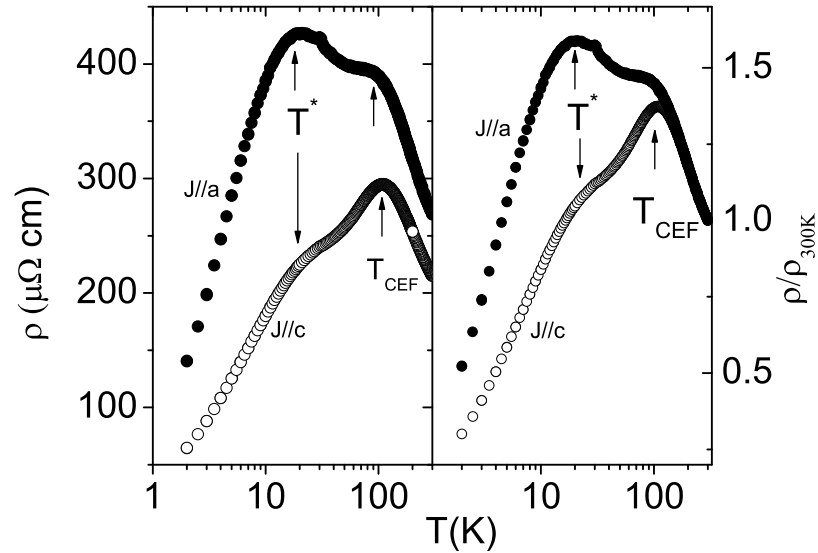


Figure 3.19: The high-temperature electrical resistivity of SA-type CeCu_2Si_2 single crystals shows the same behavior as of the A and AS single crystals.

decreasing temperature the electronic specific heat increases and reaches a value of 750 mJ/mol K^2 at 0.70 K . In zero magnetic field, the large anomaly at 0.6 K with a jump height of $\Delta C \simeq 800 \text{ mJ/mol K}$ indicates the onset of superconductivity. The superconducting phase is confirmed the a low-temperature resistivity measurement which is shown in the inset of Fig. 3.18. The resistivity shows a sharp drop at 0.65 K reveals the superconducting phase transition. The second important finding in our specific heat data is the clear and broad anomaly observed in an applied field of 2 T , which can be attributed to the magnetic transition. With further increasing magnetic field the transition temperature shifts to slightly lower temperatures as expected for the magnetic A-phase.

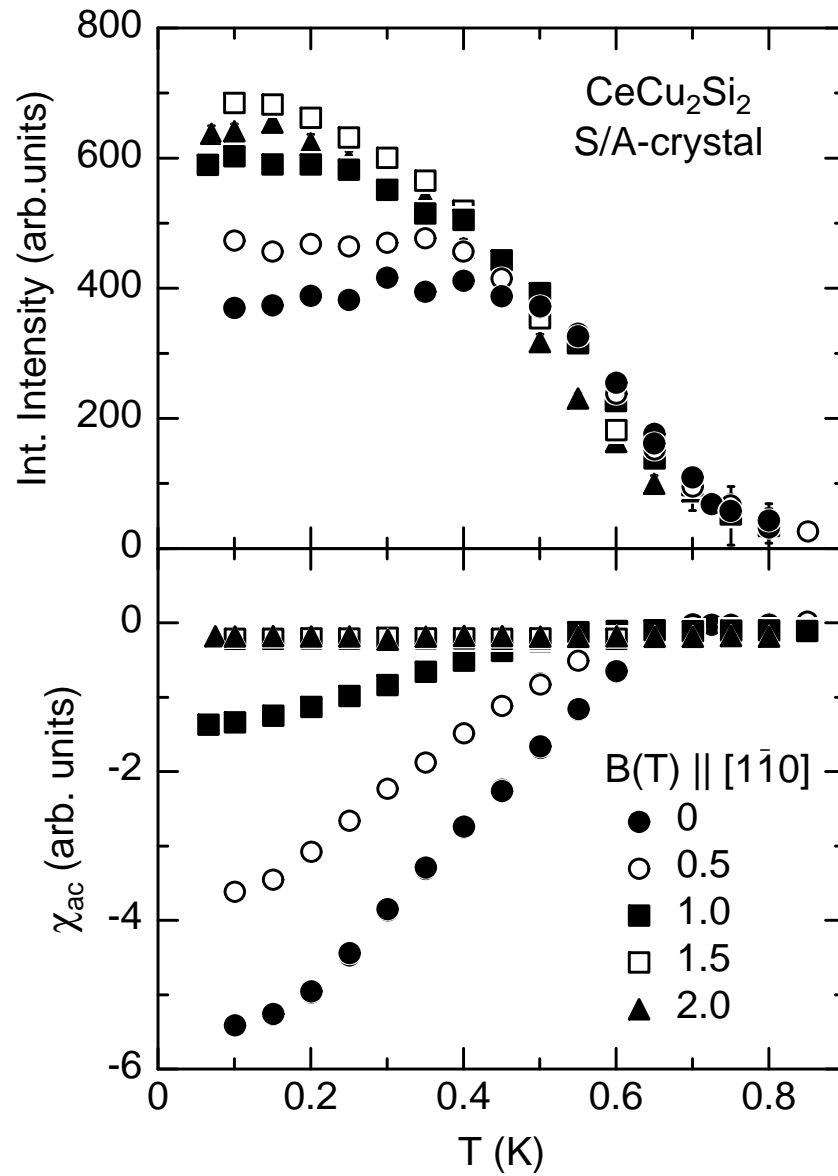


Figure 3.20: Temperature dependence of the integrated magnetic intensity (a.u) at the propagation vector $q = (0.21 \ 0.21 \ 0.55)$ for a SA-type CeCu₂Si₂ single crystal in different applied field magnetic field. Lower part shows the ac-susceptibility measured simultaneously.

To study the relation between the magnetic and the superconducting phase we performed corresponding neutron scattering experiment as for the AS-type single crystal. The neutron scattering experiment was undertaken on the triple-axis spectrometer IN12 at the ILL in Grenoble. The bulk ac-susceptibility measurements were performed simultaneously to the neutron experiments, allowing to check the presence of the superconducting phase. More details on the experimental setup are given elsewhere [33]. The temperature dependence of the integrated magnetic intensity at the propagation vector $q = (0.21 \ 0.21 \ 0.55)$ for the SA-type CeCu_2Si_2 single crystal in different applied magnetic fields ($B//[110]$) is shown in Fig. 3.20, while the lower panel shows the ac susceptibility results. The integrated intensities were obtained by fitting a Gaussian function to the magnetic satellite reflections measured in rocking scans across the magnetic peaks. The antiferromagnetic satellite peaks were observed at the same position $(0.215, 0.215, 1.475)$ as for the A- and AS- type single crystals. In zero magnetic field the magnetic peak intensity increases below 0.7 K, and saturates below 0.4 K. With increasing magnetic field the peak intensity increases further below 0.4 K down to low temperatures. Unlike for the AS-type single crystal, we observed no sharp drop in ac-susceptibility in SA-type as expected for a sharp superconducting phase transition. By contrast, the diamagnetic signal increases linearly with decreasing temperature below 0.6 K, which is possibly due to inhomogeneities of the sample (or very strong pinning?). The linear temperature dependence of the diamagnetic signal suggests the superconducting phase volume fraction to increase with decreasing temperature.

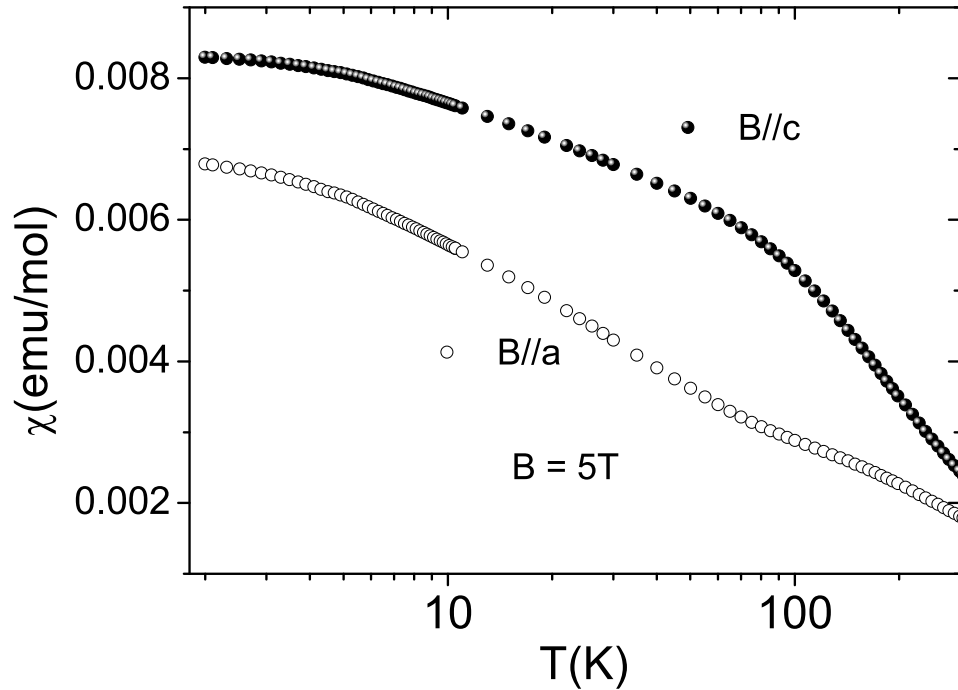


Figure 3.21: Temperature dependence of magnetic susceptibility of S-type CeCu_2Si_2 single crystal in field of 5 T applied along the two crystallographic axis a and c.

3.2.4 S-type CeCu_2Si_2

It was known since long time that with excess of Cu one obtains purely superconducting CeCu_2Si_2 phase (S-type). By taking also an excess of Ce, i.e., $\text{Ce}_{1.05}\text{Cu}_2\text{Si}_2$ and Cu flux we managed to synthesize this type of single crystals. This type exhibits a superconducting phase with a large jump height of nearly 1000 mJ/mol.K^2 in the specific heat at the transition. In this section we show the results from magnetic susceptibility, specific heat, electrical resistivity and neutron measurements obtained on these S type single crystals.

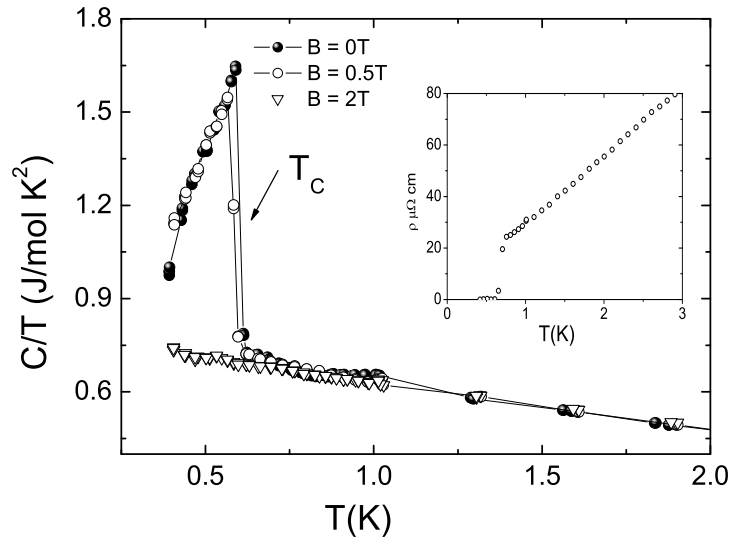


Figure 3.22: Temperature dependence of C/T of a S - type CeCu_2Si_2 single crystal at different magnetic field. One observe a huge anomaly at the superconducting phase transition at 0.6 K with a large jump height of nearly 1000 mJ/mol K which shifts only slightly to lower T at 0.5 T, but disappears in an field of 2T which is just above the critical field. Inset shows the electrical resistivity below 3 K.

The magnetic susceptibility along crystallographic axis c and a is shown in Fig. 3.21 for applied magnetic field of 5 T. Again the data are very similar to the those observed for A-, AS- and SA-type single crystals. The only significant difference is a more pronounced saturation behavior at low temperature, leading to smaller absolute values at 2 K for both directions compared to all other types of CeCu_2Si_2 single crystals. This is in accordance with an even weaker magnetic character.

The electronic specific heat of the S-type CeCu_2Si_2 single crystal is shown in Fig. 3.22, measured in zero and in fields of 0.5 T and 2 T, applied in an unspecific direction. C/T increases with decreasing temperature and reaches a value of $\simeq 770$ mJ/mol K^2

at the onset of superconductivity. The phase transition appears sharp with a large jump height of $\Delta C/T_c \simeq 1000 \text{ mJ/mol K}^2$ which is a hallmark of heavy fermion superconductivity. The superconducting phase transition is confirmed by a resistivity measurement. The results, shown in the inset of Fig. 3.22, evidence a clear and sharp drop of the resistivity to zero at the superconducting phase transition. Upon applying a field of 0.5 T, T_c slightly shifts to lower temperatures while the anomaly vanishes in an applied field of 2 T. Unlike in the other three types no anomaly is found in C/T for 2T field indicating the absence of a magnetic phase. The ratio $\Delta C/(\gamma_n T_c) = 1.3$ is close to the value 1.43 expected for a BCS superconductor. From the low-temperature specific heat data it is clear that in this type of single crystals only the superconducting phase but no long range magnetic ordered phase exist.

The electrical resistivity measured on different single crystals from the same batch in the temperature range 2 K to 300 K with current J parallel to a or c axis is shown in Fig. 3.23. Again, the results are very similar to those obtained for the A, AS and SA single crystals.

To check the power law in the low temperature electrical resistivity, we measured the resistivity below 4 K for $J//a$ and $J//c$. Fig. 3.24 shows the resistivity in the temperature range 0.9 K to 4 K with the power law fit. The resistivity with current along the c axis can be best fitted to the power law $\rho = \rho_0 + AT^n$ with $\rho_0 = 9.1 \mu\Omega\text{cm}$, $A = 23.2 \mu\Omega/\text{K}^n$ and $n = 0.925$. On the other hand, for current along the a axis the best fit is obtained with $\rho_0 = 7 \mu\Omega\text{cm}$, $A = 23\mu\Omega/\text{K}^n$ and $n = 1.07$.

In order to study the existence of a magnetic phase in S-type CeCu_2Si_2 single crystal we performed neutron scattering experiments on the triple-axis spectrometry PANDA at the Munich research reactor FRM-II in Garching. For the experiment we

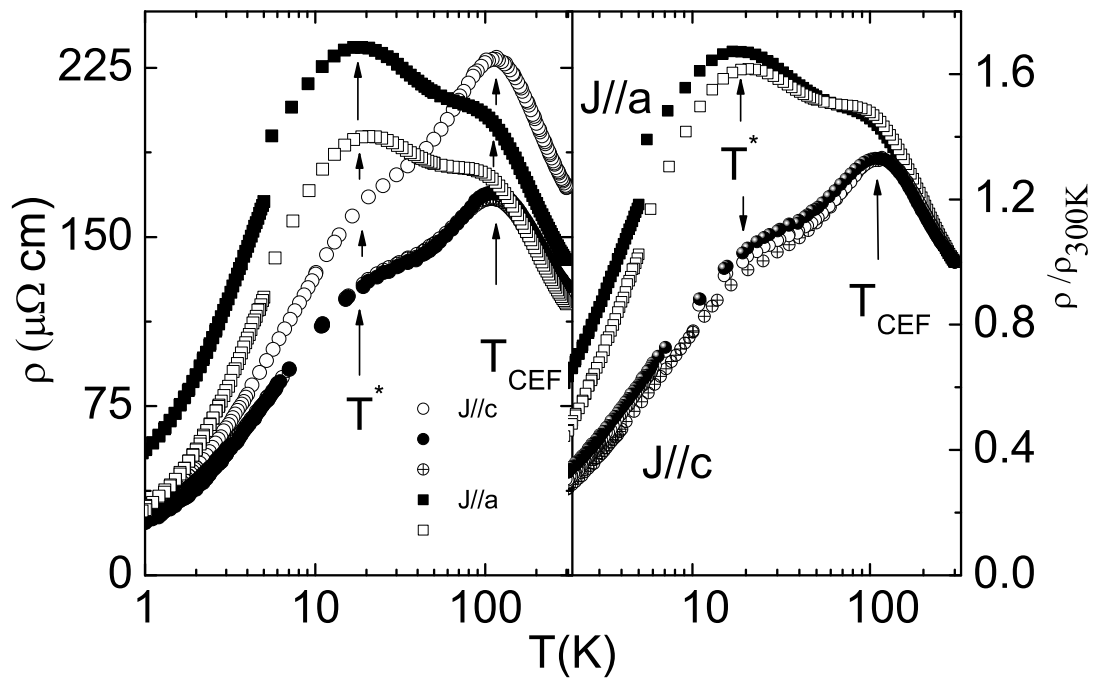


Figure 3.23: The high-temperature absolute (left panel) and normalized (right panel) electrical resistivity of S-type CeCu_2Si_2 single crystals shows the same behavior as those of the A, AS and SA single crystals.

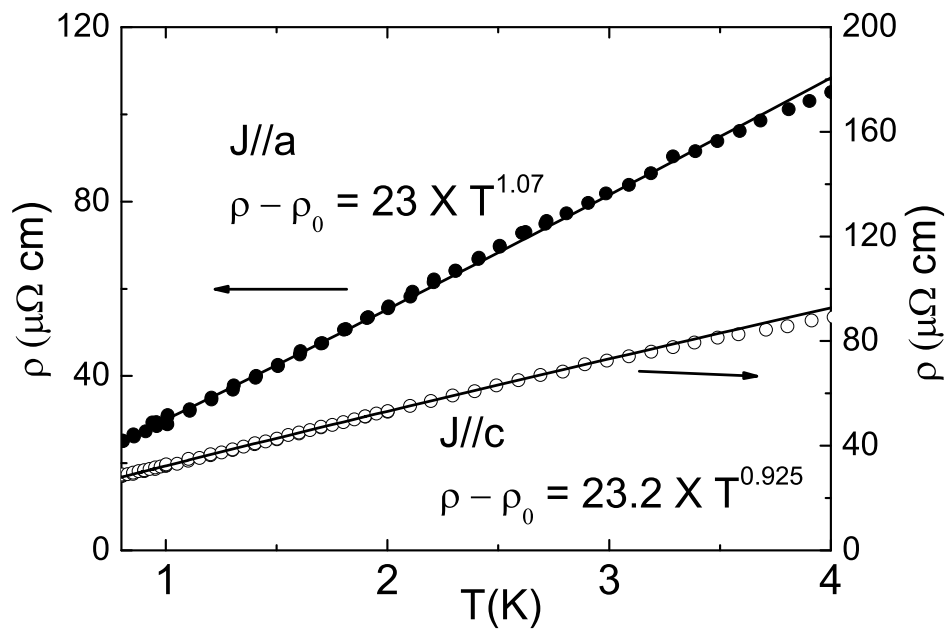


Figure 3.24: Low-temperature electrical resistivity of S-type single crystal measured below 4 K, measured both along $J//a$ and $J//c$ as a function of temperature. Solid line shows the $\rho = \rho_0 + AT^n$ fit with $\rho_0 = 7 \mu\Omega \text{ cm}$, $A = 23 \mu\Omega/\text{K}^n$ and $n = 1.07$ along a axis and $\rho_0 = 9.1 \mu\Omega \text{ cm}$, $A = 23.2 \mu\Omega/\text{K}^n$ and $n = 0.925$ along c axis.

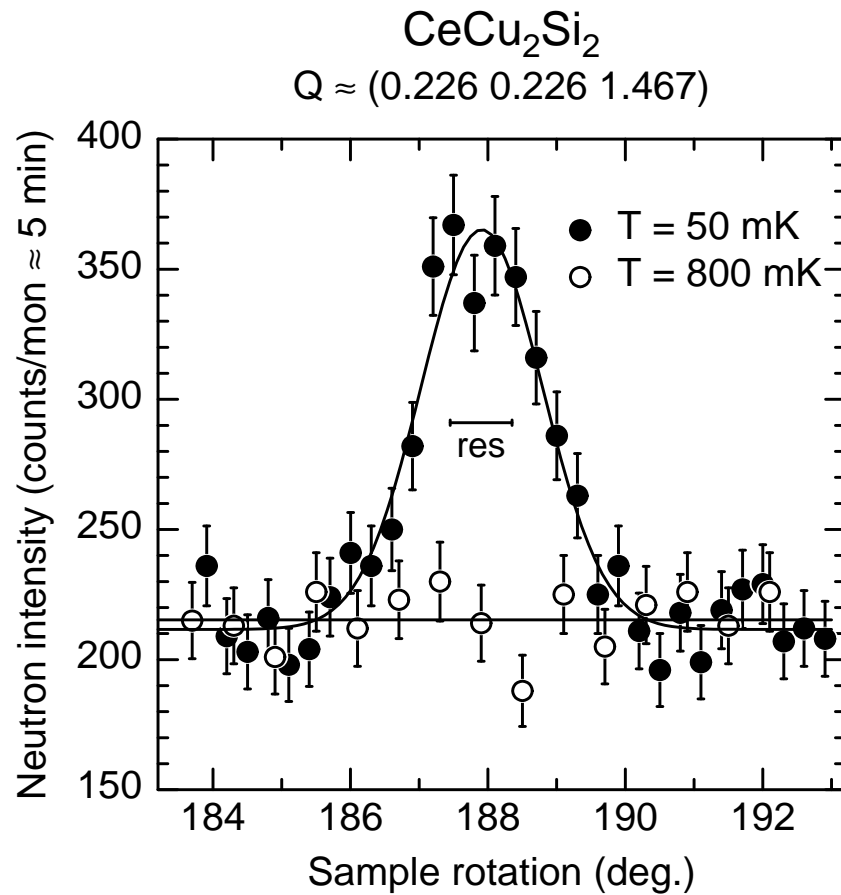


Figure 3.25: Rocking scan across the position of a magnetic satellite peak (0.215, 0.215, 1.47), both below and above superconductivity transition in S-type CeCu_2Si_2 single crystal.

used a single crystal of approx. 2 g mass which shows only a superconducting phase transition and no magnetic phase transition according to specific heat measurements on different samples from the same batch. All these measurements evidenced the same physical properties. Rocking scans at the position $Q=(0.226, 0.226, 1.47)$ were done at two different temperatures 50 mK and 800 mK which is above and below the superconducting transition (cf. Fig. 3.25, res - width of 1 deg). Surprisingly, magnetic short range correlations were observed at the same position where antiferromagnetic superstructure peaks were found in A type or A/S type crystals. At 800 mK we only see the background signal which arises mainly from incoherent nuclear scattering, whereas at 50 mK additional intensity of magnetic origin is clearly observed. The peak is broad and can be best fitted by a Gaussian line shape. The width of magnetic peak is approximately 2θ , which is quite large and corresponds to a correlation length of 50 Å to 60 Å. Interestingly, this is of the same order of magnitude as the superconducting coherence length. The intensity of this magnetic Bragg peak in S-type single crystal is 10 times smaller than the intensity observed in A-type single crystals. These neutron results shall be discussed in more detail later.

In order to study the temperature dependence of the magnetic correlations we investigated the neutron intensity as a function of temperature. The upper part of Fig. 3.26 shows the integrated intensity (a.u) versus temperature plot, and the lower part shows the ac-susceptibility measured simultaneously to the neutron scattering experiment. At 0.8 K, the magnetic correlations starts to appear and increase further with decreasing temperature, even after entering the superconducting phase. Consequently, it is clear that short-range magnetic correlations coexist with the superconducting phase, in contrast to the disappearance of long-range magnetic order

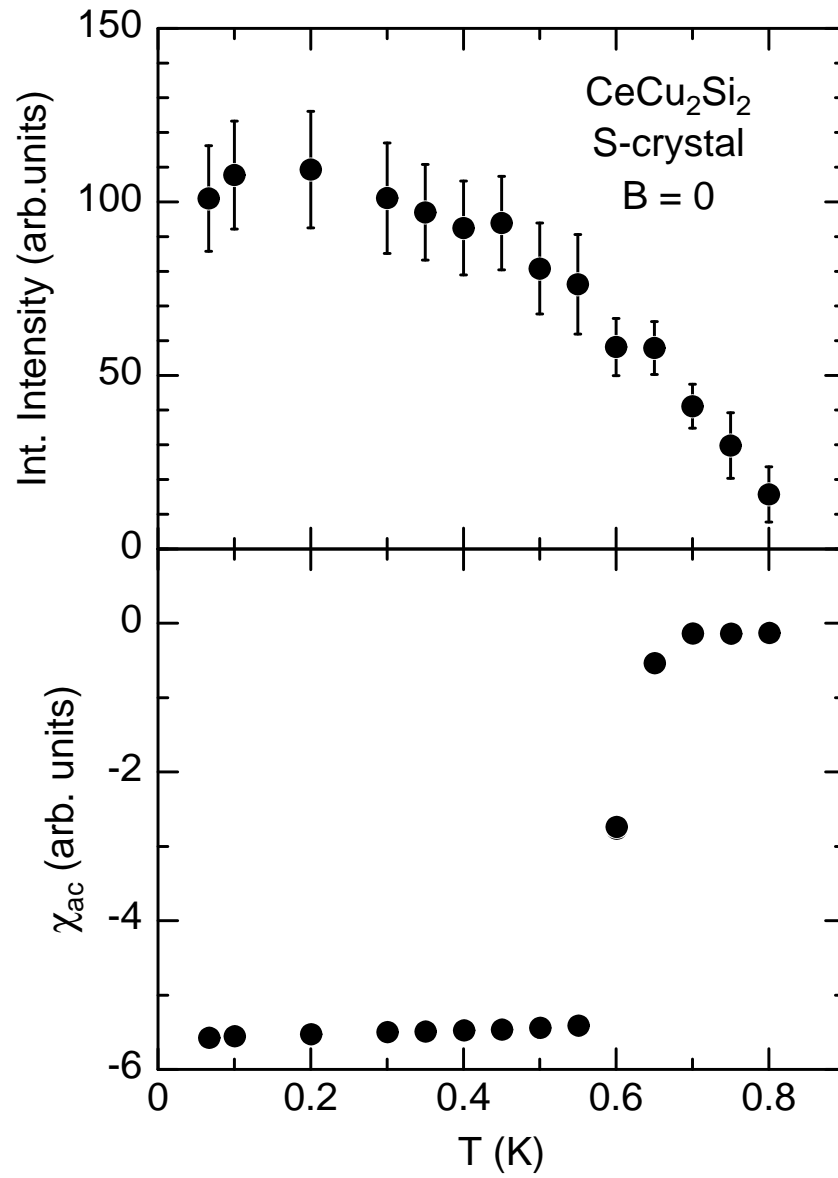


Figure 3.26: Temperature dependence of the integrated magnetic intensity (a.u) at the propagation vector $q = (0.21 \ 0.21 \ 0.55)$ in a S-type CeCu₂Si₂ single crystal in zero field (upper panel), and ac-susceptibility measured simultaneously (lower panel).

in the superconducting phase in AS-type crystals. The simultaneous measurement of ac-susceptibility confirms the superconducting phase transition at 650 mK with a sharp diamagnetic step.

3.3 Discussion

From all the results of the magnetic, thermodynamic, and transport measurements as well as neutron diffraction experiments it is concluded that four different types of ground states in CeCu_2Si_2 single crystals which are called A-type, AS-type, SA-type and A-type. The microscopic investigations by neutron diffraction prove that the A phase is nothing else than an incommensurate long-range antiferromagnetic order with the propagation vector $A_{AF} = (0.215, 0.215, 0.530)$. In AS-type CeCu_2Si_2 this long-range incommensurate antiferromagnetic order competes with the superconducting phase, being ultimately destroyed by the SC phase. For S-type crystals we showed that short-range magnetic correlations coexist with the superconducting phase.

As explained earlier, it is possible to get all the different types of single crystals in the small homogeneity region (< 1 at %) of CeCu_2Si_2 by tuning the Cu:Si ratio. Due to this small homogeneity range it is difficult to determine the difference in the chemical composition between different ground states and no clear difference in lattice parameters has been resolved. The summary of lattice parameters and chemical compositions is given in Table 3.1. It is very clear from Table.3.1 that chemical detection method like Energy Dispersive X-ray Analysis (EDAX) fail to find any composition difference between these different ground states. The systematic study by Geibel et al. [26, 24] resulted in the partial ternary phase diagram of Ce-Cu-Si in which different parts of the homogeneity regions show the different types of ground states. Excess of Cu or Si leads to different ground states and also adds disorder to the system. Basically Cu occupies the Si site or Si goes to the Cu position. Excess of Cu to the system leads to an increase of the hybridization strength between conduction and f- electron, since the 3d electrons of Cu (although slightly below the

Fermi-level) lead to a stronger hybridization than p or s electrons. Since EDAX and XRD fail to resolve chemical difference between different ground states, we looked at the residual resistivity ratio (RRR) in more detail. The RRR should be sensitive to the disorder induced by slight deviations from the stoichiometry. Thus, one expects a clear differences in RRR for different ground state properties. Due to magnetic and superconducting phase transitions it is difficult to determine the absolute value to the residual resistivity value. Therefore we took the resistivity ratio at 2 K and just above the transitions.

Table 3.1: Lattice parameters and chemical compositions of different types of CeCu_2Si_2 single crystals

Type	a (Å)	c (Å)	volume V (Å ³)	Composition Ce:Cu:Si
A type	4.100	9.931	166.96	19.99:39.42:40.15
AS type	4.099	9.922	166.71	19.76:39.58:40.8
SA type	4.101	9.924	166.95	19.81:39.28:40.89
S type	4.101	9.919	166.84	19.80:39.26:40.77

Fig. 3.27 shows the dependence of these resistivity ratios for both current directions on the starting Ce concentration as well as the relation to the different ground state properties. The open circles and squares mark ρ_{2K}/ρ_{300K} while the closed circles and squares indicate ρ_{LT}/ρ_{300K} (LT - Low temperature, just above the transitions). A Ce concentration of 0.9 in the starting melt shall lead to an excess of Si in the resulting single crystal, while a Ce concentration of 1.05 shall lead to a sample with

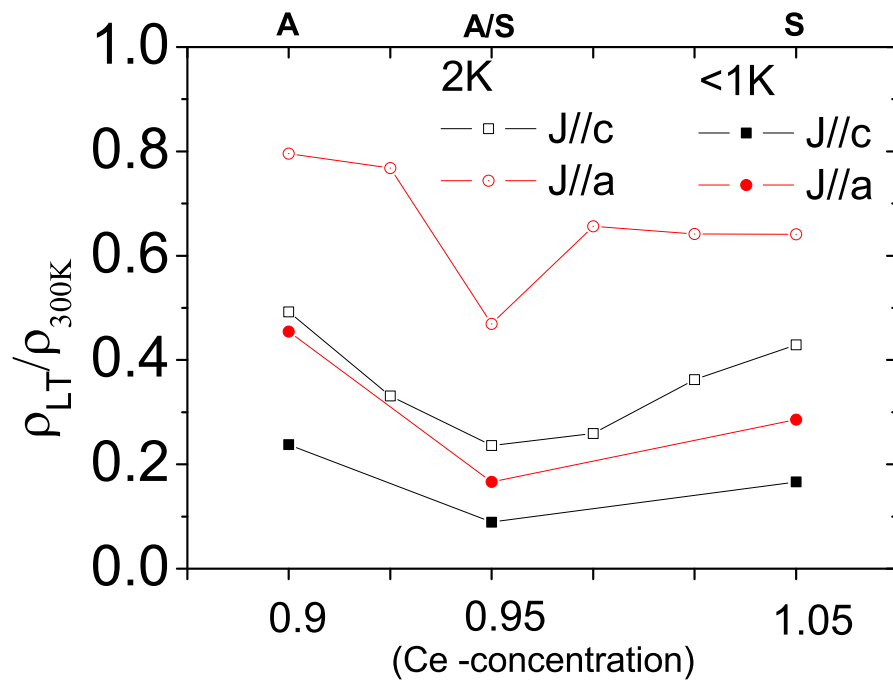


Figure 3.27: Evolution of the resistivity ratio with composition. The plots show the inverse residual resistivity ratio at 2 K (open symbols) and at low temperature 0.8 K (closed symbols). Squares and circles are for $J//a$ and $J//c$, respectively.

Cu excess. In both cases one would therefore expect a large residual resistivity, i.e. a large ρ_{LT}/ρ_{300K} ratio. This is exactly the results we observe in Fig. 3.27.

Table 3.2: Residual resistivity ratio measured for $J//a$ and $J//c$ on different types of $CeCu_2Si_2$ single crystals.

Type	$\rho_{300K}/\rho_{2K}(J//a)$	$\rho_{300K}/\rho_{2K}(J//c)$	$\rho_{300K}/\rho_{LT}(J//a)$	$\rho_{300K}/\rho_{LT}(J//c)$
A-type	1.25	2	2.2	4.2
S-type	1.56	2.33	3.51	6
SA-type	1.53	3.86	—	—
AS-type	2.13	4.23	6	11.2

In Table 3.2 the results are arranged according to increasing RRR. Both, Table 3.2 and Fig. 3.27 clearly show that the resistivity ratio is always larger for $J//c$ than for $J//a$. The AS-type $CeCu_2Si_2$ shows the largest RRR. Thus, this single crystal with AS behavior is likely closest to the true stoichiometric composition. Besides the single crystals presented in details in the previous paragraphs, we grew further ones at intermediate starting concentration, i.e $Ce_{0.925}$, $Ce_{0.975}$ and $Ce_{1.00}$, in order to look in more details at the evolution of the properties. Both, the evolution of the resistivity values and the evolution of the magnetic and superconducting phases follow the scheme established with the results of the previous paragraphs. Increasing the starting Ce content leads to a continuous increase of the Cu-content in the single crystals. This results in a continuous weakening of the magnetic A phase and a continuous strengthening of the superconducting phase. From these results it is clear

that one can control the ground state of CeCu_2Si_2 single crystals by tuning the Ce content in a flux crystal growth method. This is in agreement with polycrystal results where tuning the ground state was done by varying Cu and Si contents.

Non-Fermi-liquid (NFL) behavior demonstrates itself in the power-law behavior of physical properties, with exponents different from those of a Fermi liquid. As already mentioned, in order to study the power law in resistivity, we fit the resistivity data in the temperature range 0.9 K to 4 K for A-type, AS-type and S-type crystals. The presence of the magnetic and/or superconducting transitions prevents using the data below 0.9 K, which results in some uncertainty in ρ_0 , A and the exponent. However, for a comparative analysis of the different types of single crystals this effect is not important. More critical is the large difference in the absolute values of $\rho(T)$, which results in a large scattering in the absolute ρ_0 and A values. In order to be able to compare the data we normalized the real A coefficient using an absolute value for the room temperature resistivity of $100\mu\Omega\text{cm}$, i.e., $A^* = 100 \mu\Omega\text{cm} * A/\rho_{300\text{K}}$ where $\rho_{300\text{K}}$ is the measured ρ at 300 K of that single crystal.

Table 3.3. shows all the parameters of the power law fit for different ground states. The room temperature resistivity $\rho_{300\text{K}}$ for both current along $J//a$ and $J//c$ are all in the range 100 to 200 $\mu\Omega\text{cm}$. The A coefficient, which corresponds to the increment in $\rho(T)$ at $T = 1$ K for all n, is clearly anisotropic between the a and c axis, being larger along a than along c. This is even more evident for the normalized A^* values. The last column shows the normalized A coefficient multiplied with the exponent n. This product corresponds to the normalized slope $\delta\rho/\delta T$ at $T = 1$ K. Remarkably, all different types of crystals present the same value $\simeq 12 \mu\Omega\text{cm}/\text{K}^n(\pm 1)$ for this slope for $J//c$, and a much larger value $\simeq 24 \mu\Omega\text{cm}/\text{K}^n(\pm 3)$ for $J//a$. The exponent n

is always close to one and does not show any large change. One can notice that it is always larger along a than along c . NFL theories predict a lowest limit of 1 for the exponent in the T dependence of the resistivity at low T . Thus, n values below one seem to be quite surprising. However, the contradiction is that we consider here the T range above T_N , not the limit $T \Rightarrow 0$. For the power law above T_N , using a very primitive approach, one expects the exponent decrease from $n = 2$ (Fermi liquid behavior in a paramagnetic Kondo lattice) to $n = 0$ (T -independent spin scattering in the paramagnetic state of 4f intermetallic compound with well localized 4f moment) [38], when the hybridization strength decreases from a large value to a small one. The general trend of a slightly decreasing n from S-type to A-type CeCu₂Si₂ single crystals is thus in good agreement with an increasing magnetic character.

Table 3.3: Residual resistivity, A coefficient, A* normalized to a room temperature resistivity $\rho_{300} = 100 \mu\Omega\text{cm}$ and exponent n .

Type	$\rho_{300K}(\mu\Omega\text{cm})$	$\rho_0(\mu\Omega\text{cm})$	$A(\mu\Omega/\text{K})^n$	$A^*(\mu\Omega/\text{K})^n$	n	$A^* \times n (\mu\Omega/\text{K})^n$
A-type -J//a	108	5	35	32	0.87	27.8
-J//c	123	8	17.5	14	0.83	11.6
AS-type -J//a	127	4	26	20	1.07	21.4
-J//c	125	7.4	19.4	15	0.822	12.3
S-type -J//a	120	7	23	19	1.07	20.3
-J//c	190	19	23.2	12	0.925	11.1

Fig. 3.28 shows the temperature dependence of the C/T of single crystalline CeCu₂Si₂ for all the four types, namely A-type, AS-type, SA-type and S-type. The specific heat (closed circle) of A-type shows a magnetic transition at 850 mK, which is marked by an arrow with T_N . The specific heat of the AS-type presents two well separated anomalies, one at 750 mK due to the magnetic transition (T_N) and another

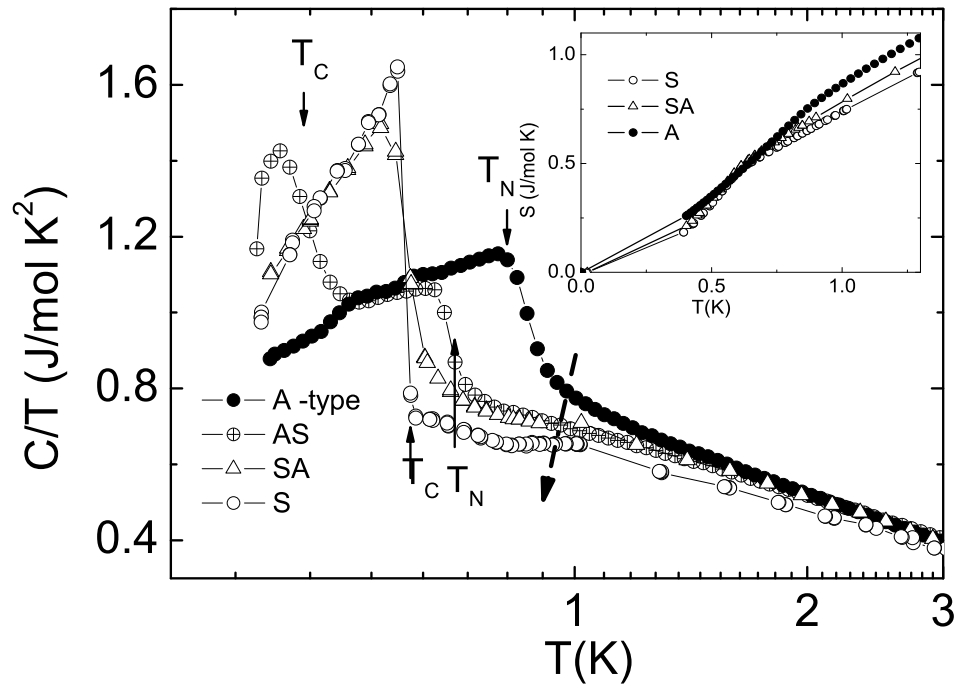


Figure 3.28: Comparison of the temperature dependence of the specific heat of A-type, AS-type, SA-type and S-type CeCu_2Si_2 single crystals. Arrows show anomalies corresponding to magnetic ordering (T_N) and superconducting ordering (T_C). The inset shows the calculated entropy of all four crystal types up to 1.5 K.

one at 550 mK due to superconducting transition (T_c). SA- and S-type crystals show only one anomaly at the same temperature. The only difference is that the jump height for the S-type is larger compared to the one of the SA-type. More interestingly, C/T decreases just before the transition from the magnetic (A-type) to the superconducting (S-type) phase. These results were confirmed by pressure experiments. E. Lengyel et al. [34] measured the electronic specific heat of an AS-type single crystal under isostatic pressure up to 2.03 GPa. They observed a decrease in C/T at 0.7 K (above the magnetic or the SC transition) by 50 % upon increasing the pressure to 2.03 GPa. The magnetic phase disappears at a small pressure $\simeq 0.1$ GPa, while T_c initially increases before reaching a maximum with further increasing the pressure, then slightly decreases up to pressure $\simeq 2$ GPa, but increases again above 2 GPa. The decrease in electronic specific coefficient from A-type to S type can be related to the increase of the Kondo energy scale upon strengthening the 4f-conduction electron hybridization by applying pressure or substituting Cu for Si. The inset of Fig. 3.26 shows a plot of the entropy $S(T)$ versus temperature. $S(T)$ was calculated for all four types of CeCu_2Si_2 up to temperature 1.5 K. The entropy between $T = 0$ K and the low- T limit of the $C(T)$ measurement were estimated by extrapolating the measured $C(T)$ down to $T = 0$ by using a power law. All entropy plots cross at $\simeq 0.8$ K, which basically reflects the conservation of entropy above the transitions. Since quite a large part of this entropy is involved in either the magnetic or the SC transition, it indicates that the 4f - electrons are involved in both. It is very clear that above 0.9 K, a higher entropy is accumulated for the A-type crystal as expected since it has a smaller Kondo energy scale compared to the S-type.

The ratio $\Delta C/(\gamma_n \cdot T_c)$ (Table 3.4), which gives hints for superconducting coupling

strength, was calculated for S-type and SA-type samples. Furthermore, we also calculated the ratio $\Delta C_{\text{TN}}/\gamma_n(T_{\text{N}})$. As a consequence of the large increase of $\Delta C_{\text{Tc}}/(T_{\text{c}})$ from 0.4 J/mol.K² in AS-type to 0.7 J/mol K² in SA and 1 J/mol.K² in S-type single crystals as well as a small decrease of γ_n , the ratio $\Delta C_{\text{Tc}}/(\gamma_n T_{\text{c}})$ increases even more from AS to S type, i.e., from 0.5 to 1.4. We suspect that this increase is likely not due to an increase of coupling strength, but to an increase of the part of the Fermi surface involved in the formation of the SC state. The ratios for the magnetic transition at T_{N} are much smaller, which is common for SDW ordering since only part of the Fermi surface is involved in the formation of the SDW state. The ratio at T_{N} decreases from the A to the SA type, also likely reflecting a reduction in the part of the involved Fermi surface rather than a decrease of the coupling strength.

Table 3.4: $\Delta C/(\gamma_n T_{\text{c}})$ and $\Delta C/(\gamma_n T_{\text{N}})$ for different type of CeCu₂Si₂

Type	$\Delta C/(\gamma_n T_{\text{N}})$	$\Delta C/(\gamma_n T_{\text{c}})$
A-type of CeCu ₂ Si ₂	0.7	-
AS-type of CeCu ₂ Si ₂	0.58	0.5
SA-type of CeCu ₂ Si ₂	0.79(2T)	0.81
S-type of CeCu ₂ Si ₂	-	1.4

Before describing the nature of the magnetic phase in CeCu₂Si₂, we would like to comment on the low-temperature resistivity measurements on A-type single crystals. In order to check for superconductivity in the A-type we performed low-temperature resistivity and specific heat measurements. Fig. 3.29 shows the low-temperature specific heat down to 50 mK while the inset shows the resistivity measured down to 50

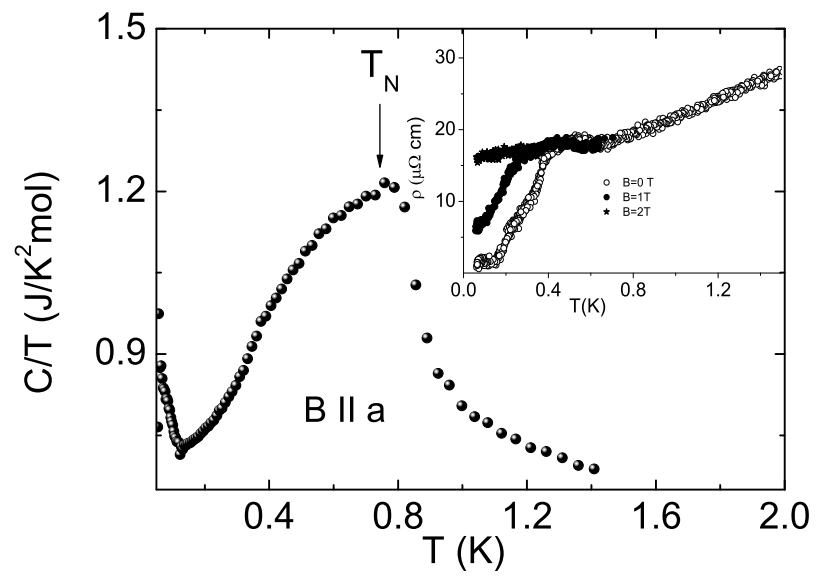


Figure 3.29: Low-temperature specific heat down to 50 mK of the A-type CeCu_2Si_2 . Inset shows the resistivity measured down to 50 mK on the same sample.

mK in different magnetic field. The broad anomaly at 850 mK in the specific heat corresponds to the magnetic transition while no clear anomaly is found down to 100 mK. The upturn below 100 mK is attributed to nuclear contributions, thus there is no clear sign for bulk superconductivity in this sample. But low-temperature resistivity data show a broad drop at 400 mK, where $\rho(T)$ linearly decreases with decreasing temperature. This suggests that only a minor part of the sample undergoes a superconducting transition but the bulk of the crystal remains in the magnetic phase. In an applied magnetic field of 1 T, T_c shifts to lower temperature and the superconducting transition vanishes in a magnetic field of 2 T. After this note on disorder or inhomogeneity effects and on the bulk nature of the magnetic and superconducting phases we now describe the nature of the A phase.

Nearly 10 years after the discovery of superconductivity in CeCu_2Si_2 , muon-spin-rotation (μSR) [3] and nuclear magnetic resonance (NMR) [2] measurements found a further ordered phase of magnetic in nature, with slowly fluctuating moments of the order of $0.1 \mu_B$. Furthermore this magnetic phase was suggested to be a "spin density wave". But despite many attempts, no magnetic Bragg peaks could be observed in neutron scattering experiments. Recently resistivity measurements [31] also give some evidence for a spin density wave, because of an upturn in resistivity at the transition indicating the opening of a gap in the Fermi surface. As explained in the paragraph on neutron experiments, now we succeed to find the magnetic Bragg peaks thanks to the availability of large single crystals. We determined the propagation vector $(0.215 \ 0.215 \ 0.530)$, which corresponds to an incommensurate antiferromagnetic phase. The experimental data could be well accounted for by assuming a sinusoidal modulation of the ordered magnetic moments lying in the basal plane, with an estimated ordered

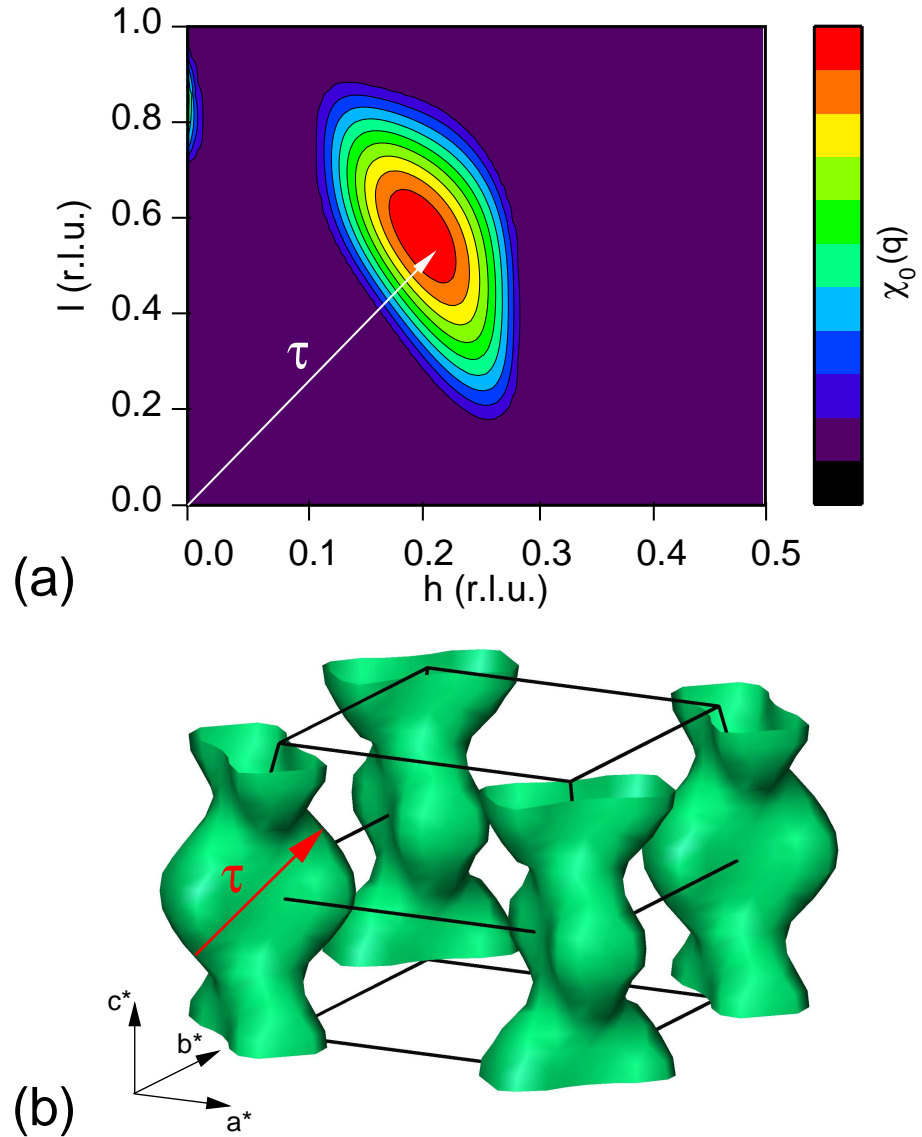


Figure 3.30: (a) Calculated static susceptibility in the (hhl) plane using a renormalized band structure. τ is the experimentally observed propagation vector. (b) Fermi surface of heavy quasiparticles calculated with renormalized band method showing the nesting for incommensurate wave vector $\tau = (0.21 \ 0.21 \ 0.55)$ within the columnar Fermi surface.

moment of the order $\simeq 0.1 \mu_B$.

Zwicknagl et al. calculated the band structure of CeCu_2Si_2 using the renormalized band method [35, 36]. In this method the width of the quasiparticle band is adjusted to the experimentally observed specific heat coefficient $C/T \simeq 700 \text{ mJ/mol K}^2$. In CeCu_2Si_2 they find two sheets for the Fermi surface one with heavy and one with light quasiparticles. It is the instability in the heavy Fermi surface which leads to antiferromagnetic order. Fig. 3.30a shows the q wave vector dependence of the static susceptibility calculated using renormalized band theory. The calculated q dependent static susceptibility shows a clear maximum at the same position as the experimentally observed propagation vector. Fig. 3.30b shows the heavy Fermi surface sheet of CeCu_2Si_2 , which consists of cylinders along the c axis. The pronounced maximum in the static susceptibility at Q_{AF} is due to nesting of the Fermi surface for this propagation vector. Thus, the experimental propagation vector of A-phase agrees well with the maxima position of the calculated static susceptibility. This is a strong evidence for the SDW nature of the A-phase.

In order to investigate the relation between the magnetic correlations and the superconducting phase, elastic and inelastic neutron scattering experiment on S-type CeCu_2Si_2 single crystals were performed at the triple-axis spectrometer PANDA (Munich research reactor FRM-II in Garching). As already shown in Fig. 3.26, the intensity in the elastic channel as a function of sample rotation in S-type across the $(0.226, 0.226, 1.467)$ position indicates short-range magnetic correlations inside the superconducting phase. In order to know more about the relation between the short range correlations and superconducting phase we proceeded to the inelastic neutron scattering. More results and a detailed discussion of this subject can be found in [37].

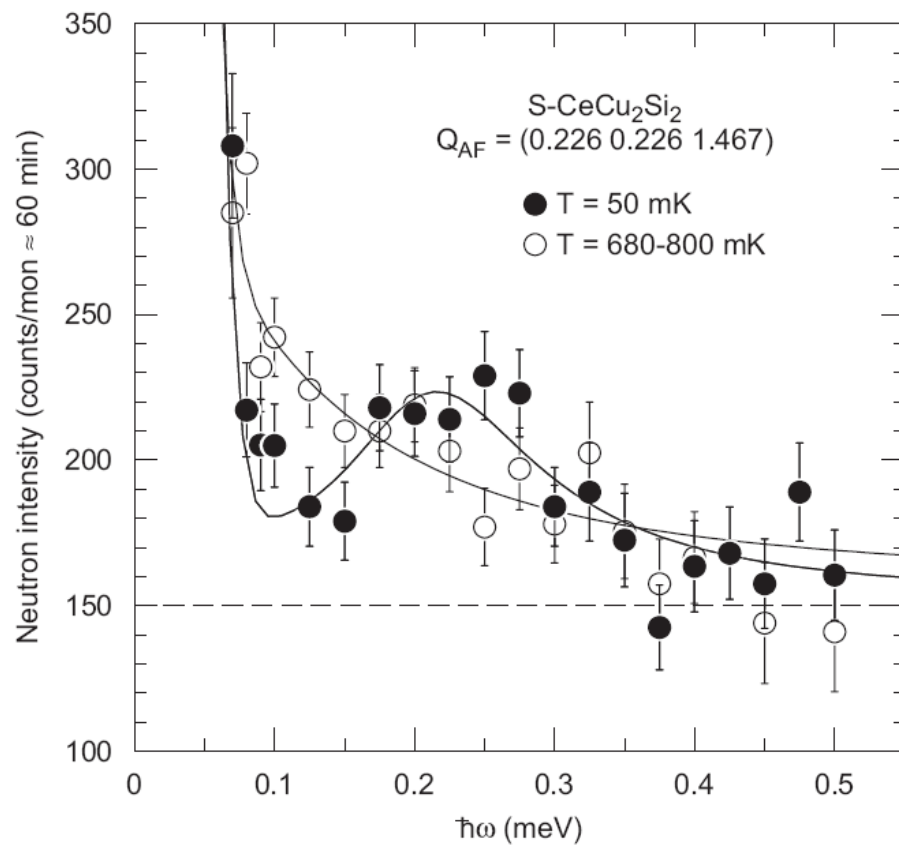


Figure 3.31: Inelastic neutron spectra observed for a S-type single crystal at the AF propagation vector.

In Fig. 3.31 we show the scattering intensity as a function of the energy transfer in the range 0 to 0.5 meV for two different temperatures, far below T_c at 50 mK and just above T_c at $\simeq 700$ mK. At 50 mK a double-peak structure is detected, with an elastic line, which remains at 700 mK and an inelastic peak at $\simeq 0.2$ meV which disappears at 700 mK. The elastic line is due to both incoherent scattering and to the coherent scattering associated with the short-range order below 800 mK (see Fig. 3.25 and 3.26). It can be well fitted by Gaussian line shape [37]. The excitation at 0.2 meV which can be well fitted with a Lorentzian line shape seems to be directly associated with the superconducting state, as it disappears at T_c . Since it is observed at the location of the propagation vector observed for the magnetic state in the A and AS phase, it indicates a connection between the interaction leading to the magnetic state and the superconducting state. Taking the center of this inelastic peak as a rough measure for the superconducting gap, one obtain $2\Delta \simeq 4k_B T_c$ which is in good agreement with the predictions for a weak-coupling d-wave superconductor. In the normal state above T_c the inelastic peak is replaced by a quasielastic line which is expected for a fluctuating local moment system.

3.4 Conclusions

In this work we have successfully grown single crystals of CeCu_2Si_2 with precise and controlled low- T physical properties and masses up to 5 g. As explained it is difficult to find any systematic differences either in chemical analysis or in the lattice constants for the different ground states. But there is a clear relation between the ground state and residual resistivity ratio, which reflects the disorder in the system. These results show that the Cu:Si ratio can be well tuned by Cu in the self-flux crystal growth method by tuning the Ce content. The magnetic susceptibility for different types of single crystal shows a small but systematic dependence, being largest for the A-type and smallest for the S-type. The electronic specific heat clearly demonstrates four different ground state with a broader and smaller anomaly in A-type due to a magnetic transition and a sharper and much larger anomaly in S-type due to a superconducting transition. C/T is larger just above the transition in the A-type single crystal and smallest for S-type, indicating an increase of the Kondo scale from A to S type. This increase in C/T is also in agreement with the results from pressure measurements. The low-temperature resistivity shows a non-Fermi liquid behavior above T_N or T_c , with an almost T -linear behavior below 3.5 K. The exponent in the power law decreases from S to A type, and is slightly larger for current in the basal plane than for current along c axis. The most important results is that our large single crystals allowed for the first time the successful observation of the magnetic Bragg peaks in the A-type single crystal. This proves that the A phase is nothing but a long-range incommensurate antiferromagnetic phase with a propagation vector $(0.21 \ 0.21 \ 0.54)$. In AS-type single crystals, long-range magnetic order compete

with superconducting phase, i.e. the magnetic order gets suppressed by the superconducting phase. Interestingly, short-range magnetic correlations coexist with the superconducting phase in S-type single crystals. First inelastic neutron experiments show a possible relation between the superconducting and magnetic phases evidenced by the formation of a spin excitation gap in the magnetic excitation spectra at the antiferromagnetic propagation vector below T_c .

Bibliography

- [1] F. Steglich, J. Aarts, C. D. Bredl, W. Lieke, D. Meschede, W. Franz and H. Schäfer, Phys. Rev. Lett. **43**, 1982 (1979).
- [2] H. Nakamura, Y. Kitaoka, H. Yamada, K. Asayama, J. Magn. Magn. Mater. **76-77**, 517 (1988).
- [3] Y. J. Uemura, W. J. Kossler, X. H. Yu, H. E. Schone, J.R. Kempton, C.E. Stronach, S. Barth, F. N. Gygax, B. Hitti, A. Schenck, C. Baines, W. F. Lankford, Y. Onuki, T. Komatsubara, Phys. Rev. B. **39**, 4726 (1989).
- [4] B. Bellarbi, A. Benoit, D. Jaccard, J. M. Mignot, H. F. Braun, Phys. Rev. B **30**, 1182 (1984).
- [5] F. Thomas, C. Ayache, I.A. Fomine, J. Thomasson, C. Geibel, J. Phys.: Condens. Matter **8**, 51(1996).
- [6] K. Miyake, O. Narikiyo, and Y. Onishi, Physica B **259-261**, 676 (1999).
- [7] D. Jaccard, H. Wilhelm, K. Alami-Yadri, and E. Vargoz, Physica B **259-261**, 1 (1999).

- [8] E. Vargoz, D. Jaccard, J. Y. Genoud, J. P. Brison, and J. Flouquet, *Solid State Commun.* **106**, 631 (1998).
- [9] J. Thomasson, Y. Okayama, I. Sheikin, J. P. Brison and D. Braithwaite, *Solid State Commun.* **106**, 637 (1998).
- [10] E. Vargoz and D. Jaccard, *J. Magn. Magn. Mater.* **177-181**, 294 (1998).
- [11] D. Jaccard, K. Behnia and J. Sierro, *Phys. Lett. A* **163**, 475 (1992).
- [12] N. D. Mathur, F. M. Grosche, S. R. Julian, I. R. Walker, D. M. Freye, R. K. W. Haselwimmer, and G. G. Lonzarich, *Nature* **394**, 39 (1998).
- [13] S. Araki, M. Nakashima, R. Settai, T. C Kobayashi and Y. Onuki, *J. Phys.: Condens. Matter* **14**, L377 (2002).
- [14] C. Petrovic, P. G. Pagliuso, M. F. Hundley, R. Movshovich, J. L. Sarrao, J. D. Thompson, Z. Fisk, and P. Monthoux, *J. Phys.: Condens. Matter* **13**, L337 (2001).
- [15] C. Petrovic, R. Movshovich, M. Jaime, P. G. Pagliuso, M. F. Hundley, J. L. Sarrao, Z. Fisk, J. D. Thompson, *Europhys. Lett.* **53**, 354 (2001).
- [16] H. Hegger, C. Petrovic, E. G. Moshopoulou, M. F. Hundley, J. L. Sarrao, Z. Fisk, and J. D. Thompson, *Phys. Rev. Lett.* **84**, 4986 (2000).
- [17] I. R. Walker, F. M. Grosche, D. M. Freye and G. G. Lonzarich, *Physica C* **282-287**, 303 (1997).
- [18] E. Bauer, G. Hilscher, H. Michor, Ch. Pau, E. W. Scheidt, A. Griбанov, Yu. Seropegin, H. Noe M. Sigrist, and P. Rogl, *Phys. Rev. Lett.* **92**, 027003 (2004).

- [19] K. Izawa, Y. Kasahara, Y. Matsuda, K. Behnia, T. Yasuda, R. Settai, and Y. Onuki, Phys. Rev. Lett. **94**94, 197002 (2005).
- [20] M. Yogi, Y. Kitaoka, S. Hashimoto, T. Yasuda, R. Settai, T. D. Matsuda, Y. Haga, Y. Onuki, P. Rogl, and E. Bauer, Phys. Rev. Lett. **93**, 027003 (2004).
- [21] G. Motoyama, S. Yamamoto, Y. Oda, K. Ueda, T. Kohara, Physica B **359-361**, 187 (2005).
- [22] M. Ishikawa , H. F. Braun, and J. L Jorda, Phys. Rev. B **27**, 3092 (1983).
- [23] R. Modler, M. Lang, C. Geibel, C. Schank, R. Mueller-Reisener, P. Hellmann, A. Link, G. Sparn, W. Assmus, and F. Steglich, Physica B **206-207**, 586 (1995).
- [24] F. Steglich, P. Gegenwart, C. Geibel, R. Helfrich, P. Hellmann, M. Lang, A. Link, R. Modler, G. Sparn, N. Buttgen, and A. S. Loidl, Physica B **223-224**, 1 (1996).
- [25] D. Louca, J. D. Thompson, J. M. Lawrence, R. Movshovich, C. Petrovic, J. L. Sarrao, and G. H. Kwei, Phys. Rev. B **61**, R14940 (2000).
- [26] C. Geibel, to be published.
- [27] H. Wilhelm, T. Luehmann , T. Rus and F. Steglich, Rev. Sci. Instrum. **75**, 2700 (2004).
- [28] G. Bruls, B. Wolf, D. Finsterbusch , P. Thalmeier, I. Kouroudis, W. Sun , W. Assmus, B. Luethi, M. Lang, K. Gloos, F. Steglich, and R. Modler, Phys. Rev. Lett. **72**, 1754 (1994).
- [29] W. Assmus, M. Herrmann, U. Rauchschwalbe, S. Riegel, W. Lieke, H. Spille, S. Horn, G. Weber, F. Steglich, and G. Cordier, Phys. Rev. Lett. **52**, 469 (1984).

- [30] E.A. Goremychkin and R. Osborn, Phys. Rev. B **47**, 14280 (1993).
- [31] P. Gegenwart, C. Langhammer, C. Geibel, R. Helfrich, M. Lang, G. Sparn, F. Steglich, R. Horn, L. Donnevert, A. Link, and W. Assmus, Phys. Rev. Lett. **81**, 1501 (1998).
- [32] O. Stockert, E. Faulhaber, G. Zwicknagl, N. Ster, H. S. Jeevan, M. Deppe, R. Borth, R. Kuechler, M. Loewenhaupt, C. Geibel, and F. Steglich, Phys. Rev. Lett. **92**, 136401 (2004).
- [33] E. Faulhaber, O. Stockert, K. Schmalz, H. S. Jeevan, M. Deppe, C. Geibel, F. Steglich, M. Loewenhaupt, Journal of Magnetism and Magnetic Materials **310**, 295 (2007)
- [34] E. Lengyel, G. Sparn, M. Nicklas, H. S. Jeevan, C. Geibel, F. Steglich, Physica B **378-380**, 415 (2006).
- [35] G. Zwicknagl and U. Pulst, Physica B **186-188**, 895 (1993).
- [36] G. Zwicknagl, Adv. Phys. **41**, 203 (1992).
- [37] O. Stockert, J. Arndt, A. Schneidewind, H. Schneider, H. S. Jeevan, C. Geibel, F. Steglich, M. Loewenhaupt, Physica B **403**, 973 (2008).
- [38] K. Kikoin, private communication.

Chapter 4

Evolution of magnetism and superconductivity in $\text{CeCu}_2(\text{Si}_{1-x}\text{Ge}_x)_2$

4.1 Introduction

CeCu_2Si_2 was the first heavy-fermion superconductor discovered in 1979 [1]. The isostructural compound CeCu_2Ge_2 is a heavy-fermion system (HFS) with a Kondo temperature $T^* = 6$ K showing a magnetically ordered ground state [2]. Below the Néel temperature $T_N = 4.1$ K neutron powder diffraction revealed antiferromagnetic (AFM) order with Kondo-compensated Ce moments [3,4,5]. The magnetic phase transition of CeCu_2Ge_2 is reflected by a jump in the specific heat corresponding to a mean-field transition [2]. The magnetic order in CeCu_2Ge_2 is in accordance with the expected decrease of the hybridization strength between f and conduction electrons upon increasing the volume from CeCu_2Si_2 to CeCu_2Ge_2 which stabilizes the magnetic ordered state. With application of pressure, CeCu_2Ge_2 loses its AFM state and becomes superconducting at an applied pressure of $\simeq 7.0$ GPa [6]. The reduction in volume at that pressure corresponds to the difference in volume between

CeCu₂Si₂ and CeCu₂Ge₂.

Despite nearly 30 years of study, the nature of the unconventional superconducting state in CeCu₂Si₂ as well as its interplay with magnetism is still very far from being understood [12, 13]. One way to gain more insight is to study this system upon tuning the strength of the magnetism, which can easily be done by substituting Si by the larger, but isoelectronic Ge. The investigations on polycrystalline sample were done by Knebel et al. [7] and Trovarelli et al. [8]. Both authors reported an increase of the Néel temperature with increasing Ge content. Furthermore, they found additional phase transitions below T_N . The recent detailed investigations on single crystals by Deppe et al. [9, 15] show results similar to those obtained on polycrystalline samples. Fig. 4.1 shows the magnetic phase diagram as a function of the Ge content x in the region $x < 0.5$ drawn based on the specific heat, thermal expansion, electrical resistivity and neutron diffraction results [9]. It clearly shows a continuous increase of the Néel temperature T_N with x and, in addition, a first order transition at $T_1 < T_N$. For $x > 0.4$ even a third transition appears at $T_L < T_1 < T_N$ [9, 14]. Recently a detailed NMR (Cu-NQR) study of a $\simeq 1$ % Ge-doped polycrystal [10, 11] suggests coexistence of the slowly fluctuating AFM phase with superconducting phase.

Here, we investigate in more detail the low Ge-doped region $0.01 < x < 0.10$. Study of pure CeCu₂Si₂ showed that the main parameter determining the ground state of a given sample is the Cu/Si ratio. Therefore, we investigate here Ge doping for various Si/Cu content. As we discussed for CeCu₂Si₂, superconductivity in CeCu₂Si₂ takes place in the vicinity of the disappearance of the magnetic phase. Accordingly the pressure - temperature phase diagram of CeCu₂Ge₂ shows a superconducting transition at pressure > 7 GPa [6]. However, superconductivity is still observed up

to 10 % Ge doping, where it seems to coexist with magnetism in contrast to the situation in pure CeCu_2Si_2 . We have grown single crystals of $\text{Ce}_y\text{Cu}_2(\text{Si}_{1-x}\text{Ge}_x)_2$, with different compositions varying from $x = 0.02$ and 0.1 , and $y = 1.05, 0.98, 0.95, 0.9$ and 0.8 . The crystal-growth method used is the same as for pure CeCu_2Si_2 , i. e., a modified Bridgman method with Cu as flux. Initially we prepared the polycrystalline samples using arc melting and than add 40 mole % Cu. We, furthermore, used the same temperature profile as for pure CeCu_2Si_2 single crystals. With this procedure we found large single crystals with mass ranging from 1 g to 5 g, and measured the physical properties on these single crystals.

4.2 $\text{CeCu}_2(\text{Si}_{0.98}\text{Ge}_{0.02})_2$

In order to study the evolution of the superconducting phase, we first synthesized samples with 2 % Ge doping. We started the crystal growth with the pre-melted composition of $\text{Ce}_{0.95}\text{Cu}_2(\text{Si}_{0.99}\text{Ge}_{0.02})_2$ and Cu flux. A powder X-ray diffraction measurement confirms the sample to be single phase with the ThCr_2Si_2 structure and the lattice parameters $a = 4.101(4)$ Å and $c = 9.9276(7)$ Å. The lattice constants are very close to those of the undoped samples. EDAX shows that the actual Ge content in a single crystal is approximately 0.8 to 0.85 %. Fig. 4.2 shows the high-temperature electrical resistivity of a $\text{CeCu}_2(\text{Si}_{0.98}\text{Ge}_{0.02})_2$ single crystal measured with current J parallel to the crystallographic a direction. The resistivity shows the same Kondo lattice behavior as observed in pure CeCu_2Si_2 . The two broad maxima in $\rho(T)$ are denoted as T^* and T_{CEF} , the former being related to the onset of coherence among the Kondo ions while the latter one is associated with Kondo scattering of the excited crystal electric field levels. T^* is slightly lower compared to pure CeCu_2Si_2 which

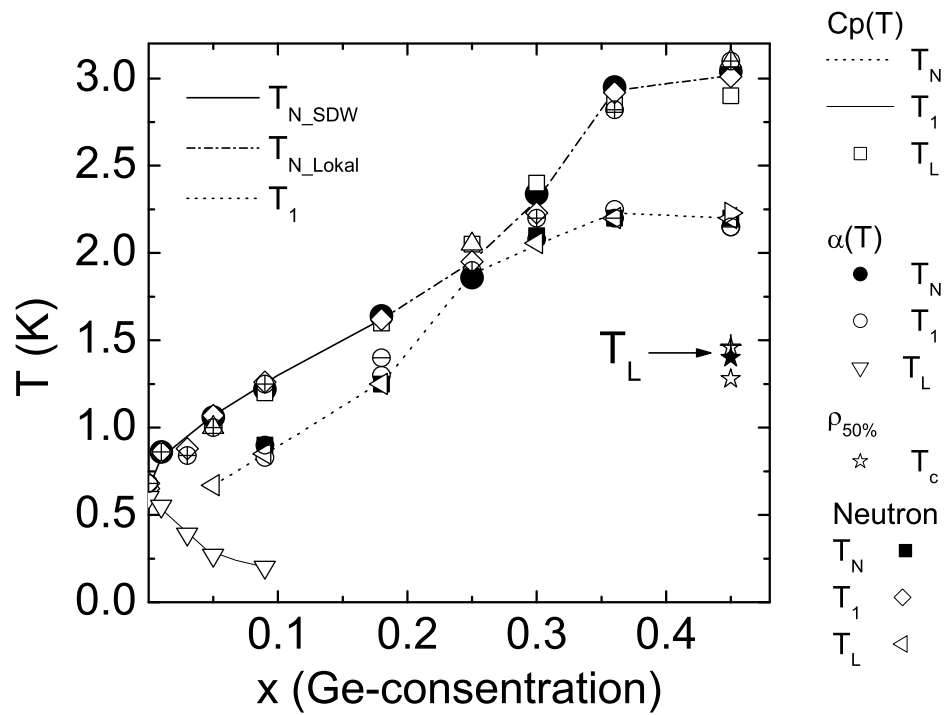


Figure 4.1: Temperature - Ge concentration (x , T) magnetic phase diagram of $\text{CeCu}_2(\text{Si}_{1-x}\text{Ge}_x)_2$. Data points are collected from specific heat, resistivity data, thermal expansion and neutron experiment. T_N increases with increasing Ge substitution, while SC is observed up to 10% Ge in resistivity [9].

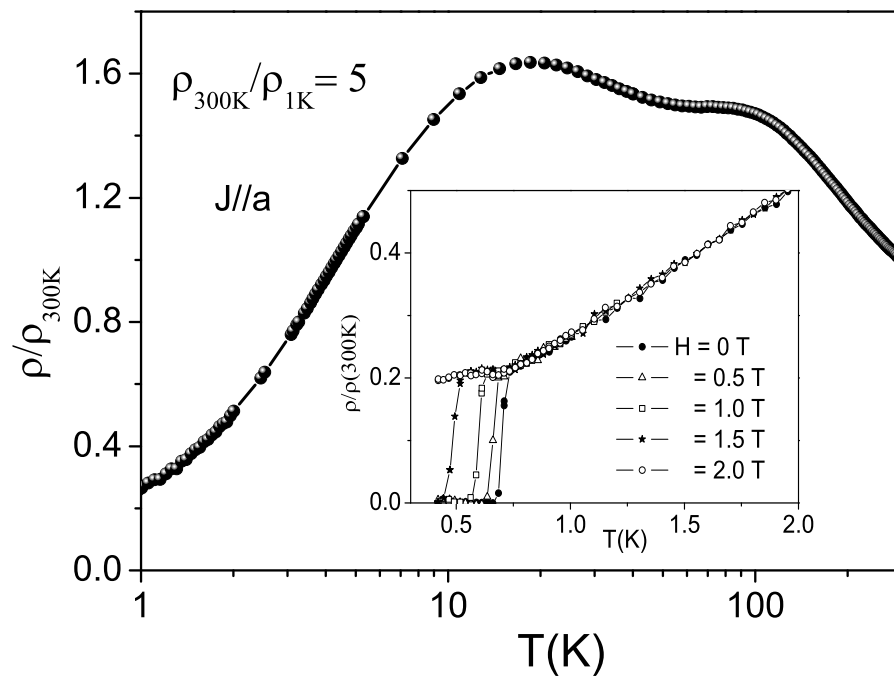


Figure 4.2: The temperature dependence of the electrical resistivity of a $\text{CeCu}_2(\text{Si}_{0.98}\text{Ge}_{0.02})_2$ single crystal measured with current J parallel to the crystallographic a direction. The two broad maxima in $\rho(T)$ are denoted as T^* and T_{CEF} . Inset show low temperature resistivity measured for different magnetic fields.

is possibly due to two effects. Substituting Ge for Si shifts the system towards the magnetic side and, thus, reduces T_K . A second possibility is the disorder effect which can also shift the onset of coherence to lower temperatures. The residual resistivity ratio down to 2 K is 5, which is the same as for the stoichiometric samples. The inset shows the low-temperature resistivity measured for different magnetic fields. In zero magnetic field, $\rho(T)$ shows a sharp drop below 0.7 K, which shifts to lower temperatures with increasing field and disappears (at least above 0.5 K) in an applied magnetic field of 2 T. The small hump (anomaly) at 0.6 K for applied magnetic field of 2 T is possibly due to AFM ordering.

The temperature dependence of the resistivity of $\text{CeCu}_2(\text{Si}_{0.98}\text{Ge}_{0.02})_2$ in the temperature range $0.8 \text{ K} < T < 4 \text{ K}$ is shown in Fig. 4.3. As in pure CeCu_2Si_2 it is clear that the resistivity does not follow a T^2 -law as would be expected for a conventional Fermi-liquid system. It can be best fitted in the temperature range 0.9 K to 3.5 K with $\rho = \rho_0 + AT^n$, where $\rho_0 = 1.16 \mu\Omega\text{cm}$, $n = 1$ and $A = 7.3 \mu\Omega\text{cm}/\text{K}^2$. Such a NFL resistivity is often observed near a quantum critical point induced by a zero-temperature antiferromagnetic phase transition.

The low-temperature specific heat of the $\text{CeCu}_2(\text{Si}_{0.98}\text{Ge}_{0.02})_2$ single crystal in zero field and at 2 T is displayed in Fig. 4.4 as C/T versus T . The data proves that the system undergoes two subsequent phase transitions, a magnetic AFM one at $T_N = 0.7 \text{ K}$, which is not affected by a magnetic field of 2 T, and a transition to a superconducting state at $T_c = 0.5\text{K}$, which suppressed by $B = 2 \text{ T}$. The sharp anomaly at T_c is, on the one hand, a first indication for a first order transition from the SC to the AFM state. On the other hand the large jump height of more than 1.2 J/mol K^2 shows the good quality of the single crystal. In the applied field of 2 T, which is

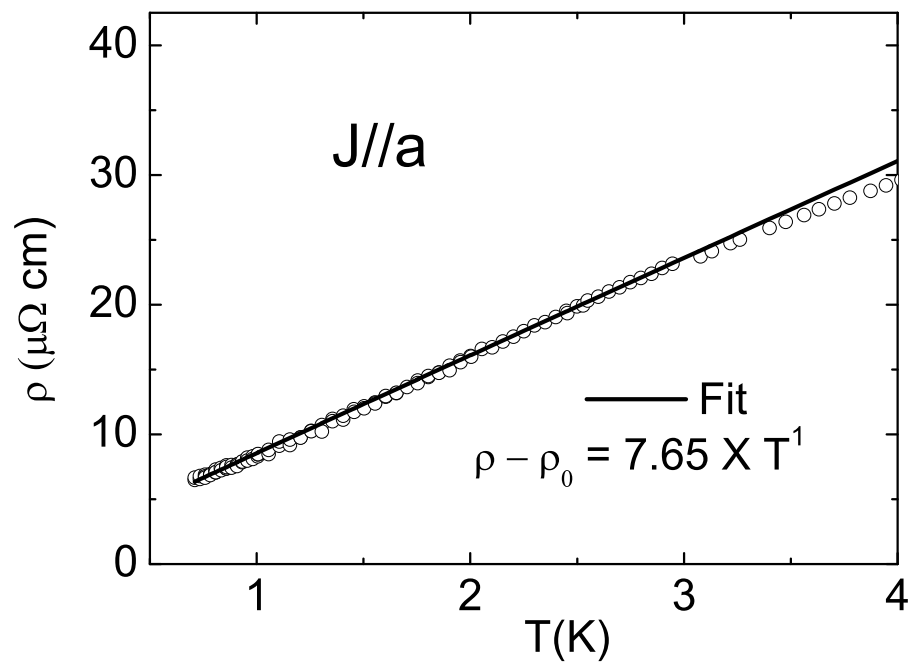


Figure 4.3: Low-temperature electrical resistivity of a $\text{CeCu}_2(\text{Si}_{0.98}\text{Ge}_{0.02})_2$ single crystal for $0.8 \text{ K} < T < 4 \text{ K}$, and current J along the a axis. Solid line shows the $\rho = \rho_0 + AT^n$ fit with $\rho_0 = 1.16 \mu\Omega$, $A = 7.65 \mu\Omega \text{ cm} / \text{K}$ and $n = 1.0$.

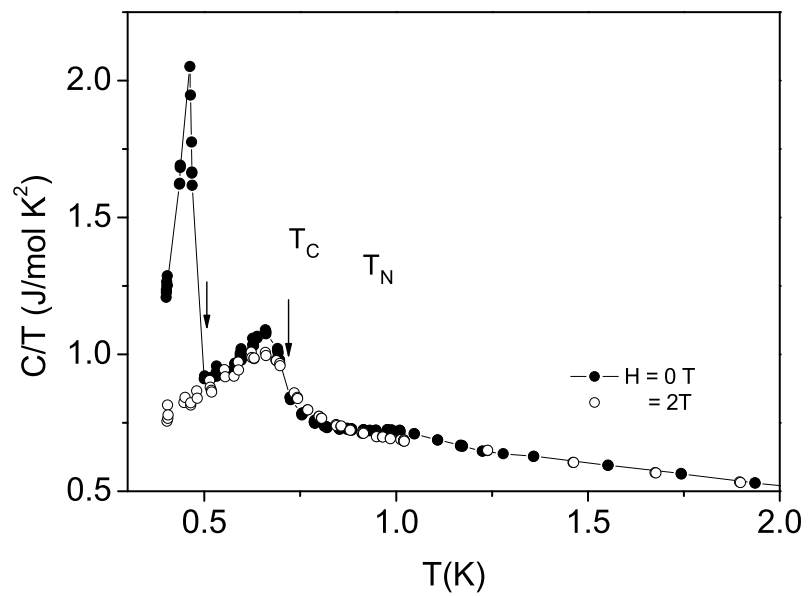


Figure 4.4: Temperature dependence of the specific heat of a $\text{CeCu}_2(\text{Si}_{0.98}\text{Ge}_{0.02})_2$ single crystal. Arrows show anomalies corresponding to magnetic ordering (T_N) and superconducting order (T_c), measured in zero and 2 T magnetic field.

above the upper critical field the data show a small hump which likely corresponds to the AFM phase transition. In order to investigate the coexistence or competition of SC and AFM phase, we performed elastic neutron scattering measurements. More details on these experiments shall be described in the PhD thesis of J. Arndt [16]. According to preliminary, non-published results of G. Bruls [22], and C. Geibel [23], one expects a transition from competing SC and AFM to coexisting SC and AFM phases upon stabilization of the magnetic state.

Fig. 4.5 shows the temperature dependence of the integrated magnetic intensity (a.u) measured at the propagation vector $q = (0.21 \ 0.21 \ 0.55)$ on $\text{CeCu}_2(\text{Si}_{0.98}\text{Ge}_{0.02})_2$ single crystal in different applied magnetic field. The lower part of Fig. 3.5 shows the ac-susceptibility measured simultaneously to detect the SC phase. In zero field the integrated magnetic intensity increases with decreasing temperature below T_N but reaches a maximum when the system starts to become superconducting. Below T_c the Bragg peak intensity decreases with further decreasing temperature and becomes almost negligible below 300 mK. The reduction of the magnetic intensity with decreasing temperature in the superconducting regime in $\text{CeCu}_2(\text{Si}_{0.98}\text{Ge}_{0.02})_2$ indicates that the superconducting phase grows at the expenses of the magnetic phase. The SC phase transition is confirmed by the sharp drop in ac-susceptibility as shown in the lower part of Fig. 4.5. Upon applying a magnetic field of 0.5 K the SC phase transition shifts to lower temperature, while the magnetic phase develops at expenses of the SC phase. When the SC phase is suppressed by a field of 2 T (no signal in ac-susceptibility), the Bragg peak intensity increases continuously down to the lowest investigated temperature of 80 mK. This emphasizes the competition between the SC and the AFM state. Thus, the 2 % Ge-doped single crystal presents the same

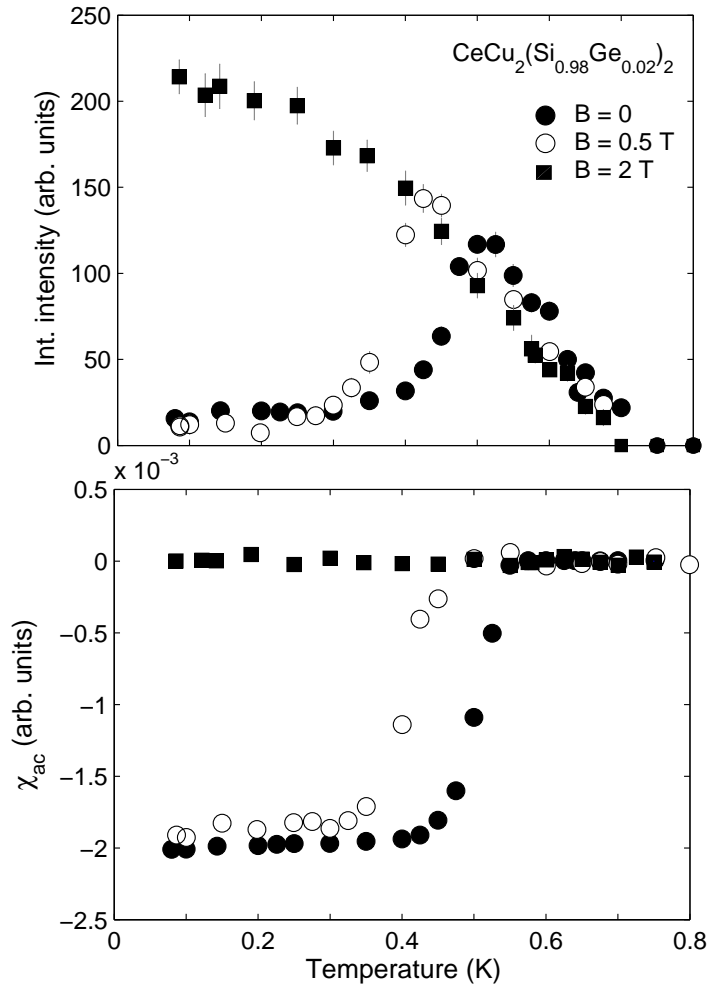


Figure 4.5: Upper part shows the temperature dependence of the integrated magnetic intensity (a.u) at the propagation vector $q = (0.21 \ 0.21 \ 0.55)$ in a $\text{CeCu}_2(\text{Si}_{0.98}\text{Ge}_{0.02})_2$ single crystal for different applied magnetic fields. Lower part shows the ac-susceptibility measured simultaneously.

behavior as the stoichiometric CeCu_2Si_2 single crystals. Likely, one needs a higher Ge content to enter the regime of coexistence of SC and AFM phase. We therefore investigated the behavior at a much higher doping of 10 % Ge

4.3 $\text{Ce}_y\text{Cu}_2(\text{Si}_{0.9}\text{Ge}_{0.1})_2$

The neutron scattering experiments on the 2 % Ge-doped $\text{CeCu}_2(\text{Si}_{1-x}\text{Ge}_x)_2$ crystal confirmed the competition of the long-range magnetic order and the SC phase. In order to extend the studies, we prepared $\text{CeCu}_2(\text{Si}_{0.9}\text{Ge}_{0.1})_2$ single crystals. As explained earlier, the magnetic phase will be significantly stabilized at that Ge concentration. Since experiments on polycrystals showed the SC phase to be very sensitive to the Cu/Si ratio at 10 % doping, we also varied the Cu to Si/Ge content by tuning the initial Ce content as explained in an earlier chapter. $\text{Ce}_y\text{Cu}_2(\text{Si}_{0.9}\text{Ge}_{0.1})_2$ samples with compositions $y = 0.8, 0.9, 0.98$ and 1.05 were prepared using arc melting of pure elements in appropriate compositions. The same flux growth technique is used as of pure and 2 % Ge-doped single crystal. We obtained large single crystals with mass ranging from 1 g to 5 g. On these single crystals we measured the transport and thermodynamic properties.

In previous investigations of polycrystalline $\text{CeCu}_2(\text{Si}_{1-x}\text{Ge}_x)_2$ samples, it was established that the Si/Ge ratio mainly influences the unit cell volume, while the Cu/(Si+Ge) ratio mainly affects the c/a ratio [9, 19]. We, therefore, plot in Fig. 4.6 the unit cell volume V and the c/a ratio as a function of the initial Ce content. The unit cell volume scatters around $V = 167.9 \pm 0.1 \text{ \AA}^3$, which according to a calibration based on the polycrystals corresponds to a Ge doping level of $8.4 \pm 1.2 \%$. The microprobe analysis also reveals a Ge doping level of 8 % to 9 %, thus, in excellent agreement with the value determined from the lattice parameters. This slight reduction of the real Ge content compared to the initial melt composition is in good agreement with the observations by M. Deppe [9], who in his extended work on the crystal growth of $\text{CeCu}_2(\text{Si}_{1-x}\text{Ge}_x)_2$ already noticed a reduction by 10%.

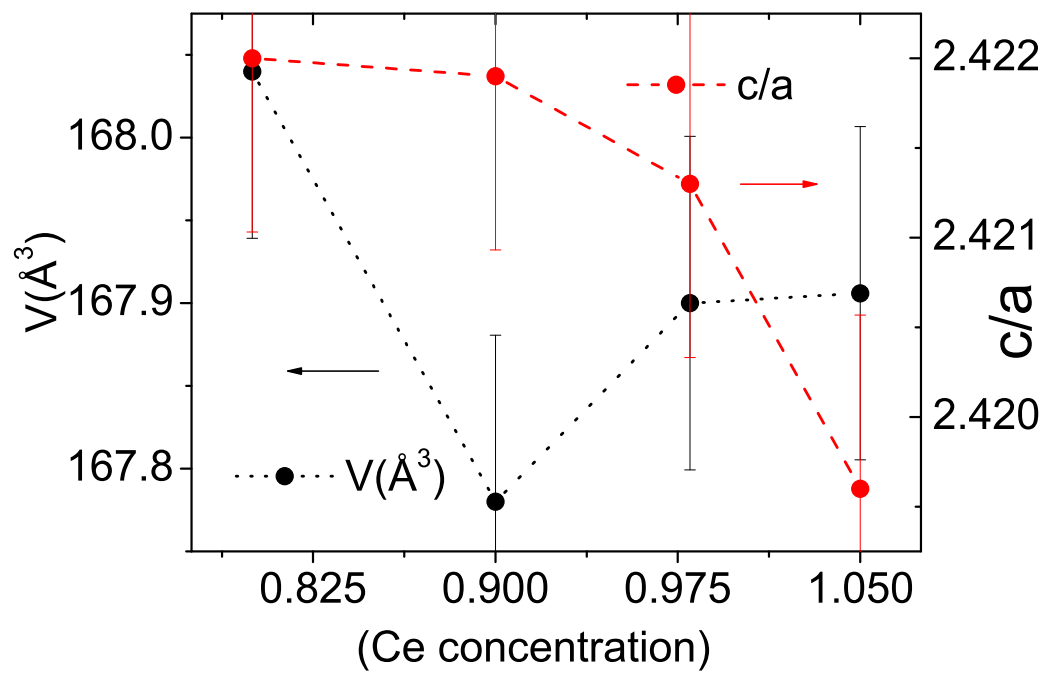


Figure 4.6: Unit-cell volume and c/a ratio as a function of the initial Ce concentration in the initial melt. Lines are guide to the eye.

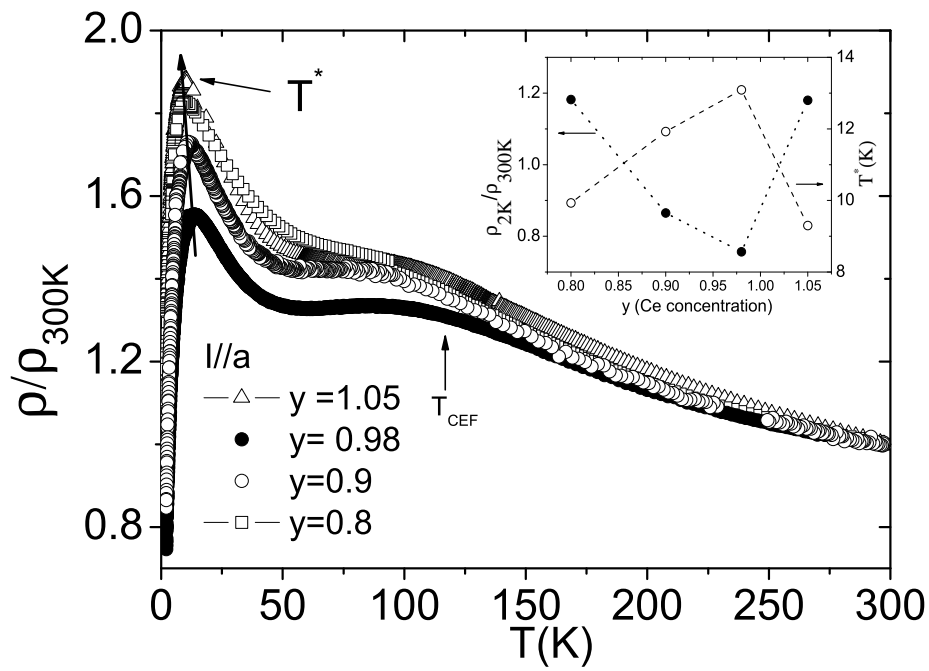


Figure 4.7: The temperature dependence of the electrical resistivity for different initial Ce content $y = 0.8, 0.9, 0.98$ and 1.05 . The current was applied along the a direction. Two maxima are observed at T_{CEF} and T^* in all the samples. The broad maximum at T_{CEF} approximately remains in same position whereas the low-temperature maximum at T^* shifts to different positions with changing y . Inset shows the resistivity ratio at 2 K and 300 K, ρ_{2K}/ρ_{300K} and T^* as a function of y .

In contrast to the unit cell volume, the c/a ratio presents a clear dependence on y , with a pronounced drop for $y > 0.9$. A comparison with the results obtained on off-stoichiometric polycrystalline samples indicates a nearly stoichiometric or slightly Si/Ge - rich 122 phase for $y = 0.80$, and a 2 % excess Cu in the $y = 1.05$ single crystals. The clear decrease of the c/a ratio with increasing y proves that an increasing Ce content in the flux results in an increase of the Cu content in the single crystals. Unfortunately, the change in the Cu content of the present single crystals was too small to be directly detected in the microscopic measurement.

The room-temperature normalized resistivity $\rho/\rho_{300\text{K}}$ for the different initial Ce concentration $y = 0.8, 0.9, 0.98$ and 1.05 is shown in Fig. 4.7. The resistivity was measured with current J parallel to a . The overall temperature dependence of the resistivity for all different initial compositions is the same as for pure CeCu_2Si_2 . As already explained in the previous chapter, the maximum at T_{CEF} near 100 K corresponds to the Kondo scattering of excited CEF levels, while the maximum at lower temperature marked with T^* reflects the onset of coherent scattering. Compared to pure CeCu_2Si_2 the former one does not show appreciable changes, while the latter one is now much more pronounced and shifted towards lower temperatures. The most pronounced changes between different initial Ce content y are the maximum values of $\rho(T^*)/\rho_{300\text{K}}$ at $\rho(T^*)$ and the residual resistivity $\text{RR2K} = \rho_{2\text{K}}/\rho_{300\text{K}}$, both being closely related. Furthermore, one can also notice a shift of T^* with the initial composition y . Therefore, we plot in the inset of Fig. 4.7 T^* and RR2K as a function of y . RR2K presents a clear minimum for $y = 0.98$ and increases for larger as well as smaller y . This suggests that the single crystal grown from the melt $y = 0.98$ are close to a stoichiometric $(\text{Si}+\text{Ge})/\text{Cu}$ ratio. It is noted that T^* presents a y dependence

which is just the opposite of $\text{RR } 2K(y)$ with the largest value for $y = 0.98$ whereas the maximum in ρ is also more pronounced and smaller values for larger or smaller y . This fact indicates that in the present system T^* is mainly determined by disorder, not by change of the Kondo scale T_K . This is confirmed by specific heat measurements which indicate the change in T_K to be much weaker than those in T^* .

Upper part of Fig. 4.8 shows the specific heat as a function of temperature for different compositions y in zero magnetic field. C/T shown in Fig. 4.8 corresponds to the electronic contribution since the phonon contribution is negligible in this temperature range. The AFM transition is observed at $T_N = 1.32$ K for $y = 0.98$, which is consistent with the previous report of M. Deppe [9]. Increasing the initial Ce content to $y = 1.05$, which is expected to result in an increasing of Cu/(Si+ Ge) ratio in the single crystal, leads to a significant shift of T_N towards lower temperatures, and to a reduction of the size of the anomaly at T_N . By contrast, decreasing y results initially in a slight increase of T_N and a slight sharpening of the transition. The results for $y = 0.8$ are very close to those for $y = 0.98$. Thus, as for pure CeCu_2Si_2 , a higher Cu content weakens the AFM state quite significantly, while a lower Cu content has no strong effect. In order to find out whether these changes can be related to a variation of the Kondo scale we compiled the entropy $S(T)$ by integrating the measured $C(T)/T$. For the region below 0.5 K which is the limit of the experiment, the measured C/T data above 0.5 K were linearly extrapolated to $T = 0$. The resulting $S(T)$ is shown in the lower part of Fig. 4.8. The difference between the four compositions are quite small, however, it is not really larger than the accuracy of the experimental data. All curves reach $0.5R\ln 2$ (the $S(T)$ value expected for $T = T_K/2$) near $T = 5$ K showing that there is no large difference in T_K , T_K being close to 10 K (close to the

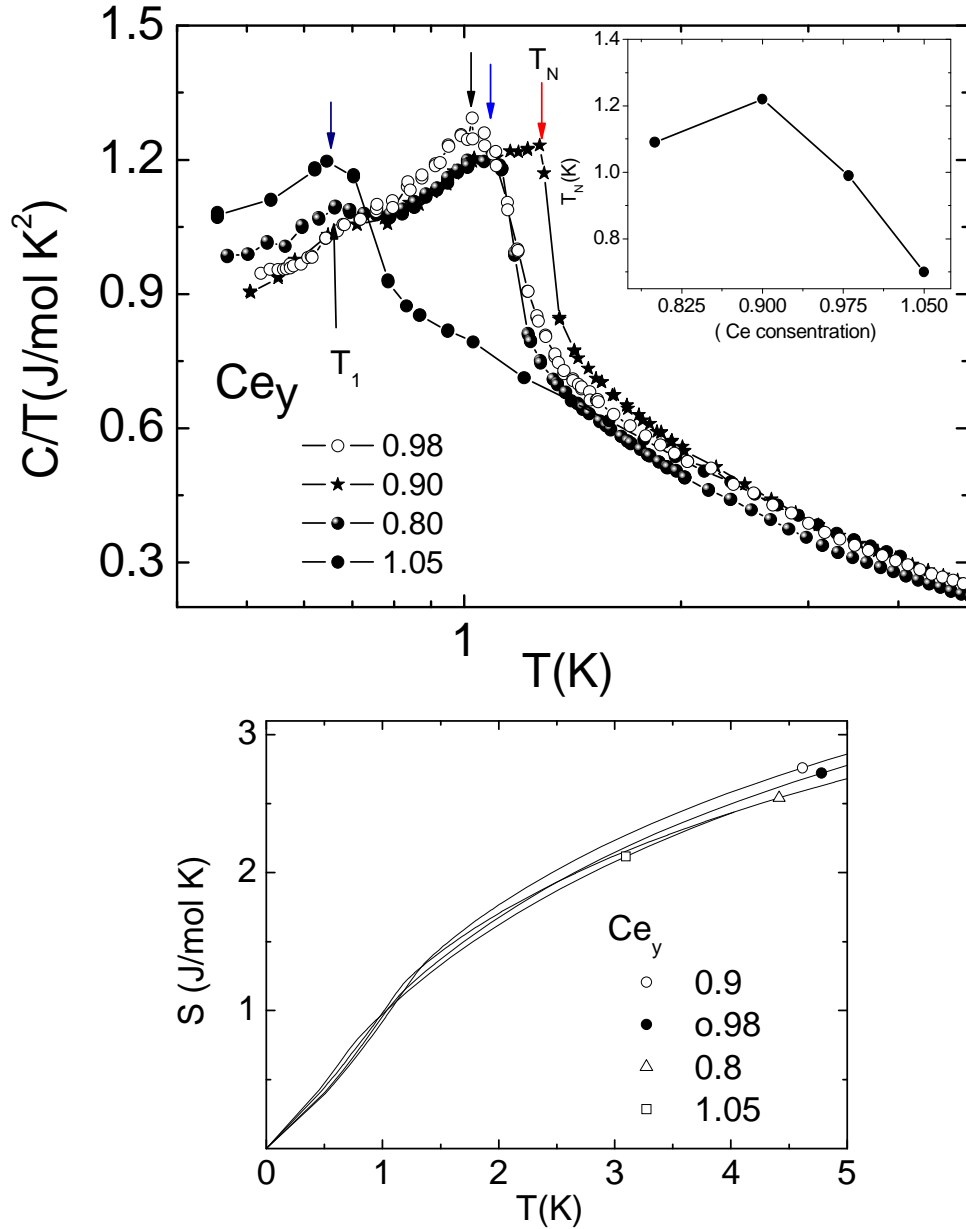


Figure 4.8: Upper part shows the temperature dependence of the specific heat for different initial Ce composition $y = 0.8, 0.9, 0.98$ and 1.05 . Arrows show anomalies corresponding to the magnetic ordering T_N . Inset shows the variation of T_N with respect to the y concentrations. Lower plot corresponds to the entropy versus temperature for four compositions. The total entropy was calculated by extrapolating the specific heat to $T = 0$.

value for pure CeCu_2Si_2) for all single crystals. There is a tendency in favor of an increase of the entropy and thus a slight decrease of T_K with increasing y . However, the difference is obviously much smaller than those observed for T^* , proving that changes in T^* is mostly determined by disorder. These results of the specific heat measurements suggest that the magnetic ordering is also more sensitive to the kind of disorder (Cu on Si site or Si on Cu site) than on T_K .

In order to look at the superconductivity in this system we measured the low-temperature resistivity. Fig. 4.9 shows the electrical resistivity in the temperature range 50 mK to 1 K for different y values. The current was applied along a random direction. All curves show a pronounced, superconducting-like drop in $\rho(T)$, near 0.45 K for $y \leq 0.9$ but shifts down to $\simeq 0.2$ K for $y = 0.8$. This latter single crystal presents a further weak and smooth decrease of $\rho(T)$ below 0.8 K, which corresponds to a lock-in transition of the propagation vector [20, 21]. In the $y = 0.8$ single crystal, we could resolve a hysteresis in the ρ measurement between heating and cooling curve, see inset of the Fig. 4.9. This is a further confirmation for the first order nature of this transition. The sharpest SC transition is observed for $y = 1.05$, while decreasing y leads to a broadening of the transition, besides the shift to lower T . This suggests the SC state to be more robust for large y value, i.e., Cu excess. This correlation is the same as that observed in pure CeCu_2Si_2 . In lower part of Fig. 4.9 we plot the ratio of ρ just above T_c to ρ at 300 K, ρ_{LT}/ρ_{300K} , as well as the midpoint of the SC transition in ρ as a function of y . While T_c clearly correlates with y , it does not correlate with the resistivity. This is in contrast to the behavior expected for unconventional SC and observed in many heavy-fermion SC, but in analogy to the behavior observed for pure CeCu_2Si_2 .

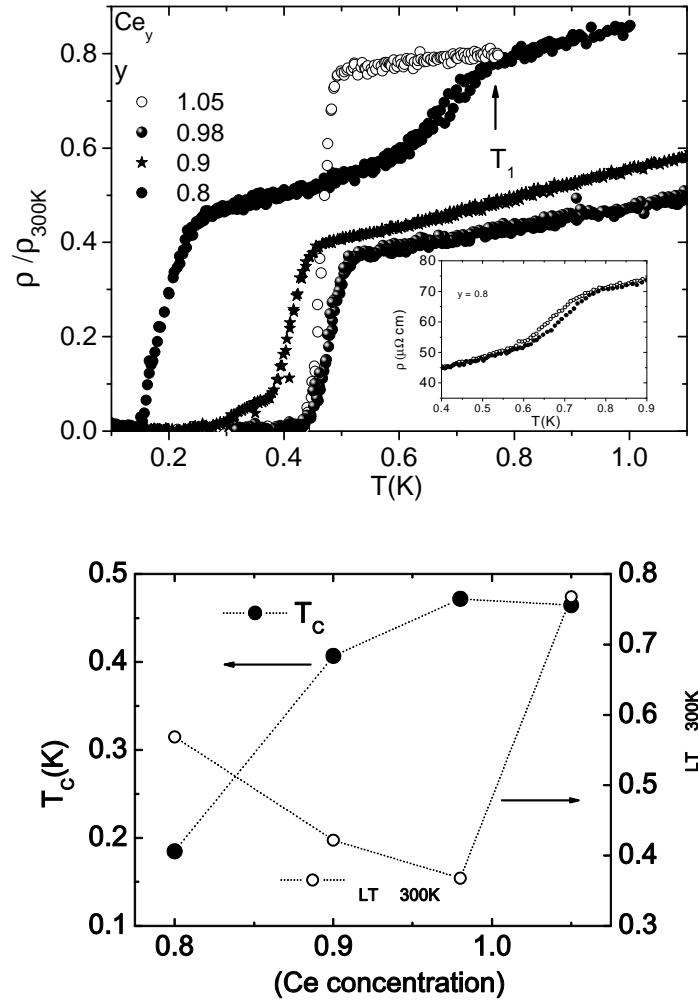


Figure 4.9: Upper part shows the low-temperature electrical resistivity in the temperature range 50 mK to 1 K for different values of y , 0.8, 0.9, 0.98 and 1.05, the current was applied in random direction. All the samples show the superconducting transition. The sample with $y = 0.8$ shows a clear magnetic transition T_1 at 0.8 K. Inset shows the hysteresis observed at T_1 in resistivity for the sample with $y = 0.8$. Lower part: Open circles correspond to 50 % T_c and closed circles correspond to inverse of residual resistivity ratio (ρ_{LT}/ρ_{300K}) for different y concentration.

In order to check the bulk nature of the SC phase in these samples we studied the low-temperature specific heat (measurements performed by T. Cichorek). The low-temperature specific heat was measured using the quasiadiabatic heat-pulse method. More details can be found elsewhere [18]. Here we chose two single crystals, one with a good RRR and another with a large and sharp superconducting transition in $\rho(T)$. Fig. 4.10 shows the low-temperature specific heat divided by temperature measured for $y = 1.05$ and 0.9 in the temperature range 100 mK to 2 K. The first obvious result is the absence of any clear anomaly related to the superconducting transition near 0.4 K. Thus, the superconductivity observed in $\rho(T)$ at T_c is not a bulk property. A careful analysis of the data below 0.2 K suggests that in the $y = 1.05$ sample a small anomaly is hidden in the upward tail corresponding to a much lower T_c . However, it was not possible to determine independently the nuclear contribution which lead to this tail. Therefore, a confirmation for the presence of bulk SC at low temperature in this single crystal is lacking. However, a recent specific heat measurement on a large $y = 0.9$ single crystal revealed a small, but clear anomaly at $T_c = 0.15$ K and χ_{ac} measurements showed a pronounced diamagnetic signal below this temperature. Thus, in this large $y = 0.9$ single crystal bulk SC at $T = 0.15$ K was demonstrated. Neutron scattering experiments on the same crystal did not reveal a decrease of the magnetic Bragg peak intensity below 0.15 K, indicating the coexistence of SC and AFM in this single crystal [16]. By contrast, the anomalies related to the magnetic transitions are large and clearly seen. Thus, the data above 0.5 K are in good agreement with those previously obtained with the PPMS (see Fig. 4.8). This indicates a good homogeneity of the single crystal concerning the magnetic properties, since the present data were obtained on a large part of the single crystal

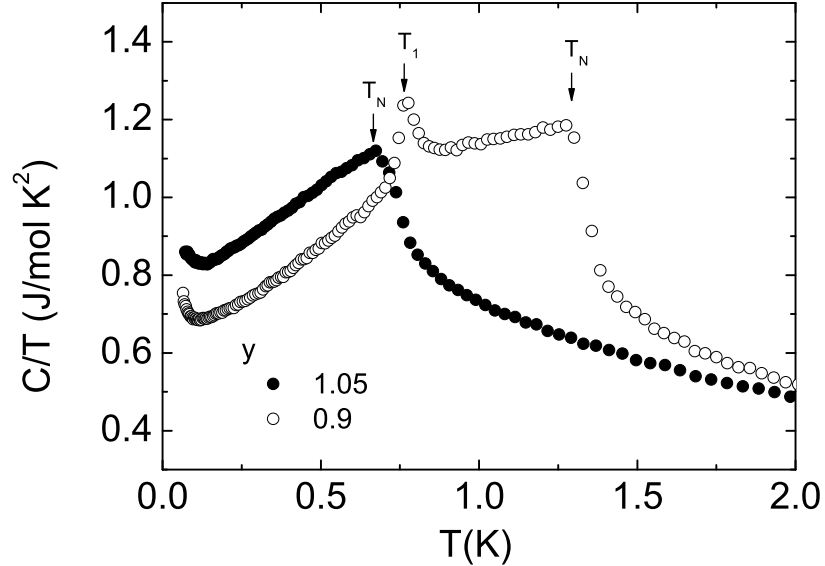


Figure 4.10: Temperature dependence of the heat capacity divided by temperature at $B = 0$ for $y = 1.05$ and 0.9 . We observed two phase transitions T_1 and T_N for $y = 0.9$ and one transition for $y = 1.05$.

(1 g), while the PPMS data were obtained on a small part ($< 4\text{mg}$). The $y = 1.05$ single crystal presents only one transition at $T_N = 1.3$ K. The much larger anomaly at T_N in the present measurement compared to the PPMS data can be related to the different measurement techniques, quasi-adiabatic versus relaxation method, and the first order type transition at T_1 , for which a relaxation techniques is not appropriate.

4.4 Discussion and Conclusions

Previous investigations of the alloy system $\text{CeCu}_2(\text{Si}_{1-x}\text{Ge}_x)_2$ [5, 8, 9] clearly show that substituting Ge for Si stabilizes the antiferromagnetic state. Many of these

results suggest an evolution from a SDW-type ordering of heavy quasiparticles at low Ge content to a classical AFM order of local moments for a Ge doping level larger than 20 %. The aim of the present work was to study the evolution of the superconducting state upon increasing Ge- content. For this purpose we have grown $\text{CeCu}_2(\text{Si}_{1-x}\text{Ge}_x)_2$ single crystals with $x = 0.02$ and $x = 0.10$ and investigated their magnetic and SC properties by means of resistivity, magnetic susceptibility, specific heat and neutron scattering measurements.

The $x = 0.02$ single crystal showed almost the same properties as a stoichiometric, undoped CeCu_2Si_2 single crystal of A/S type: the temperature T^* of the Kondo maximum in $\rho(T)$, the resistivity ratio at low temperature, the anomaly in $C(T)$ at the AFM transition at $T_N = 0.7$ K, followed by a large peak at the onset of superconductivity at $T_c = 0.5$ K. All these properties look very similar to those observed for pure CeCu_2Si_2 A/S type single crystals. Accordingly, the neutron scattering experiments reveal a competition between the SC and the AFM phase, the former one expelling the latter one below T_c . Thus our results are in clear disagreement with a recent report by Kitaoka et. al [17] based on NMR results which observed the coexistence of SC and AFM on a microscopic scale in a polycrystalline sample with 1 %Ge. We suspect that this disagreement is the result of different level of disorder and slight differences in composition.

For 10 % Ge doping, we have grown a series of single crystals with different initial Ce content y in the flux, because the effect of deviation from stoichiometric (i.e. $\text{Cu}/[\text{Si}+\text{Ge}]$) on the superconductivity was not yet known. Analysis of lattice parameters and measurements confirmed a Ge doping level of $\simeq 8.5$ at. %, slightly lower than the initial level in the flux as expected from previous studies on the flux

growth of the alloy. The small but clear decrease of the c/a ratio with increasing y indicates an increase of the $\text{Cu}/(\text{Si}+\text{Ge})$ ratio with increasing y . A comparison with the polycrystalline data suggest that single crystals with small y are nearly stoichiometric while the $y = 1.05$ single crystal has a Cu excess of $\simeq 2\%$. The results of the $\rho(T)$ measurements reveal a strong dependence of the temperature T^* of the low- T maximum (Kondo coherence peak), of the magnitude of this maxima, and of RRR on the y content. A large value of T^* correlates with a small magnitude of resistivity at 2 K and a large RRR. Largest RRR and T^* are observed for $y = 0.98$, while smaller and larger y lead to a significant decrease of T^* . This suggest that the $y = 0.98$ single crystal is close to stoichiometry, while the $y = 0.8$ and the $y = 1.05$ single crystals have significant amounts of defects. Furthermore it indicates that the change in T^* is related to disorder and not to a change in the Kondo temperature T_K . We observed a clear dependence of the AFM transition on y . Small y , i.e., nearly stoichiometric single crystals presents a sharp transition at a comparatively high temperature $T_N \simeq 1.25$ K, while the excess Cu in the $y = 1.05$ single crystal results in a broader transition and a shift to lower temperatures, $T_N \simeq 0.7$ K. Thus, Cu excess leads to a weakening of the AFM state as for undoped CeCu_2Si_2 . However, an analysis of the entropy did not reveal a significant change towards larger T_K in single crystals with Cu excess.

All the samples show at low temperatures a pronounced drop in resistivity to $\rho(T) = 0$ indicating superconductivity with T_c in the range $0.2 \text{ K} < T_c < 0.5 \text{ K}$. The $y = 1.05$ single crystal presents a very sharp transition at a comparatively high $T_c \simeq 0.45$ K, while the $y = 0.8$ single crystal exhibits a much broader transition at lower $T_c \simeq 0.2$ K. Thus, the resistivity data would suggest SC to be more stable when

the AFM state is weaker, similar to the situation in undoped CeCu_2Si_2 . However, no anomaly was observed in $C(T)$ at the respective transitions, indicating that this superconductivity is not a bulk property. The low-temperature $C(T)$ measurements performed on small $y = 1.05$ and $y = 0.9$ single crystal reveal only in the former one a weak indication for a SC state at a much lower $T_c < 0.15$ K. However, a recent study of a large (1.9 g) $y = 0.9$ single crystal evidenced a small but clear anomaly in $C(T)$ at $T_c = 0.15$ K, associated with a pronounced diamagnetic signal in χ_{ac} , proving bulk SC in this crystal. Neutron scattering experiments performed on same single crystal did not show a weakening of the AFM state below T_c , pointing to the coexistence of SC and AFM state [16].

In summary, we have grown $\text{CeCu}_2(\text{Si}_{1-x}\text{Ge}_x)_2$ single crystals with $x = 0.02$ and $x = 0.10$ to study the evolution of the superconducting state upon stabilizing the AFM state by Ge doping. The 2 % Ge-doped single crystal showed competing SC state with $T_c = 0.5$ K and AFM state with $T_N = 0.7$ K, the former one expelling the latter one below T_c , as in pure, undoped CeCu_2Si_2 single crystal of A/S type. By contrast, bulk SC was up to now only observed in one of the several 10 % Ge-doped single crystal, and their neutron scattering experiments indicate that SC and AFM state coexist. Thus, the present study gives a further confirmation of a transition from competing to coexistence SC and AFM upon stabilizing of the AFM state. However, the SC state in 10 % Ge-doped CeCu_2Si_2 seems to be even more sensitive to stoichiometry and defects than in undoped CeCu_2Si_2 , and the present studies leave many question still open, but gives some ideas for improvement. Thus, further studies both on the growth and of the physical properties of 5 % to 10 % Ge-doped single crystals are necessary to get a deeper insight into the regime where SC and AFM state coexists.

Bibliography

- [1] F. Steglich, J. Aarts, C. D. Bredl, W. Lieke, D. Meschede, W. Franz and H. Schäfer, Phys. Rev. Lett. **43**, 1982 (1979).
- [2] F. de Boer, J. C. P. Klaasse, P. A. Veenhuizen, A. Bohm, C. D. Bredl, U Gottwick, H. M. Mayer, L. Pawlak, U. Rauchschwalbe, H. Spille and F. Steglich. J. Mag. and Mag. Mat. **63** (1987).
- [3] A. Loidl, A. Krimmel, K. Knorr, G. Sparn, M. Lang, C. Geibel, S. Horn, A. Grauel, F. Steglich, B. Welslau, N. Grewe, H. Nakotte, F. R. de Boer and A.P. Murani, Ann. Phys. (Germany) **1**, 78 (1992).
- [4] A. Krimmel, A. Loidl, H. Schober, and P. C. Canfield. Phys. Rev. B **55**, 6416 (1997).
- [7] A. Krimmel and A. Loidl, Physica **234 & 236**, 877 (1997).
- [6] D. Jaccard, K. Behnia and J. Sierro. Physica B **206-207**, 279 (1995).
- [5] G. Knebel, C. Eggert, D. Engelmann, R. Viana, A. Krimmel, M. Dressel, and A. Loidl. Phys. Rev. B **53**, 11586 (1996).

- [8] O. Trovarelli, M. Weiden and R. Mueller-Reisener, M.Gomez-Berisso, P. Gegenwart, M. Deppe, C. Geibel, J. G. Sereni, and F. Steglich, Phys. Rev. B **56**, 678 (1997).
- [9] M. Deppe, Phd Thesis, Technische Universität Dresden.
- [10] Y. Kawasaki, K. Ishida, S. Kawasaki, T Mito, G. Q. Zheng, Y. Kitaoka, C. Geibel and F. Steglich, J. Phys. Soc. Jpn. **73**,194 (2004).
- [11] Y. Kawasaki, K. Ishida, K. Obinata, K. Tabuchi, K. Kashima, Y. Kitaoka, O. Trovarelli, C. Geibel and F. Steglich, Phys. Rev. B **66**, 224502 (2002)
- [12] R. Feyerherm, A. Amato, C. Geibel, F. N. Gygax, P. Hellmann, R. H. Heffner, D. E. MacLaughlin, R. Mueller-Reisener, G. J. Nieuwenhuys, A. Schenck and F. Steglich Phys. Rev. B **56**, 699 (1997).
- [13] K. Ishida, Y. Kawasaki, K. Tabuchi, K. Kashima, Y. Kitaoka, K. Asayama, C. Geibel and F. Steglich, Phys. Rev. Lett. **82**, 5353 (1999).
- [14] O. Stockert, M. Deppe, E. Faulhaber, H. S. Jeevan, R. Schneider, N. Stue Xer, C. Geibel, M. Loewenhaupt, F. Steglich. Physica B **359**, 349 (2005).
- [15] N. Oeschler, M. Deppe, E. Lengyel, R. Borth, P. Gegenwart, G. Sparn, C. Geibel, and F. Steglich, Phys. Rev. B **71**, 094409 (2005).
- [16] J. Arndt, O. Stockert, R. Borth, E. Faulhaber, K. Schmalzl, A. Schneidewind, H. S. Jeevan, C Geibel, M. Loewenhaupt, F. Steglich, J. Phys.: Conference Series **150**, 042008 (2009).

- [17] Y. Kitaoka, K. Ishida, Y. Kawasaki, O. Trovarelli, C. Geibel and F. Steglich, J. Phys.: Condens. Matter **13**, L79 (2001).
- [18] H. Wilhelm, T. Luehmann, T. Rus and F. Steglich, Rev. Sci. Instrum. **75** 2700 (2004).
- [19] K. Heuser, Diploma thesis, Technische Universität Darmstadt (1996), unpublished.
- [20] O. Stockert, M. Deppe, E. Faulhaber, H. S. Jeevan, R. Schneider, N. Stuesser, C. Geibel, M. Loewenhaupt and F. Steglich, Physica B **359** , 349 (2005).
- [21] O. Stockert, E. Faulhaber, G. Zwicknagl, N. Ster, H. S. Jeevan, M. Deppe, R. Borth, R. Kehler, M. Loewenhaupt, C. Geibel, and F. Steglich, Phys. Rev. Lett. **92**, 136401 (2004).
- [22] G. Bruls, private communication.
- [23] C. Geibel, private communication.

Chapter 5

Magnetic and Quadrupolar ordering in YbRu_2Ge_2

5.1 Introduction

The spin and orbital degrees of freedom of 4f electrons in rare-earth compounds allow for further type of ordering beside the standard one, i.e. that of the magnetic dipole moment. Higher-order moment ordering like quadrupolar, octupolar has been observed and studied in a number of systems. Recently, these higher order moments have received considerable attention. In rare-earth intermetallic compounds the interaction between the higher order moments also occurs through conduction electrons by an indirect exchange mechanism, as the Ruderman-Kittel-Kasuya-Yosida (RKKY) interaction. Similar to dipole ordering there exist ferro or antiferroquadrupolar ordering depending on the quadrupolar interaction. However, in most of the systems dipole ordering is dominating. Furthermore, the occurrence of quadrupolar order implies the presence of quadrupolar degrees of freedom which puts some constraints on

the crystal field scheme, and further reduces the number of appropriate compounds. Thus, most examples of quadrupolar order were observed in Pr- and Tm-based compounds, because the even number of f-electrons in these elements results quite often in non-magnetic doublets as crystal electric field (CEF) ground states, which provide a basis for the occurrence of quadrupolar ordering. Examples for systems with quadrupolar ordering are PrPb₃ [1] and the RB₂C₂ [3, 2] (R = rare earth). In many cases one first observes quadrupolar ordering and then at lower temperature dipolar ordering. Thus, the tetragonal compound TmAu₂ [4, 5], which is discussed later, shows the ferroquadrupolar ordering at $T_0 = 7$ K and AF magnetic order at $T_N = 3.2$ K.

For elements with an odd number of f-electron, like Ce and Yb, non-cubic environment of the f-element splits the J multiplets into Kramers doublets, which carry a dipole but no quadrupole moment. For these elements, quadrupolar ordering is usually restricted to cubic systems, where under appropriate circumstances the CEF ground state can be a quartet which carries a quadrupolar moment. For Ce the prototype is CeB₆ [6, 7], which has been extensively studied since many years. By contrast, for Yb no example for quadrupolar ordering has yet been well established for intermetallic Yb systems. YbSb was proposed to be a antiferroquadrupolar ordering (AFQ) at 5 K, where a very strong exchange leads to a mixing of excited and ground-state CEF doublet [8]. But the parameter required for such a mixing are rather extreme and the ordering is very far from being conclusive. Very recently, YbAl₃C₃ [9] was proposed to show quadrupolar ordering at an extremely high ordering temperature $T_Q = 80$ K. Later on, it was shown that it is a structural distortion, which is not related to 4f-electrons [10]. Thus, a clear example for quadrupolar ordering in

an Yb compound is still lacking.

In intermetallic compounds based on Ce or Yb, the instability of the f -shell allows them to be tuned from a magnetic to a non-magnetic state by changing the chemical composition or by applying pressure. At the crossover from the non-magnetic to the magnetic state, one observes unusual properties like the formation of heavy fermions, the onset of unconventional superconductivity, or strong deviations from the Fermi-Liquid behavior usually expected in a metal. A large part of the research in this field was performed on CeT_2X_2 compounds (T = transition metals, X = Si and Ge) crystallizing in the ThCr_2Si_2 or a related structure type. Two prominent examples are CeRu_2Si_2 [11, 12] and CeRh_2Si_2 [13], the former one is just on the non-magnetic side and shows an unconventional metamagnetic transition from a delocalized to a localized f -state, while the later one, although being just on the magnetic side of the crossover, has the highest antiferromagnetic ordering temperature among all Ce compounds. While all the CeT_2X_2 compounds have now been thoroughly investigated, much less studies were performed on the Yb-based homologous compounds. For the Yb compounds with $\text{T} = \text{Ru}, \text{Os}, \text{Rh}, \text{Ir}$, only little or nothing is known about their physical properties. Recently, YbRh_2Si_2 [14, 15] was found to be located extremely close to the quantum critical point (QCP) connected with the onset of a magnetic ordered state with $T_N = 70$ mK, which leads to very interesting properties and makes this compound one of the most fascinating in the field of quantum phase transitions. This transition at T_N can be suppressed either by small doping of Ge, La or Lu or by a small applied magnetic field $B = 0.06$ T. However, tuning to the QCP by chemical doping or by applying a magnetic field might inhibit the appearance of unconventional superconductivity. The appropriate approach for the observation of

a QCP at $B = 0$ in a clean Yb-system is to start with a pure Yb compound located on the paramagnetic side of the QCP and to apply pressure. Since for Yb applying pressure for the magnetic configuration because of its smaller atomic volume. An example for such a systems is YbIr_2Si_2 , which was recently investigated in our group [16]. It is a heavy fermion system just on the non-magnetic side of the critical point, exhibiting Landau Fermi-liquid state below 0.2 K. By application of external pressure > 3 GPa, YbIr_2Si_2 first shows non Fermi-liquid behavior and at even higher pressure evidence for magnetic order, but no sign of superconductivity despite a very low residual resistivity $\rho_0 < 1\mu\Omega\text{cm}$. In search for further interesting Yb-based compounds we synthesized YbRu_2Ge_2 and investigated its physical properties. To the best of our knowledge only structural data have been reported previously [17]. Our results revealed a stable trivalent Yb state, rather complex ordering phenomena with three successive transitions at $T_0 = 10.2$ K, $T_1 = 6.5$ K and $T_2 = 5.7$ K, and, to our surprise, a quasiquartet crystal field ground state which is a unique situation among YbT_2X_2 compounds. The behavior observed at T_0 suggests this transition to be quadrupolar in nature. The combination of a quasiquartet CEF ground state, a high Yb ordering temperature and the likely relevance of quadrupolar interactions makes YbRu_2Ge_2 a unique system among Yb-based compounds. In order to check further the microscopic nature of these phases we performed neutron diffraction and μSR (Muon Spin Rotation, Relaxation and Resonance) experiments. These measurements confirm the magnetic ordering at 6.5 K and show no dipolar order at 10 K [18].

5.2 Sample preparation

The preparation of YbRu_2Ge_2 turned out to be difficult. First attempts by heating a stoichiometric amount of Yb, Ru and Ge in sealed tungsten crucible up to 1450 °C leads to the formation of other phases like monoclinic $\text{Yb}_2\text{Ru}_3\text{Ge}_4$ [23], cubic $\text{Yb}_4\text{Ru}_7\text{Ge}_6$ [20]. Annealing the melted ingots did not lead to a significant improvement. A first success was reached by using a solid state sintering method. A stoichiometric (2 % excess of Yb) amount of the three elements (99.99 % pure) is sealed inside a tantalum crucible using arc welding. The sealed Ta crucible is annealed at 1200 °C for four days in Ar atmosphere. After cooling to room temperature, the sample is ground into powder and pressed into pellets. The same annealing treatment is repeated for 6 more days with the pellets. X-ray powder diffraction and electron probe microanalysis confirm the formation of polycrystalline YbRu_2Ge_2 with lattice parameter $a = 4.2105 (10) \text{ \AA}$ and $c = 9.7567 (20) \text{ \AA}$. Some of low intensity peaks are unindexed which correspond to an impurity phase which is less than 2 % of the main phase, possibly due to Yb-oxide (Yb_2O_3) phase.

High quality single crystals of YbRu_2Ge_2 were obtained using a flux method. 97.5 mole % of In flux and 2.5 mole% of a stoichiometric amount of Yb, Ru and Ge elements were put together in a Alumina crucible. The Alumina crucible was heated in argon atmosphere in a vertical furnace to 1450 °C within 5 hrs, kept at this temperature for 1 hr, and then slowly cooled down with 5 °C/hr to 1200 °C. More details on the crystal growth is explained in the crystal growth chapter. Electron probe microanalysis and X-ray powder diffraction pattern of further single crystals showed that some of the single crystals were single phase YbRu_2Ge_2 , while others had few impurity phases of less than 5 % at the surfaces. The lattice parameters of

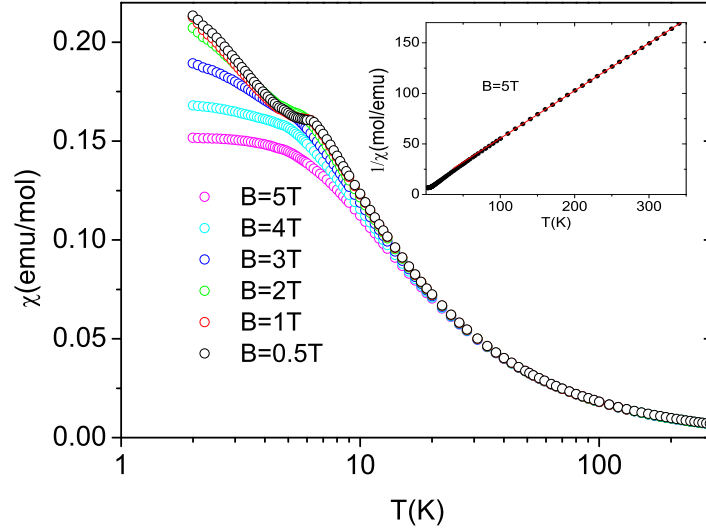


Figure 5.1: Temperature dependence of the magnetic susceptibility of a polycrystalline YbRu_2Ge_2 sample for different magnetic fields. Inset: Inverse magnetic susceptibility in an applied field of 5 T.

our single crystals, $a = 4.2116 (10) \text{ \AA}$ and $c = 9.7549(20) \text{ \AA}$ were slightly different from those obtained for our polycrystals, $a = 4.2105 (10) \text{ \AA}$ and $c = 9.7567 (20) \text{ \AA}$, but differed significantly from those reported in the literature, $a = 4.203 (4) \text{ \AA}$ and $c = 9.763 (9) \text{ \AA}$ [17]. This suggests the existence either of a significant homogeneity range (likely along the Ge-Ru line) or of Ge-Ru disorder, changes in composition or disordering leading to a decrease of the lattice parameter a and a much weaker increase of c .

5.3 Physical properties

5.3.1 Magnetic susceptibility of YbRu_2Ge_2

First we shortly report the results of the magnetic susceptibility measurements on a polycrystalline YbRu_2Ge_2 sample. Fig. 5.1 shows the variation of the magnetic susceptibility with temperature. The measurements were performed in the temperature range from 2 K to 300 K for different applied magnetic fields.

As the temperature decreases, the magnetic susceptibility increases indicating strong paramagnetic behavior. Accordingly, $1/\chi$ follows a Curie-Weiss law as shown in the inset of Fig. 5.1. A fit (solid line) of the high temperature data above 50 K to the Curie-Weiss law $1/\chi = C/(T - \theta_P)$ gives an effective moment $\mu_{\text{eff}} = 4.13 \mu_B$ which is close to the value $4.54 \mu_B$ for free trivalent Yb^{3+} moments. The Weiss temperature is estimated to $\theta_P = -18$ K, indicating dominant antiferromagnetic interaction at low temperatures. At approximately 6 K there is an anomaly which almost disappears at higher field suggesting AFM order at 6 K. The magnetic susceptibility increases further below the transition in low fields which is likely due to some paramagnetic defects. Thus, these preliminary results indicate that Yb is in 3+ state and orders magnetically below 6 K.

Because of strong crystal electric field effects, rare-earth based magnetic systems usually present a strong anisotropy of the magnetic properties. Therefore a precise investigation of these properties requires a single crystal. Fortunately, the YbRu_2Ge_2 single crystal obtained from the flux growth was just large enough for the measurements of the susceptibility and the magnetization along the main directions. For the tetragonal structure one expects the strongest anisotropy between the c- axis and the

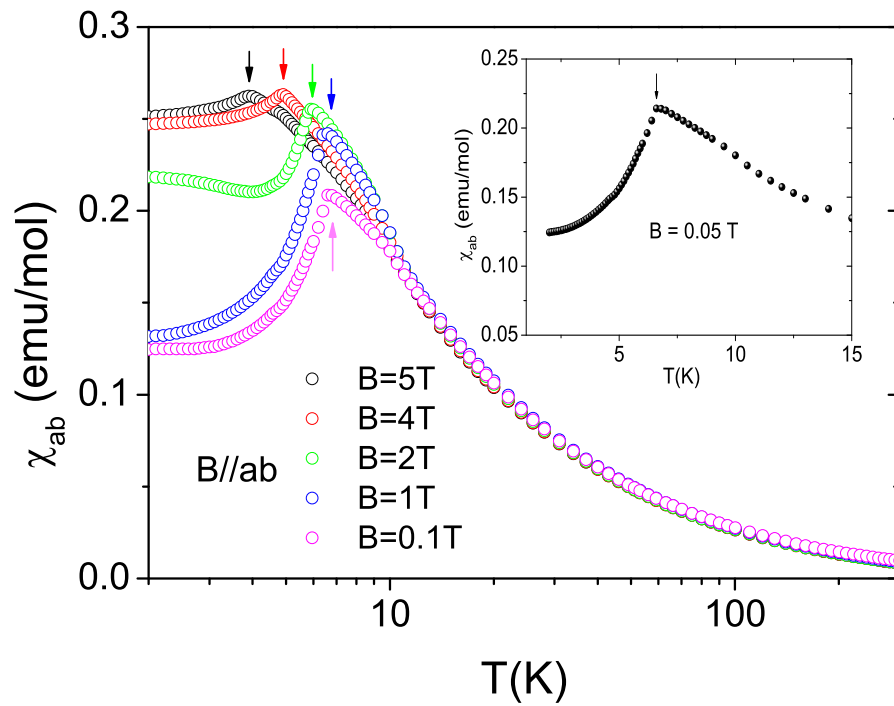


Figure 5.2: Temperature dependence of the magnetic susceptibility of YbRu₂Ge₂ for magnetic fields $B = 1$ T, 2 T and 5 T applied along the basal plane. Inset: Low-temperature part.

basal plane, while in the basal plane, no anisotropy is expected at low field in the paramagnetic state. Therefore we first address and compare the temperature dependence of the magnetic susceptibility for different magnetic fields applied along the basal plane (Fig. 5.2) and along the c direction (Fig. 5.3). The anisotropy within the basal plane in the ordered phase shall be addressed later.

The magnetic susceptibility is strongly anisotropic, being much larger for fields along the basal plane (Fig. 5.2) than for fields along the c axis (Fig. 5.3), which indicates that the basal plane is the easy plane and c is the hard direction. For the easy plane, a pronounced drop of $\chi_{ab}(T)$ at $T_1 = 6.5$ K at small magnetic field evidence a transition to a magnetically ordered state, while no anomaly is visible above or below 6.5 K (Inset of Fig. 5.2). However, there is a small change of slope at 10 K which will be more pronounced in magnetic susceptibility along hard direction. The 6.5 K anomaly marked by an arrow shifts to low temperatures upon increasing the magnetic field, as expected for an antiferromagnetic transition. The magnetic susceptibility at 2 K amounts to 0.14 emu/mole for an applied field below 1 T, but increases strongly around $B = 2$ T, suggesting the presence of a metamagnetic transition.

For fields along the hard axis (Fig. 5.3), χ_c is one order of magnitude lower than the susceptibility along the basal plane (Fig. 5.2) at low temperatures. This indicates that in YbRu_2Ge_2 the Yb-magnetic moment is mainly confined in the basal plane. At low temperatures (inset Fig. 5.3), $\chi_c(T)$ shows a significant change of slope at $T_0 = 10.5$ K, followed by a very pronounced decrease below T_1 which was also observed in χ_{ab} . The magnetic field dependence of both the 6.5 K and the 10 K anomalies is very weak, as expected for field applied along a hard direction. Also the susceptibility at 2 K remains the same with increasing magnetic field, in contrast

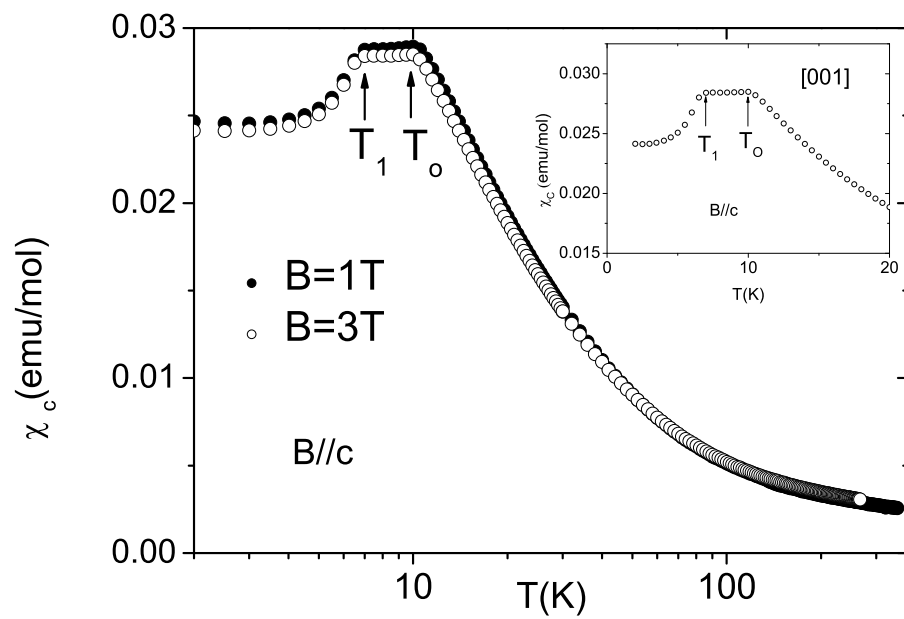


Figure 5.3: Temperature dependence of the magnetic susceptibility of YbRu_2Ge_2 for magnetic fields $B = 1\text{ T}$ and 3 T applied along c axis. Inset: Low-temperature part.

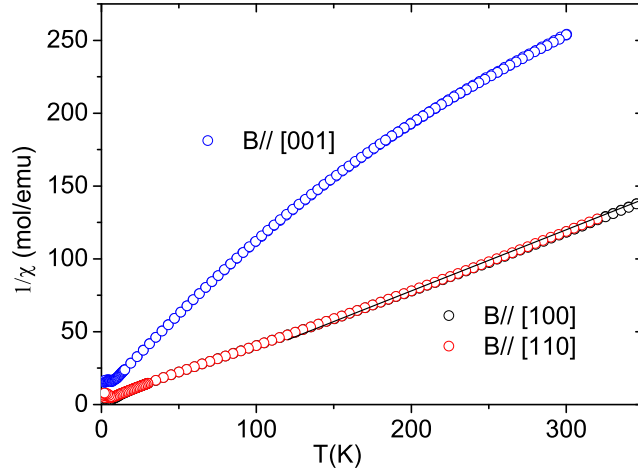


Figure 5.4: Temperature dependence of the reciprocal magnetic susceptibility of YbRu_2Ge_2 measured along [100], [110] and [001].

to the field dependence in the basal plane. Thus, χ_c gives the first clear indication for a phase transition at $T_0 = 10$ K which, as discussed later, is likely of quadrupolar order.

The temperature dependence of the reciprocal magnetic susceptibility of YbRu_2Ge_2 for fields along [100], [110] and [001] is shown in Fig. 5.4. For fields along the basal plane, $1/\chi_{[100]}$ and $1/\chi_{[110]}$ follow rather well a Curie-Weiss law from 150 K up to room temperature. The slight curvature in the $1/\chi_{ab}(T)$ versus T plot around 200 K can be attributed to crystal field effects. The value of the effective moment extracted from the slope between 150 and 300 K is $4.5 \mu_B$, very close to the value expected for a trivalent Yb state ($4.54 \mu_B$). At high temperatures, the reciprocal magnetic susceptibility is isotropic along [100] and [110] as expected, while the anisotropy between [100] and [001] is relatively strong. Furthermore, the $1/\chi_c(T)$ versus T curve shows a

pronounced negative curvature. As a result the slope at 300 K is still slightly smaller (20 %) than that expected for a free Yb^{3+} state. Such a pronounced curvature in $1/\chi(T)$ for fields along the hard axis can be attributed to a rather large overall crystal field splitting. In the related compounds YbIr_2Si_2 [21] and YbRh_2Si_2 [22], the highest excited CEF level is indeed above 400 K. The curvature in $1/\chi_{ab}$ and $1/\chi_c$ makes it difficult to give exact values for the Weiss parameter, θ_W . For fields within the basal plane θ_W is close to zero, while for fields parallel to c , θ_W is larger than 150 K. This difference is related to CEF effects and demonstrates the huge anisotropy of this compound.

Below 15 K, we observe an increasing anisotropy within the basal plane. Fig. 5.5 shows $\chi(T)$ below 20 K for different magnetic fields applied along [100] and [110]. While $\chi_{[001]}$ presents a clear anomaly at $T_0 = 10$ K, no anomaly is visible for fields along [110]. However, a difference develops between $\chi_{[100]}$ and $\chi_{[110]}$ below approximately 12 K at $B = 1$ T, and reaches a maximum at $T_1 = 6.5$ K where the susceptibility along [100] is 30 % greater than along [110] direction. The temperature at which this difference opens increases with increasing the field, while the maximum value of this difference does not change significantly. Such an anisotropy suggests that below 10 K, YbRu_2Ge_2 has no more tetragonal symmetry but a lower one like e.g orthorhombic. A basal plane anisotropy in a tetragonal system at low field is commonly observed in the magnetically ordered state, because the ordering reduces the symmetry of the lattice. Our results for YbRu_2Ge_2 are very similar to those reported for the tetragonal system TmAu_2 , where a ferroquadrupolar ordering at T_0 leads to a comparable anisotropic behavior within the basal plane. Thus, these results support the occurrence of a quadrupolar ordering at 10 K in YbRu_2Ge_2 .

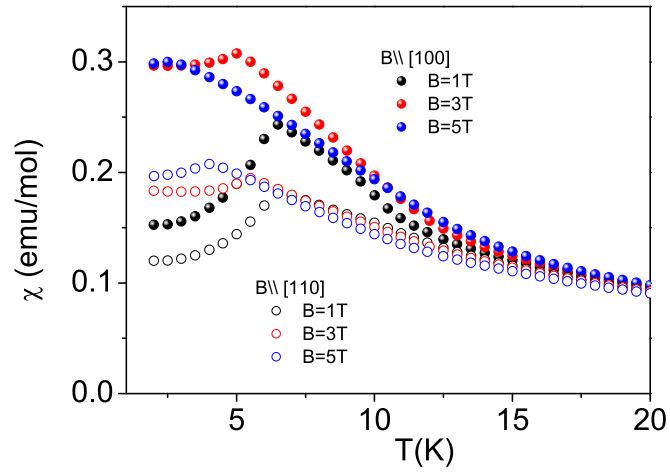


Figure 5.5: Anisotropy between susceptibility along [100] and [110] at low temperatures in different applied field.

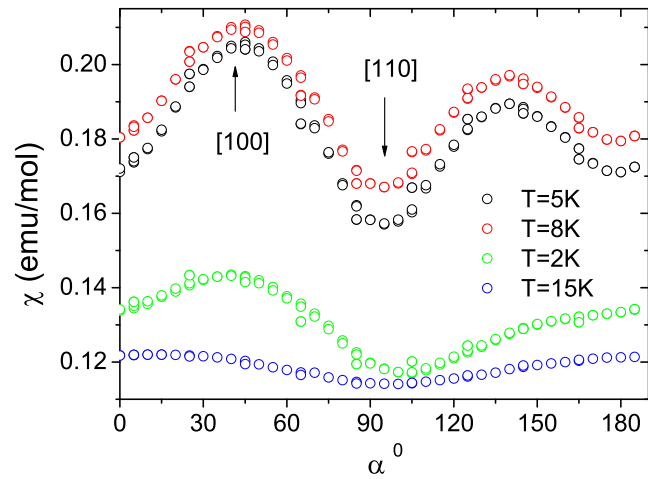


Figure 5.6: Angular dependence of the susceptibility for field rotated within the basal plane, measured at different temperatures $T = 2$ K, 5 K, 8 K and 15 K.

This basal-plane anisotropy is consistent with the angular dependence of the magnetic susceptibility in the basal plane at different temperatures (Fig. 5.6). The magnetization was measured as a function of the orientation of the magnetic field ($B = 1$ T) in the basal plane. The sample was rotated around its c axis perpendicular to the field. Fig. 5.6 shows the angular dependence of the magnetic susceptibility at different temperatures, i. e., in the paramagnetic region (15 K), the quadrupolar phase (8 K), and in the magnetically ordered state (5 K and 2 K). The angular dependence of the magnetic susceptibility has roughly a fourfold symmetry with a maximum along [100] and a minimum along [110] at all investigated temperatures. The difference, however, is very large at $T = 5$ K and $T = 10$ K but very weak at $T = 15$ K. The deviation from the fourfold symmetry can be attributed to off-centering during rotation of the sample and an anisotropy of the very large background of the sample holder.

We completed our investigation by measurements of the magnetization for fields along the main directions. Fig. 5.7 shows the magnetization at 2 K, 4 K and 8 K in fields up to 5 T, applied along the [100] direction. At 2 K, a sharp, field-induced metamagnetic transition is observed at $B = 1.6$ T. The magnetization shows a sharp jump of $0.25 \mu_B/\text{Yb}$. The transition shifts slightly to higher fields at 4 K and disappears at 8 K. Along the [110] direction (Fig. 5.8) a broad transition at a slightly higher critical field is observed. We could not resolve any hysteresis, neither along [100] nor [110]. The magnetization at 4 K and in applied field of 5 T reaches $2 \mu_B/\text{Yb}$ for the [110] and $2.6 \mu_B/\text{Yb}$ for the [100] direction, respectively. Fig. 5.9 shows the magnetization for fields along the c axis at two different temperatures 2 K and 8 K. No metamagnetic transition is visible and the magnetization at 5

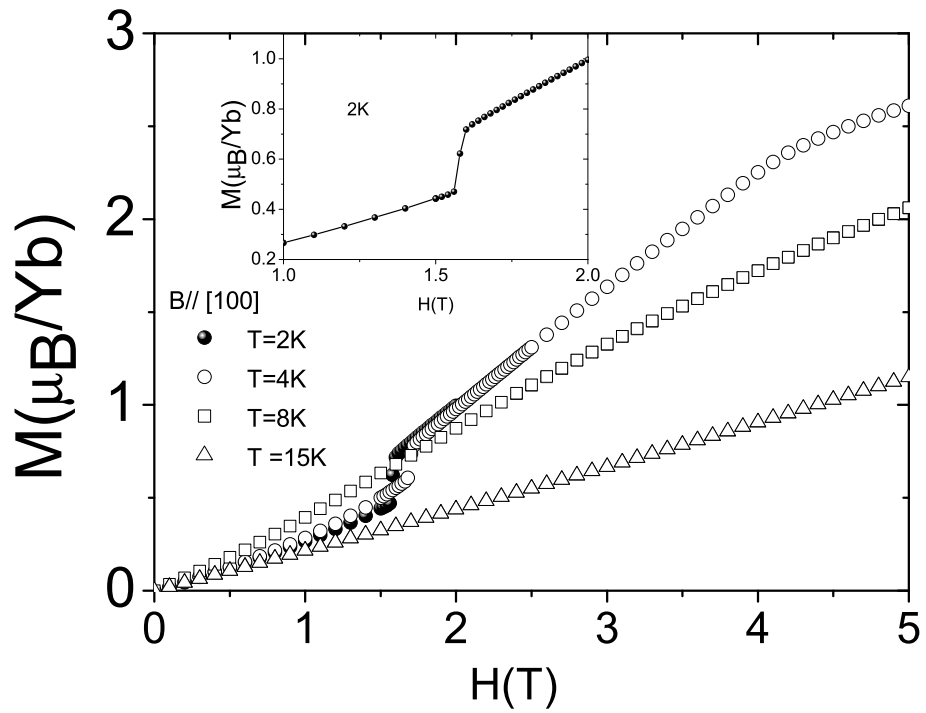


Figure 5.7: Magnetization M versus B plot of YbRu_2Ge_2 at different temperatures for magnetic field applied along $[100]$. Inset shows a closer view of the metamagnetic transition.

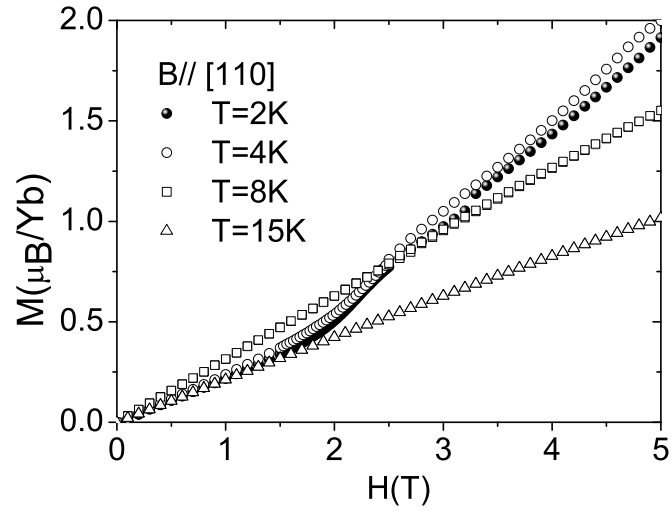


Figure 5.8: Magnetization M versus B plot of YbRu_2Ge_2 at different temperatures for magnetic applied field along $[110]$.

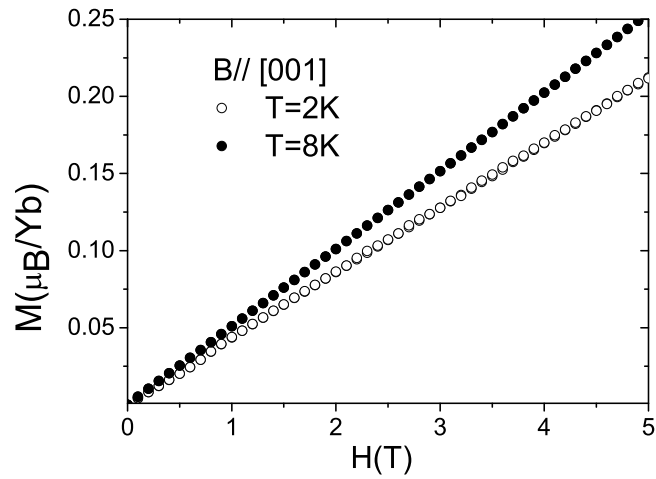


Figure 5.9: Magnetization M versus B plot of YbRu_2Ge_2 at $T = 2\text{ K}$ and 8 K for magnetic field applied along the $[001]$ direction.

T is only $0.25 \mu_B/\text{Yb}$, which is expected for the behavior along the hard axis. It should be pointed out that such a field-induced transition is quite common in the magnetization process in quadrupolar ordered systems. For example in TmAu_2 [4, 5] and RB_2C_2 ($\text{R} = \text{rare earth}$) [3, 2] multiple steps were observed in the magnetization curve. This is due to strong quadrupole - dipole interaction. An applied magnetic field can influence the quadrupolar moment and hence the magnetic structure. On the other hand, metamagnetic transitions are also quite common in other magnetic rare-earth systems, but, there, the step in $M(B)$ is usually a large fraction of the saturation moment. In YbRu_2Ge_2 , the step is one order of magnitude smaller than the saturation moment. We therefore, suspect that this is related to the quadrupolar ordering at T_0 .

5.3.2 Specific heat of YbRu_2Ge_2

The specific heat measurements on the polycrystalline sample of YbRu_2Ge_2 already reveal the basic features in the magnetic behavior. The data shown in the Fig. 5.10 as a plot of C/T versus T evidence a weak transition at $\simeq 10$ K, and a much larger one at $\simeq 6.5$ K in agreement with the anomalies observed in the susceptibility measurements. However, a sharp peak in C/T at $\simeq 5.5$ K indicates a further transition, not yet observed in the susceptibility data. Furthermore, the curve displayed in the inset of Fig. 5.10 immediately suggests that the magnetic entropy exceeds the value $R\ln 2$ expected for a Kramers CEF doublet. Indeed, an integration of C/T reveals the gain of entropy between 2 K to 12 K to amount to about 10 J/mol K, almost twice the value of $R\ln 2 \simeq 5.7$ J/mol K (inset of Fig. 5.10). This excess of entropy cannot be attributed to phonons. Their contribution is still small even at 12 K, since C/T is

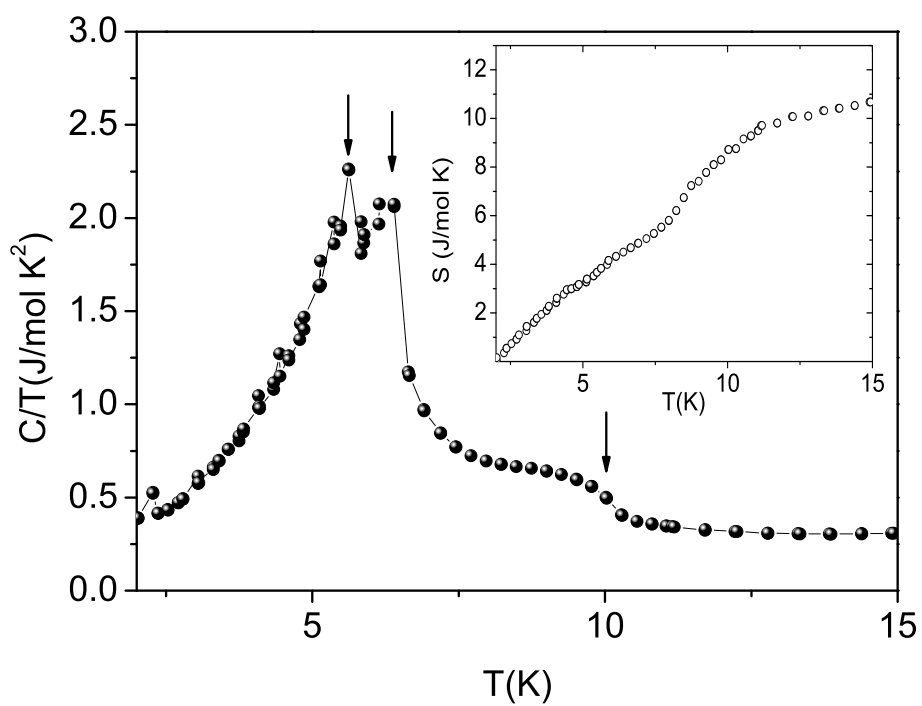


Figure 5.10: The temperature dependence of the heat capacity of polycrystalline YbRu_2Ge_2 in a plot C/T versus T shows the three transitions. The inset shows the increase of the entropy with temperature.

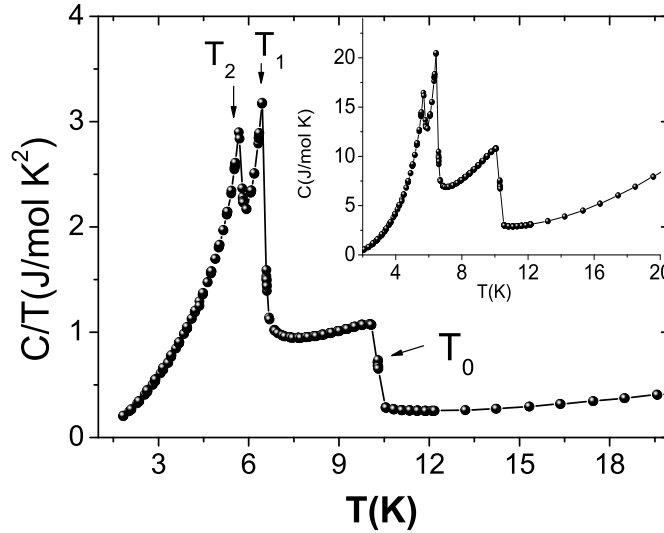


Figure 5.11: Temperature dependence of the heat capacity of single crystalline YbRu_2Ge_2 , in a plot C/T versus T showing the three transitions. Inset shows C versus T .

not increasing at this temperature, as would be expected for a Debye contribution. Thus, the specific heat results obtained on a polycrystalline sample indicate a complex ordering with three transitions at $T_0 \simeq 10$ K, $T_1 \simeq 6.5$ K and $T_2 \simeq 5.5$ K, as well as a magnetic entropy for above $R\ln 2$ at T_0 . These results are confirmed by the specific heat measurements on single crystals. Since these data have a much higher quality, single crystal shall be used for a detailed study of the properties of YbRu_2Ge_2 .

For the single-crystal C/T data (Fig. 5.11), the three transitions at $T_0 \simeq 10.2$ K, $T_1 \simeq 6.5$ K and $T_2 \simeq 5.7$ K are much sharper than in the polycrystalline sample. Furthermore, the anomaly at T_0 is much large with a step $\Delta C \simeq 9$ J/mol K, almost as large as $\Delta C \simeq 14$ J/mol K at T_1 (see inset of Fig. 5.11). All the features are well reproduced in different single crystals. The large size of the anomalies as well as

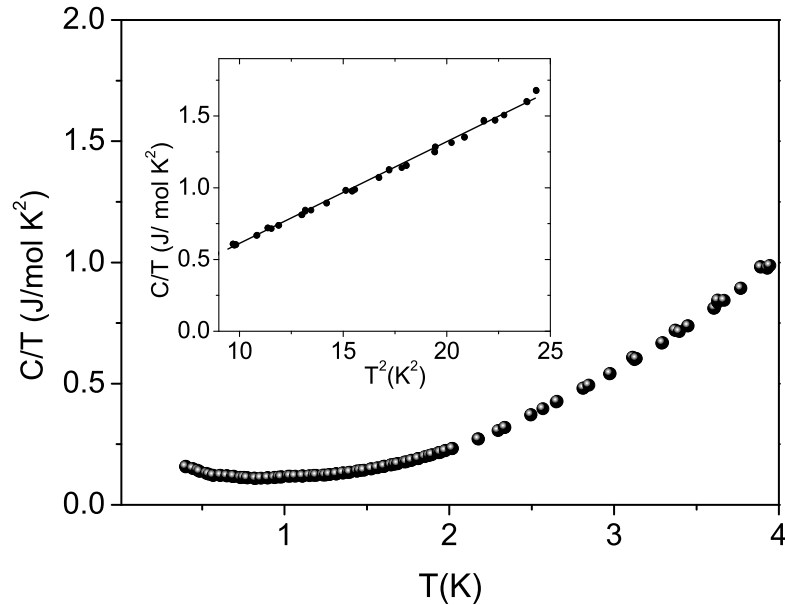


Figure 5.12: Low-temperature specific heat. Inset shows C/T versus T^2 .

their reproducibility prove that these three transitions are intrinsic. The transition T_0 resembles a mean-field like step, those at T_1 and T_2 show characteristics of a λ type transition.

In Fig. 5.12 we present the specific heat data at the lowest investigated temperatures in more details. Below 1.5 K, C/T converge towards a constant value. This linear term can be attributed with an enhanced Sommerfeld coefficient $\gamma \approx 100$ $\text{mJ/K}^2\text{mol}$. The slight upturn below 0.8 K might be either due to a nuclear Schottky contribution (due to Ru) or to a non-intrinsic contribution of defects or paramagnetic impurities. The decrease of C between 1 K and 3 K is much stronger than T^3 , indicating an excitation gap for the magnons. Such an excitation gap is expected from

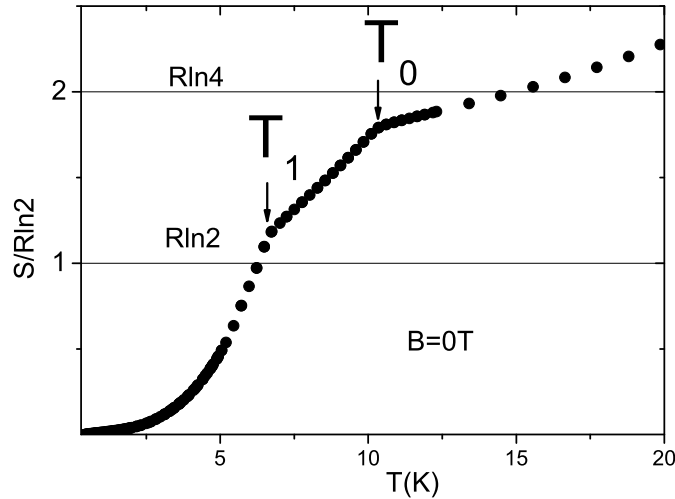


Figure 5.13: The temperature dependence of the entropy collected below 20 K.

the basal plane (and the c axis) anisotropy seen in the susceptibility.

YbRu_2Ge_2 seems to present the classical behavior of a magnetic trivalent Yb compound. The surprise came when we looked at the magnetic entropy $S(T)$, which we calculated by integrating the measured $C(T)/T$ up to 20 K (Fig.5.13). Because LuRu_2Ge_2 does not form, it was not possible to determine and subtract the phonon contribution to $C(T)$. However, for the calculation of $S(T)$ in the temperature range considered here ($T < 12$ K), the phonon contribution can be safely ignored because its contribution is negligible. As an example, the total entropy of the non-magnetic compound LuRh_2Si_2 at 12 K amounts to 0.17 J/mol K, less than 2 % of the total entropy we determined for YbRu_2Ge_2 at the same temperature. In a tetragonal environment, the crystal field splits the $J = 7/2$ state of Yb^{3+} into four Kramer doublets, with an energy spacing usually larger than 50 K. Thus only the lowest

doublet is relevant for the magnetic properties at low temperatures and one expects $S(T)$ close to $Rln2$ slightly above T_N . Our surprising result is that the magnetic entropy of $YbRu_2Ge_2$ just above the highest transition T_0 is much larger. It almost reaches $Rln4$. This result, which was reproduced with different samples, proves that in $YbRu_2Ge_2$ the first excited crystal field doublet is almost degenerated with the ground-state doublet. The excitation energy being less than 10 K (~ 1 meV). After our observation we looked in the literature [23], and found that for the homologue and isoelectronic compound $YbRu_2Si_2$, a CEF calculations based on an extrapolation of the CEF scheme of other RRu_2Si_2 compounds ($R =$ Rare earth) postulated a small excitation energy (25 K) for the first excited CEF level. However, there is up to now no experimental confirmation of such a low-level splitting in $YbRu_2Si_2$. Thus, our investigation reveals a very unusual quasi-quartet CEF ground state in $YbRu_2Ge_2$, which is unique among YbT_2X_2 compounds. More about CEF will be discussed in the context of the inelastic neutron experiment.

With this knowledge on the basic properties of $YbRu_2Ge_2$ we now discuss the effect of a magnetic field on the transitions. Fig. 5.14 shows C/T versus T for different magnetic fields, applied along hard c axis. All three transitions shift slightly to lower temperatures with increasing field, the shifts being roughly proportional to B^2 as demonstrated for T_1 in the inset of Fig 5.14. While T_0 and T_1 remain sharp and visible up to the highest investigated magnetic field ($B= 13$ T), T_2 disappears basically merging with T_1 between $B = 7$ T and 13 T.

The effect of a field along the [100] direction (easy plane) is much stronger than expected and differs strongly for T_0 and T_1 in comparison to fields along the [001] direction. T_1 is shifted to lower temperature with increasing field, down to 4 K at

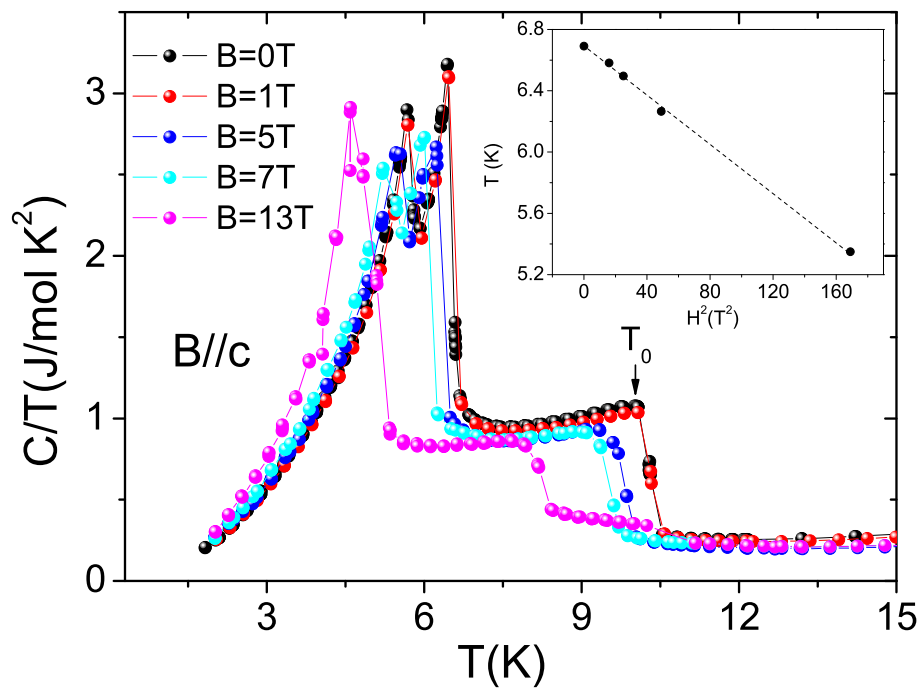


Figure 5.14: Temperature dependence of the heat capacity of YbRu₂Ge₂ in a plot C/T versus T for different fields applied along the c axis. Inset: T_1 versus B^2 .

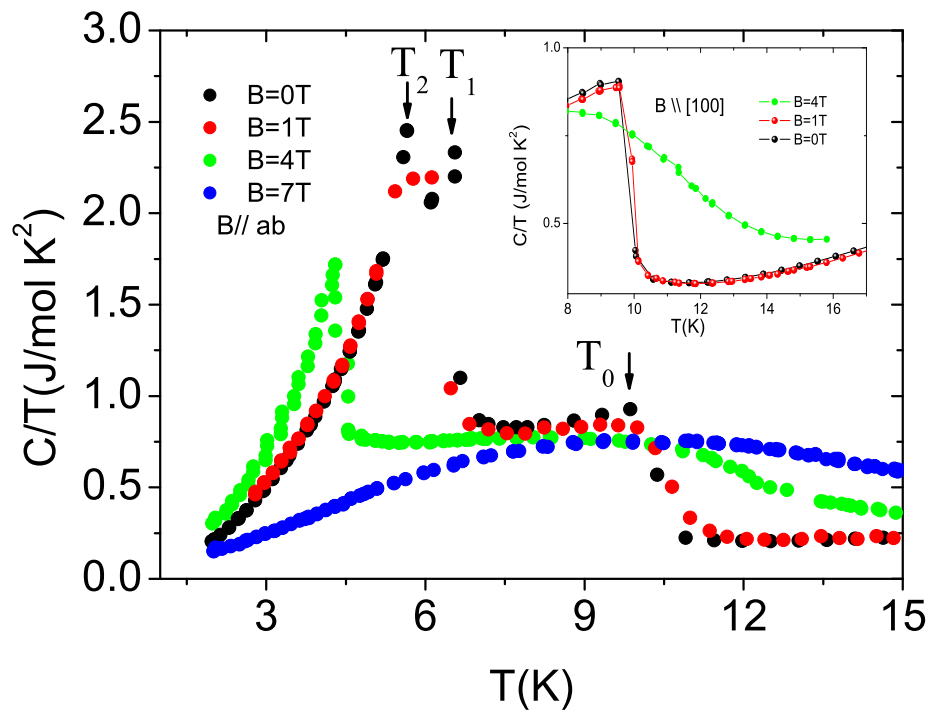


Figure 5.15: Field dependence of the phase transitions for fields applied along the $[100]$ axis in a plot C/T versus T for $B = 0\text{ T}$, 4 T , 7 T . Inset shows the region around T_1 in magnified scale.

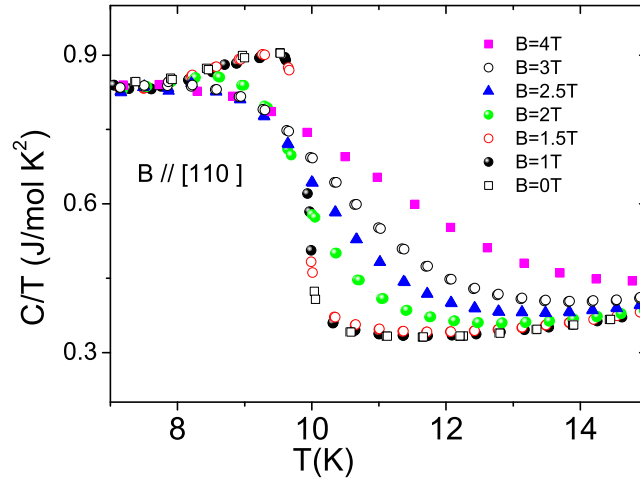


Figure 5.16: Field dependence of the specific heat anomaly at T_0 for fields applied along the [110] axis.

$B = 5$ T and to below 2 K at 7 T (Fig. 5.15), the shift being also roughly proportional to B^2 . By contrast, the upper transition T_0 shifts to higher temperatures with increasing field, up to 12 K at $B = 4$ T, and broadens. At 7 T, the specific heat reveals only a broad Schottky-like anomaly without signs of further transition. Fig. 5.16 shows more details on the field dependence of the T_0 anomaly for field applied along [110]. The transition remains unchanged up to a field of 1.5 T. Upon further increasing the magnetic field, the transition shifts to high temperatures and gets broad, similar to ferromagnetic transitions. The behavior along [100] is identical within the accuracy of the experiments (see inset of Fig. 5.15). In summary, a magnetic field applied along the hard c direction leads only to a small decrease of all the transition temperatures. By contrast, a magnetic field along the basal plane induces a rapid

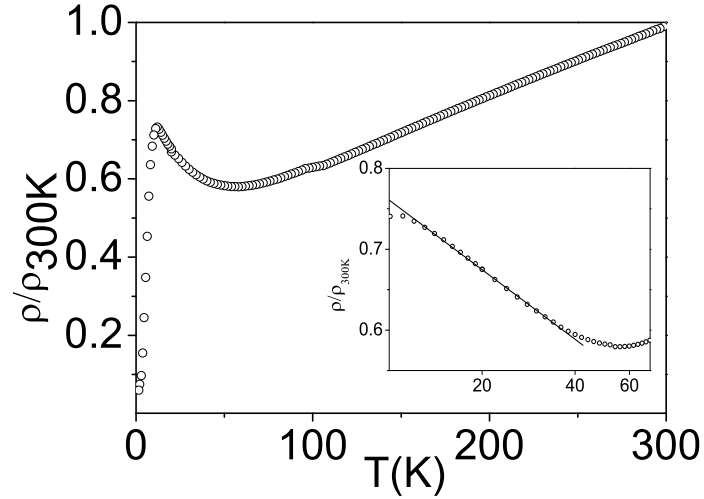


Figure 5.17: Temperature dependence of the resistivity normalized to its value at 300 K. Inset, normalized resistivity plotted on a logarithmic T scale in the temperature range $10 \text{ K} < 70 \text{ K}$.

decrease and disappearances of T_1 and T_2 , while T_0 becomes broader and shifts to higher temperatures for $B_{ab} > 1.5 \text{ T}$. The latter behavior is incompatible with a three dimensional antiferromagnetic ordering and more similar to that of a ferromagnetic transition, which, however, can be excluded from the absence of any strong anomaly in $\chi(T)$.

5.3.3 Resistivity of YbRu_2Ge_2

The temperature dependence of the resistivity normalized to room temperature is shown in Fig. 5.17. The resistivity was measured for current in the basal plane ($J//ab$). The resistivity ratio $\rho(300\text{K})/\rho(2\text{K}) = 22$ is an indicator for the good quality of the sample. The resistivity linearly decreases with temperature down to 70

K and shows a minimum around 50 K below which the resistivity starts to increase with decreasing temperature. This increase is sample dependent, in contrast to all other features in $\rho(T)$ which are very well reproducible. In the inset of the Fig 5.17 we plot the resistivity versus temperature in the range 10 K to 70 K, on a logarithmic temperature scale. Below 50 K down to 11 K (just before the transition) this increase of $\rho(T)$ is linear on a $\log T$ scale. Thus, while the decrease of $\rho(T)$ from 300 K down to 50 K indicates a metallic behavior, we tentatively attribute the increase below 50 K to weak Kondo-type interactions. In the inset of Fig 5.18, we show the detail of $\rho(T)$ at lower temperatures. At 10.2 K $\rho(T)$ exhibits a sharp break in the slope, from a negative one at $T > T_0$ to a positive one at $T < T_0$. The slope in $\rho(T)$ strongly increase further at $T_1 = 6.5$ K and only slightly more at $T_2 = 5.7$ K. Thus, all three transitions are also visible in the resistivity. The decrease in $\rho(T)$ below the transition, especially below T_1 , can be attributed to the freezing out of spin disorder scattering.

The main part of Fig. 5.18 shows the effect of a magnetic field (applied along the c axis) on $\rho(T)$ at low temperatures. The resistivity was measured in the temperature range between 2 K and 20 K under an applied magnetic field up to 14 T. The effect of the magnetic field on $\rho(T)$ is rather weak. Upon increasing field the phase transition anomalies shift to lower temperatures, in agreement with the specific heat results for $B \parallel c$. Even at 8 T there is a clear change in slope at each transition. Further increasing the field to 14 T shifts T_0 to 7.7 K and the magnetic transition to 5 K, but it is impossible to distinguish between T_1 and T_2 .

We also looked at the magnetoresistance at temperatures above the upper transition T_0 and below T_0 . Fig. 5.19 (upper part) shows the dependence of the resistivity

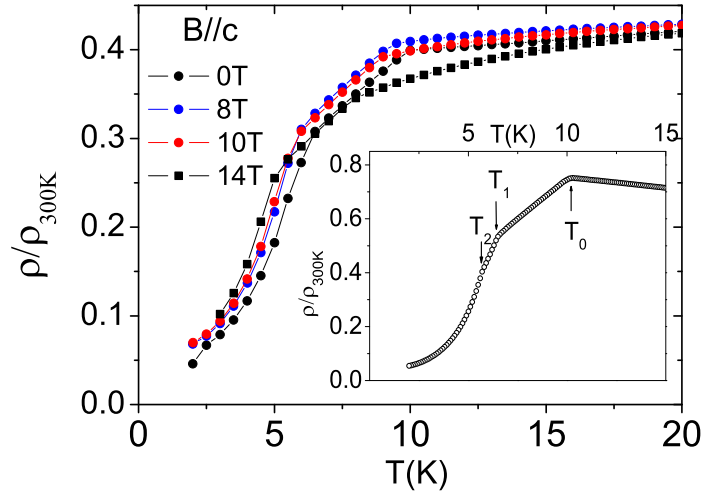


Figure 5.18: Temperature dependence (main part) of the resistivity normalized to its value at 300 K at different magnetic field ($B \parallel c$). The inset shows ρ from 2 K to 15 K. Kinks marked by arrows correspond to transitions at T_0 , T_1 and T_2 , respectively.

(normalized to its value at 300 K) on magnetic field applied along the c axis for temperatures between 12 K and 40 K. While the decrease of $\rho(B)$ at higher temperatures and higher fields can trivially be attributed to the reduction of spin disorder scattering, the slight increase observed at low temperature and low field is likely due to an increase of fluctuations because a field applied along c suppresses the ordering. A popular way to analyze the magnetoresistance in Kondo lattices is to plot the magnetoresistance (normalized with ρ at $B = 0$ and at the same temperature) as a function of an effective field $B^* = B/(T + T^*)$. We obtained a quite reasonable scaling with $T^* = 10$ K (lower part of the Fig. 5.19). T^* is a measure of the characteristic exchange interaction working against the magnetic field. Thus, this analysis indicates that the characteristic exchange energy scale in YbRu_2Ge_2 is of the order

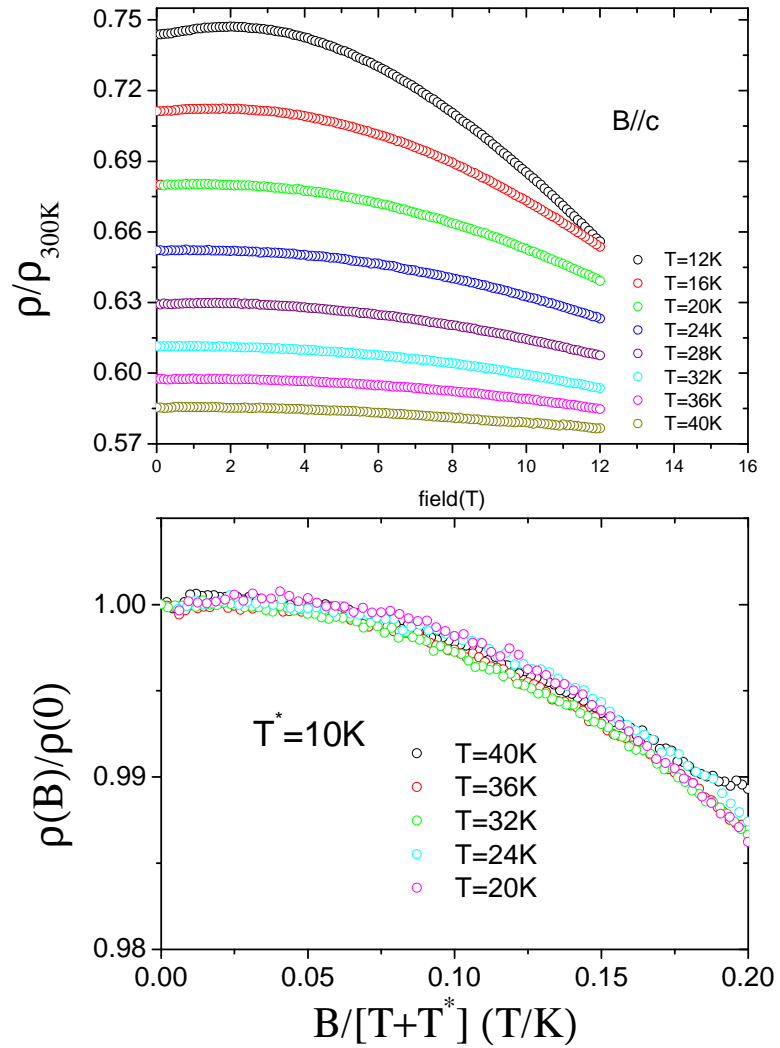


Figure 5.19: (a) Isothermal resistivity curves as a function of magnetic field measured at different temperatures above the transition T_0 . (b) Magnetoresistance versus $B/(T^* + T)$ for temperatures in the range 20 K to 40 K.

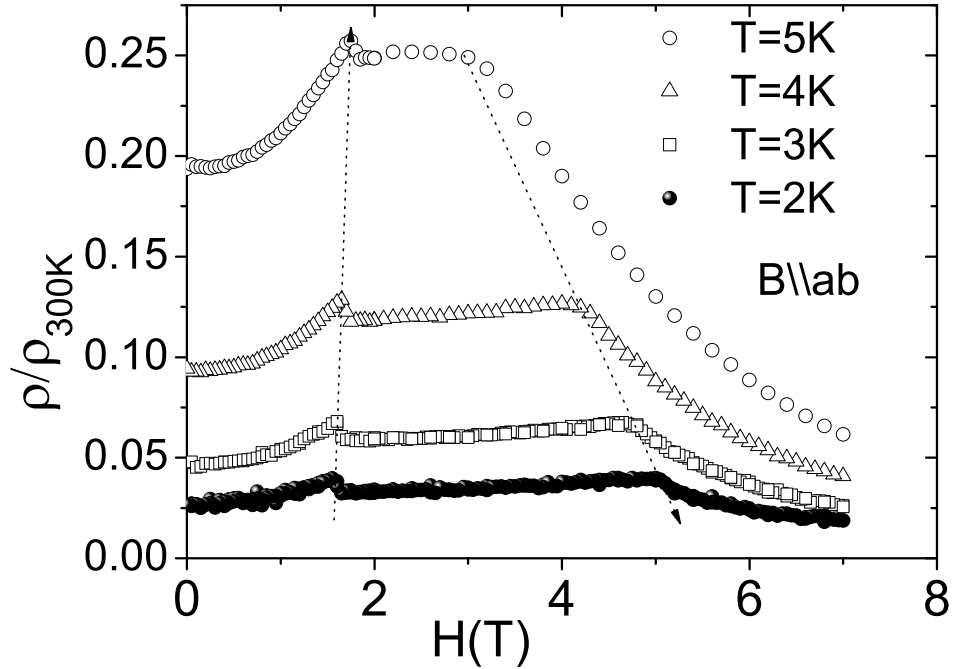


Figure 5.20: Magnetoresistance as a function of magnetic field along the basal plane measured below T_1 .

of 10 K. Fig. 5.20 shows the magnetoresistance plots as a function of magnetic field along the basal plane measured below T_1 . It shows two anomalies, one corresponding to the metamagnetic transition and another possibly due to $T_1(B)$ or $T_2(B)$. For example at 2 K, the clear anomaly at 1.6 T is due to the metamagnetic transition in agreement with the step observed in the magnetization. The anomaly at 5 T in the magnetoresistance at 2 K can be connected to one of the magnetic transition ($T_1(B)$ or $T_2(B)$), since it shifts to lower fields upon increasing temperature, in accordance to the results of the specific heat (see Fig. 5.15).

Interestingly, it turns out that there is a quite good correspondence between the

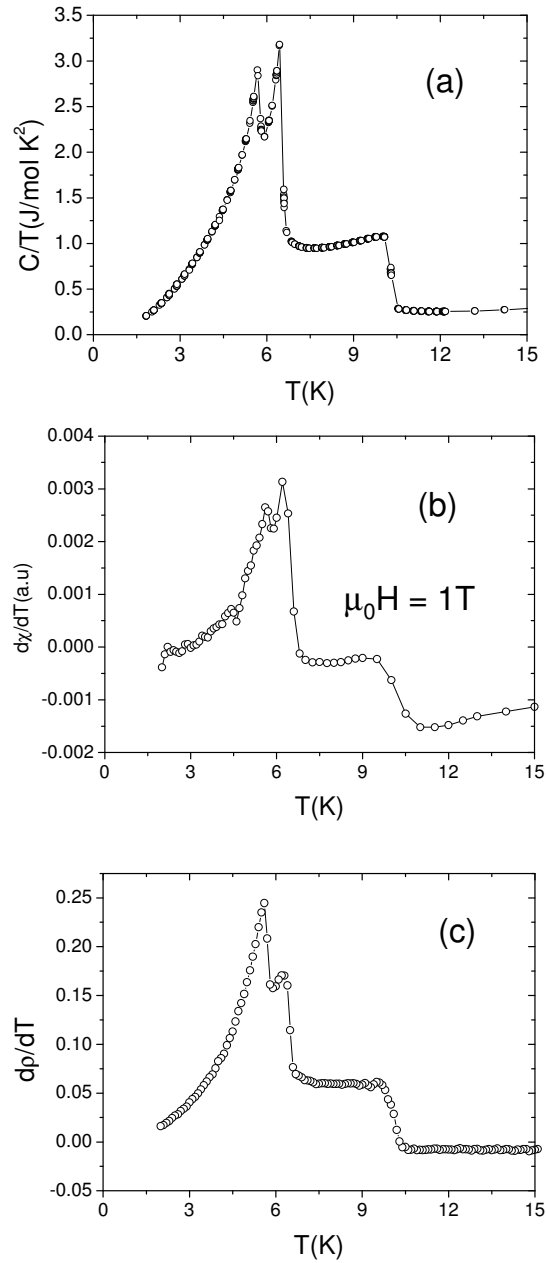


Figure 5.21: Comparisons between (a) C/T , (b) the derivative of the magnetic susceptibility $d\chi_c(T)/dT$ and (c) the derivative $d\rho(T)/dT$ vs. T .

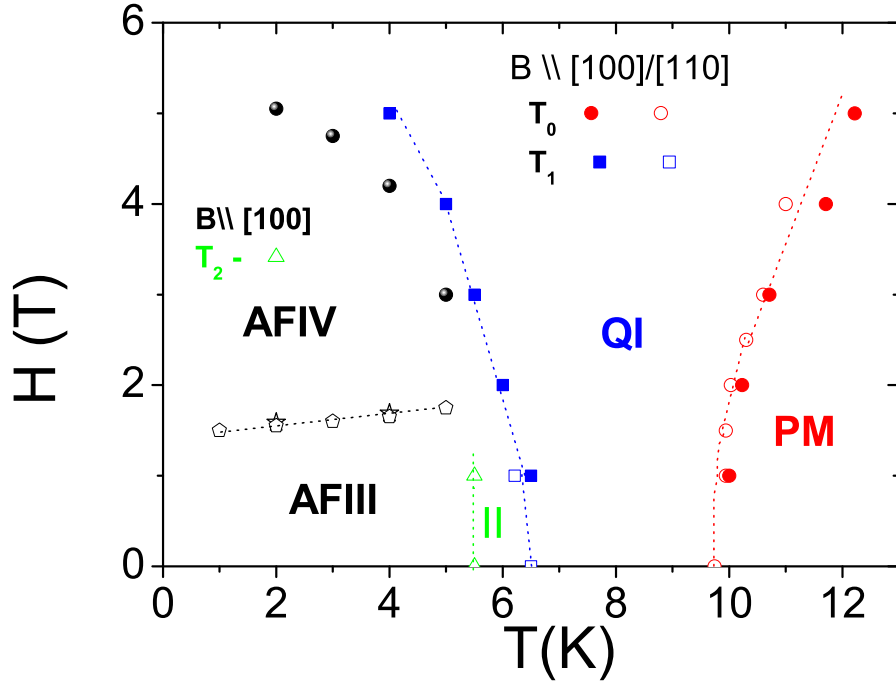


Figure 5.22: Magnetic $H - T$ phase diagram for applied magnetic fields along $[100]$ and $[110]$. Open circles, squares and triangles are taken from specific heat, closed circles and squares from magnetic susceptibility, stars from magnetization and open pentagons from magnetoresistance measurements.

temperature dependence of C/T , that of $d\rho(T)/dT$ and $d\chi_c(T)/dT$ in the temperature range between 12 K and 2 K. While some relations between $C(T)$ and $\chi(T)$ as well as between $C(T)$ and $\rho(T)$ have already been demonstrated and discussed in the literature [24], such a good, almost quantitative correspondence has rarely been observed.

The results obtained in the different measurements allow to draw the magnetic $H - T$ phase diagram. The partial $H - T$ phase diagrams of YbRu_2Ge_2 for the

magnetic field applied along the directions [100] and [110] are displayed in Fig. 5.22. The transition temperatures were determined from the specific heat, resistivity and magnetic susceptibility measurements. Open circles, squares and triangles are based on results from specific heat, closed circles and squares from derivative of magnetic susceptibility, stars from magnetization and open pentagons from magnetoresistance measurements, respectively. We can define four phases: QI, AFII, AFIII and AFIV. At the transition between the disordered paramagnetic phase and the Q1 phase we observe only a very weak signature in the susceptibility, a medium size anomaly in $\rho(T)$ but a large anomaly in $C(T)$ proving that it is a cooperative transition towards a long-range ordered state. Up to 1.5 T the transition remains unchanged while with further increasing field ($\parallel ab$) it shifts to higher temperatures and broadens. By contrast, the transition between QI and AFII behaves like an AF magnetic transition with a strong drop in magnetic susceptibility and a transition temperature shifting to lower temperatures with increasing the applied magnetic field. The metamagnetic transition between AFIII and AFIV is associated with only a small step in the magnetization compared to classical metamagnetic transition. The critical field $B = 1.6$ T increases only slightly with increasing temperature.

After the study of the bulk thermodynamic, transport and magnetic properties of YbRu_2Ge_2 , we report on neutron and μSR experiments. These measurements give a microscopic insight into the physics of this system and are, thus, complementary to the $C(T)$, $\rho(T)$ and $\chi(T)$ measurements performed in house.

5.4 Investigation of YbRu_2Ge_2 with μSR and Neutron scattering

The zero-field (ZF) μSR measurements were performed at the pulsed neutron and muon facility at ISIS (Rutherford Appleton Laboratory, UK), using the μSR spectrometer. In this spectrometer the sample was mounted into an Oxford Instruments Variox cryostat (1.2 K - 300 K). 100 % spin polarized muons with an energy of approximately 3.2 MeV are implanted in the sample. These muons come to rest rapidly (in 10^{-10}s), thermalize in the sample and then precess around the magnetic field at the muon site and subsequently decay into positrons [25, 26]. These positrons are emitted preferentially, along the spin direction of the muon at the time of decay. The neutron diffraction data were obtained on polycrystalline samples of YbRu_2Ge_2 with the 2-axis diffractometer D20 at the ILL reactor in Grenoble using neutrons with a wavelength 2.41 Å. The neutron measurements were performed at different temperatures between 2 K and 15 K in order to check all three transitions which were observed in other physical properties. For the confirmation of the crystallographic structure and the determination of magnetic structures Rietveld refinements of the powder diffraction data were carried out with the program FullProf using the atomic scattering factors provided by the program for the neutron wavelength [28].

5.4.1 Zero field muon spin measurements

Fig. 5.23 shows the time dependence of the muon polarization spectra taken from polycrystalline samples of YbRu_2Ge_2 . Fig. 5.23 has six curves which were collected at different temperatures, 15 K (above all the transitions), 8.5 K (below T_0), 6.25

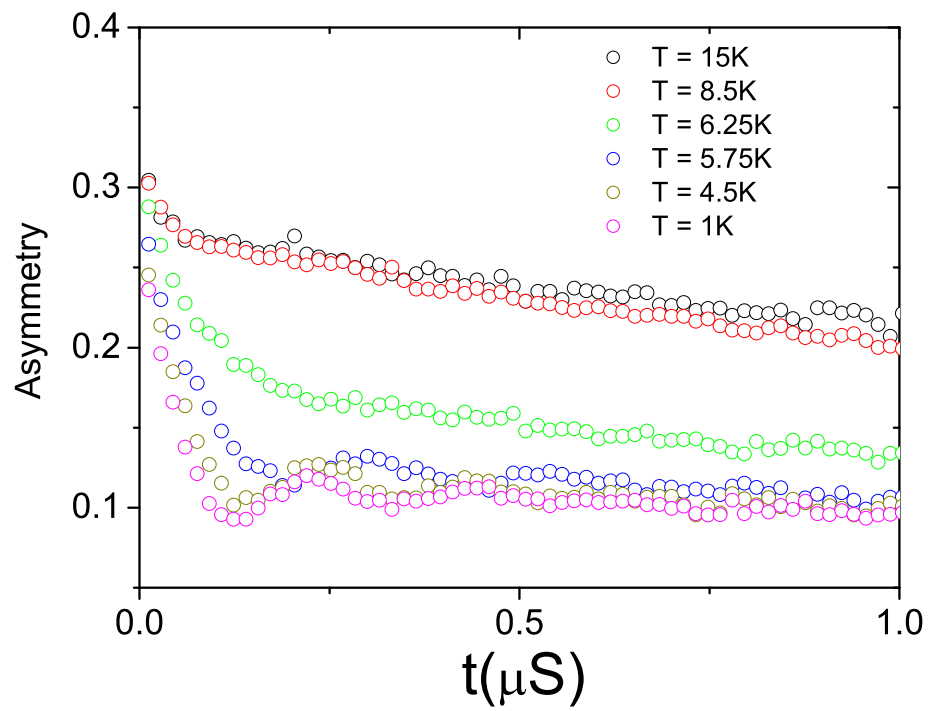


Figure 5.23: μ SR spectra of YbRu_2Ge_2 collected at different temperatures, showing very small depolarization rate at 15 K and 8 K, but strong depolarization with coherent oscillations below 6.25 K.

K (below T_1), 5.75 K (below T_2) and 2 K (below all three transitions). The 15 K spectrum which is in the paramagnetic region shows very weak muon depolarization rate due to fluctuating Yb and nuclear moments. At 8.5 K, which is below the transition at 10 K (the suspected quadrupolar phase) the depolarization rate has only very slightly increased reflecting a minor increase in the fluctuation of the Yb 4f moments. This is a strong evidence for the absence of magnetic order at 8.5 K. However, at 6.25 K and lower temperatures the results evidence a strong depolarization rate with coherent oscillations indicating long-range magnetic ordering.

Above T_1 , the μ SR polarization signal $G(t)$ is found to be composed of two exponentially relaxing components A_2 and A_3 . These two parameters are proportional to the relative amount of muons contributing to the respective behavior. Thus, in this temperature region, $G(t)$ can be fitted with equation

$$G(t) = A_2 \exp(-\lambda_2 t) + A_3 \exp(-\lambda_1 t) + C \quad (5.4.1)$$

where C accounts for the time-independent background. Below T_1 a further term representing the spontaneous muon Larmor precession in the internal field due to the ordered state has to be included. Thus, in the magnetically ordered states the following equation has to be used.

$$G(t) = A_1 \frac{\sin(wt + P)}{(wt + P)} + A_2 \exp(-\lambda_2 t) + A_3 \exp(-\lambda_1 t) + C \quad (5.4.2)$$

w is the precession frequency due to the local magnetic field, A_1 is again an asymmetry parameter and P is related to the position of the detector. Fig. 5.24 and Fig. 5.25 show an example for a fit above T_1 and below T_1 , respectively.

The temperature dependence of the most relevant fit parameters is shown in Fig.

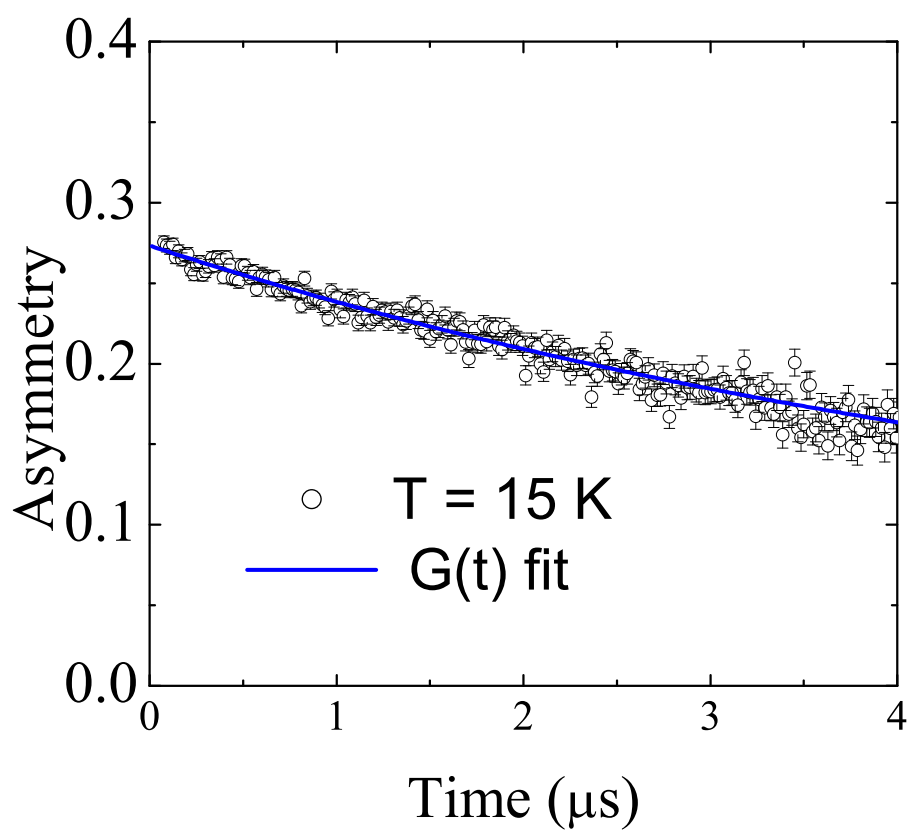


Figure 5.24: Zero-field muSR spectrum collected in the paramagnetic region with the solid line representing the fit.

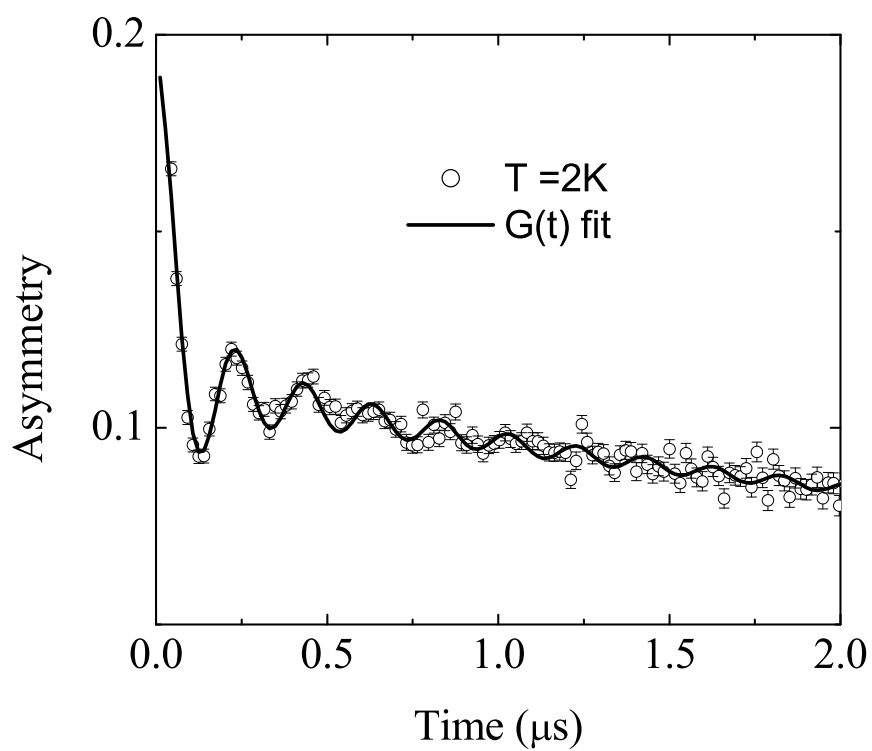


Figure 5.25: Zero-field muSR spectrum (open circles) collected at 2 K below all three transitions with the fit (solid line).

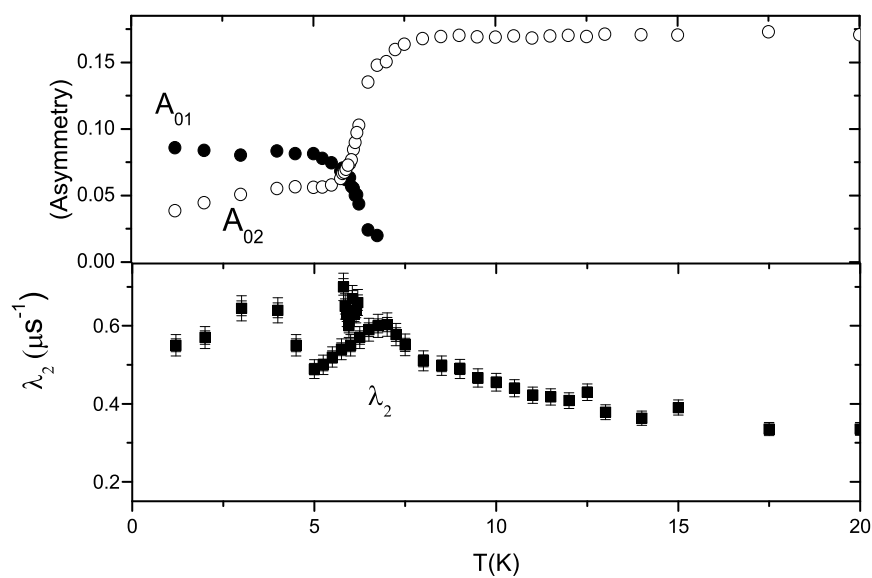


Figure 5.26: (a) Temperature dependence of the amplitudes of the asymmetries components. The amplitudes are associated with the paramagnetic A_2 and magnetic A_1 volume fractions. (b) Temperature dependence of relaxation rates λ_2 .

5.26. The asymmetry parameter A_2 , which is proportional to the paramagnetic volume fraction, is constant above 8K, but decreases steeply near T_1 and stays constant below 5 K. Simultaneously A_1 corresponding to the volume fraction increases steeply below T_1 and saturates below 5 K. This is a direct evidence for the onset of magnetic order below T_1 . The relaxation rate λ_2 of the paramagnetic part A_2 increases slightly and continuously decreasing with temperature from 50 K (not shown) to T_1 , without showing any anomaly near T_0 . This is a strong indication that T_0 is not associated with magnetic ordering. Just above T_1 , λ_2 shows the beginning of a divergence, as commonly observed above a magnetic transition. Below T_1 , λ_1 stays approximately constant (not shown) but with a large scattering likely due to the smaller A_2 . The origin of the small amount of paramagnetic signal evidence by A_2 below T_1 is yet not clear. The same problem applies for the real second paramagnetic contribution connected with A_3 (not shown), which shows a small, temperature-independent relaxation rate λ_1 (not shown) in the whole temperature range (also below T_1), but a small decrease of A_3 below T_1 . A possible origin might be a contribution from the sample holder. The X-ray diffraction pattern of the powder used for these μ SR measurements did not show a sufficient amount of impurity phases to account for the quite large contribution A_3 .

The precession frequencies ω of the muon is proportional to the internal field at the muon site, which in turn is proportional to the size of the ordered magnetic moment. Thus, the T dependence of ω (inset of Fig. 5.27) traces the evaluation of the staggered magnetization. ω increases very strongly below T_1 , shows a kink at T_2 , and saturates below 4 K. Thus, the temperature dependence of ω confirms both the onset of magnetic order at T_1 and a change in magnetic structure at T_2 .

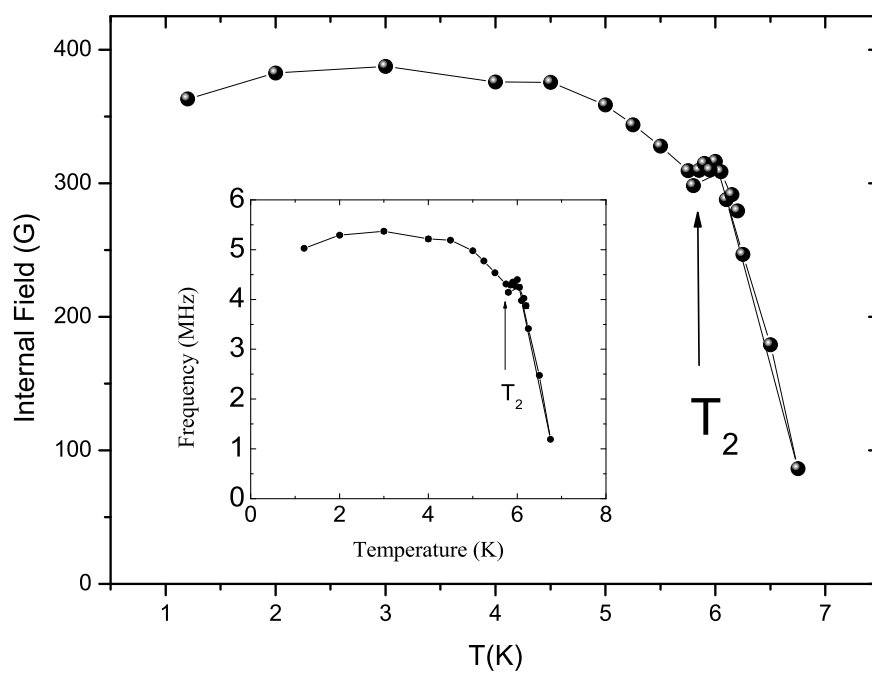


Figure 5.27: Temperature dependence of internal magnetic field at the muon site. Inset shows the muon precession frequency.

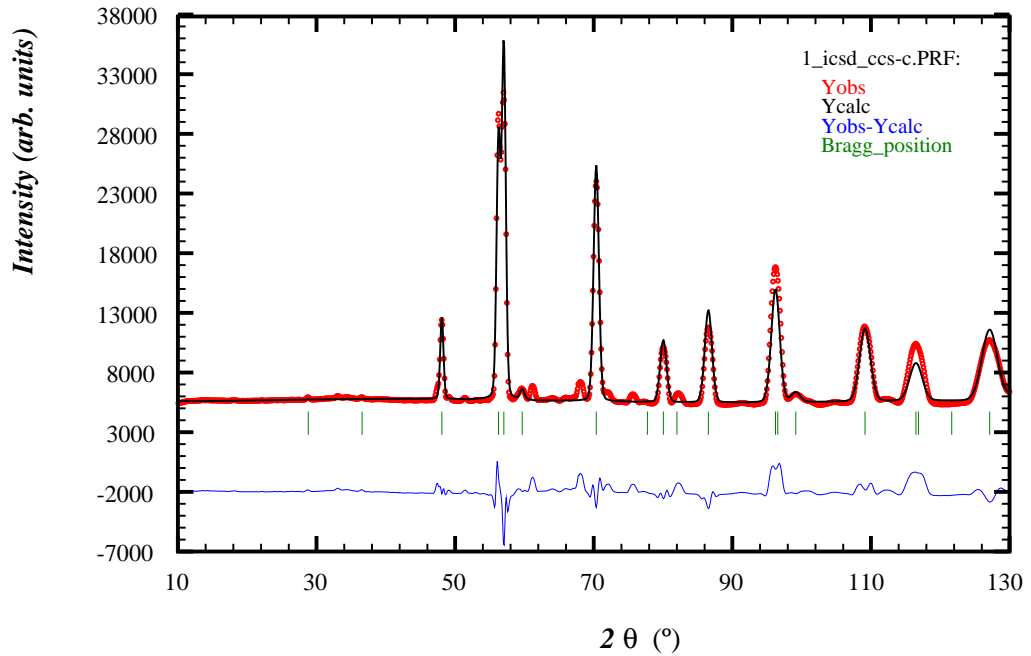


Figure 5.28: Neutron-diffraction pattern of YbRu_2Ge_2 recorded at 8 K above the magnetic phase transition (points) together with the best fit (the full line). The full line at the bottom represents the difference between the experimental data and the fit and the vertical lines are the position of expected nuclear Bragg peaks.

5.4.2 Neutron diffraction

In order to investigate the nature of the magnetic phases, neutron diffraction patterns were obtained at different temperatures from 15 K (paramagnetic region) down to 2 K (well below the three transitions). All diffraction patterns were taken in zero applied magnetic field. Fig. 5.28 shows the neutron-diffraction pattern recorded at 8 K, where only nuclear peaks of YbRu_2Ge_2 are visible. The refinement of the 8 K spectrum confirms the ThCr_2Si_2 structure with lattice parameters $a = 4.190$ (10) Å and $c = 9.710$ (20) Å. The blue line represents the difference between the

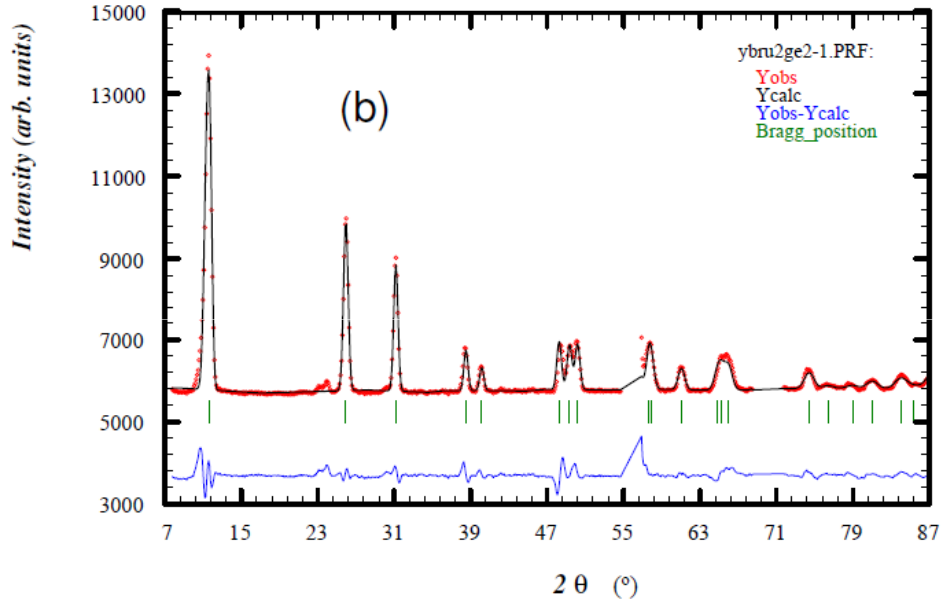


Figure 5.29: Magnetic diffraction pattern of YbRu_2Ge_2 at 2 K, obtained by subtracting the spectrum collected at 12 K from the spectrum collected at 2 K after appropriate scaling. The marks at the bottom denote peak positions expected for propagation $q = (0.3516, 0, 0)$.

experimentally measured intensity and the theoretically calculated pattern while the vertical lines represents the expected peak positions. The absence of changes between the diffraction patterns at high temperatures (not shown) and at 8 K indicates that there is no large lattice distortions at 10 K. Below T_1 , additional diffraction peaks appear, a direct proof for the onset of antiferromagnetic order. We first determine the magnetic structure at 2 K.

To separate the magnetic Bragg peaks we subtracted the diffraction pattern collected at 15 K from that collected at 2 K, after appropriate scaling. The difference

shown in Fig. 5.29 evidences intense Bragg peaks due to the antiferromagnetic ordering of the Yb sublattice. The difference pattern at 2 K is characterized by the satellite peaks at positions which do not coincide with reciprocal lattice points of either the chemical cell or any simple multiple of the chemical unit cell. All the new reflections of magnetic origin could be indexed assuming a propagation vector $q = (0.3516, 0, 0)$, which indicates an incommensurate magnetic order at 2 K. With this propagation vector we could perform a complete fit of the magnetic diffraction pattern. The solid line in Fig. 5.29 shows the fit for the propagation vector $q = (0.3516, 0, 0)$. The vertical lines mark the positions of the expected magnetic Bragg peaks for this propagation vector, and the bottom line shows the difference between the experimental and calculated patterns. The fit provides evidence that the Yb moments are aligned in the basal plane, along the $[010]$ direction. The ordered magnetic moment is found to be $3.95 \mu_B$ per Yb ion at 2 K. All the magnetic Bragg peaks disappear at 7.4 K, and a long time measurement at 8.0 K shows no extra peaks other than nuclear ones confirming that there is no magnetic ordering at 8.0 K, in agreement with μ SR measurements.

In order to check for the T_2 transition we plot the intensity of the magnetic peaks versus temperature. Fig. 5.30 shows the intensity of the first three strong magnetic peaks as a function of temperature. The magnetic intensity appears at around 7.5 K. This corresponds to the onset of magnetic order and is consistent with the broader anomaly observed around T_1 in specific heat measurements of polycrystalline sample. The intensity increases smoothly with temperature, without an anomaly at T_2 (5.5 K). However we found a very small change in the position of these peaks at 5.5 K (not shown here), which suggests that there might be a small change in the propagation

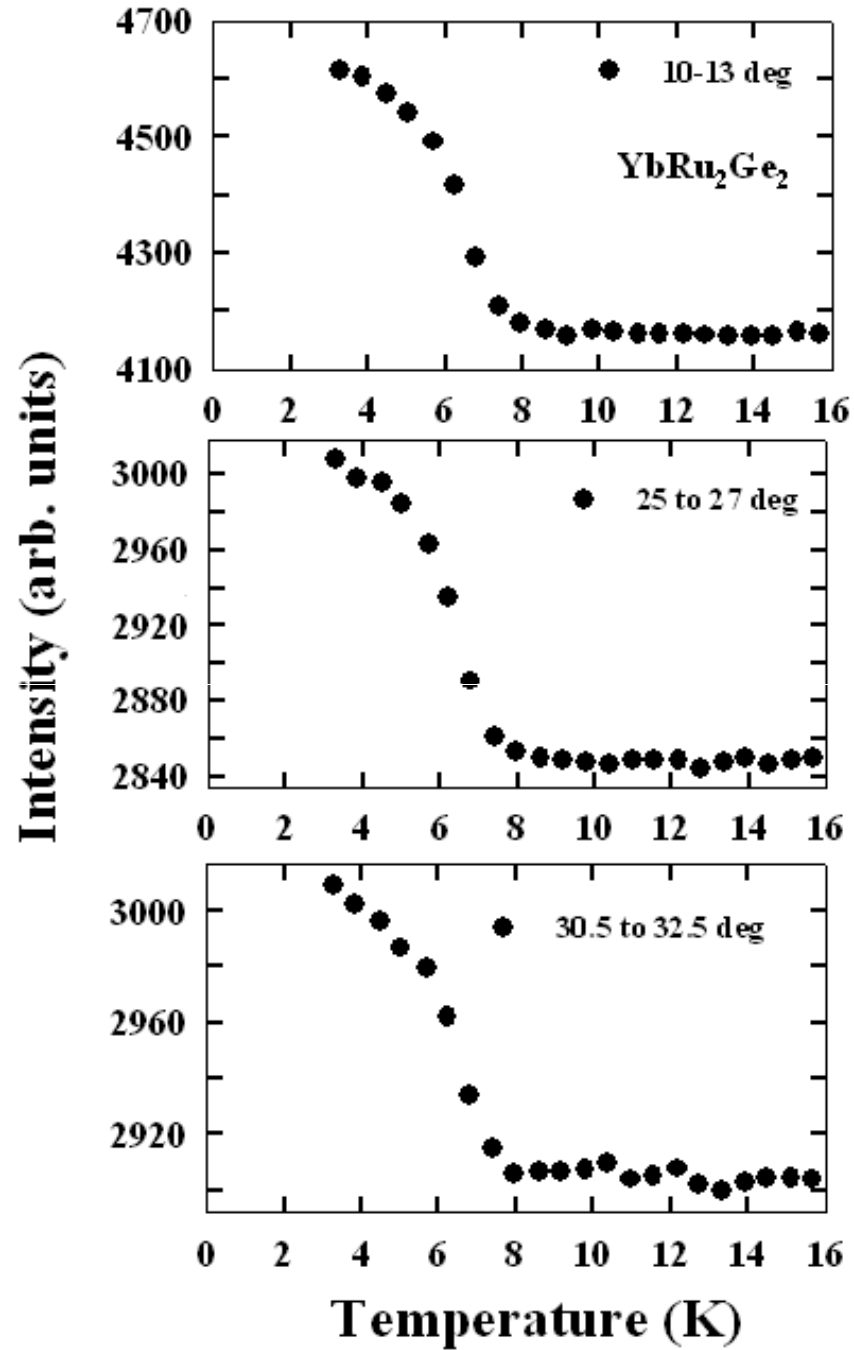


Figure 5.30: The integrated intensity of the first three strong magnetic peak as a function of temperature.

vector.

The determined magnetic structure of YbRu_2Ge_2 at 2 K is shown in Fig. 5.31. The magnetic moment of the Yb atoms are oriented perpendicular to the c axis in agreement with the anisotropy found in the magnetic susceptibility, and perpendicular to the propagation vector. They form an incommensurate antiferromagnetic phase.

In summary, both the results of the muon spin rotation and neutron diffraction experiments confirm the onset of long-range magnetic order below T_1 and the absence of such order between T_1 and T_0 . The magnetic structure below T_1 could be determined from the neutron diffraction experiment. It corresponds to an incommensurate structure with propagation vector $Q_{AF} = (0.3516, 0, 0)$. and a large ordered moment $\mu_{AF} = 3.95 \mu_B$ aligned perpendicular to Q_{AF} within the basal plane. The change in the magnetic structure at T_2 could not be resolved in the neutron diffraction experiments. This change is likely rather small, as evidenced by only a small kink at T_2 in the temperature dependence of the muon precession frequency. Thus further experiments are needed in order to clarify the change at T_2 , as well as whether the propagation vector remains incommensurate down to lowest temperature.

5.4.3 Inelastic Neutron Scattering

From the entropy of $\text{Rln}4$ collected in the specific heat below 14 K, it was clear that the crystal electric field ground (CEF) state is a quasi quartet. In order to study the CEF scheme of YbRu_2Ge_2 we did inelastic neutron scattering experiment at HET (ISIS) and IN6 (ILL). Magnetic excitations can be distinguished from phonon excitations through their temperature dependence and momentum transfer dependence. For

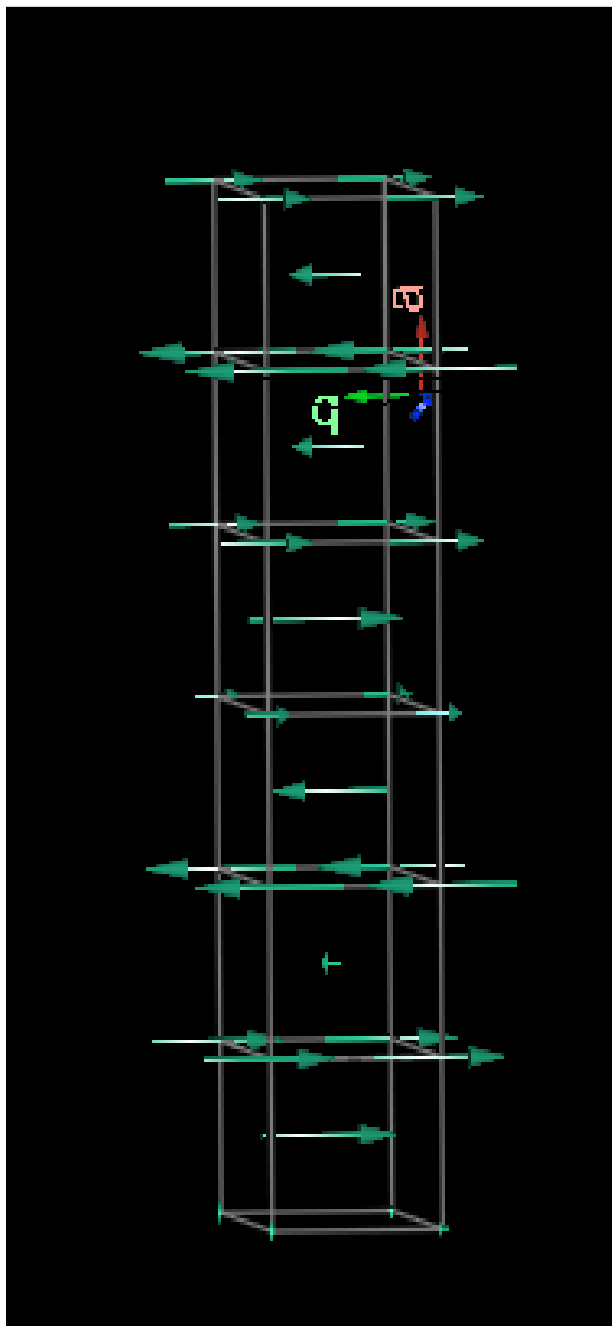


Figure 5.31: Proposed magnetic structure of YbRu_2Ge_2 at 2 K.

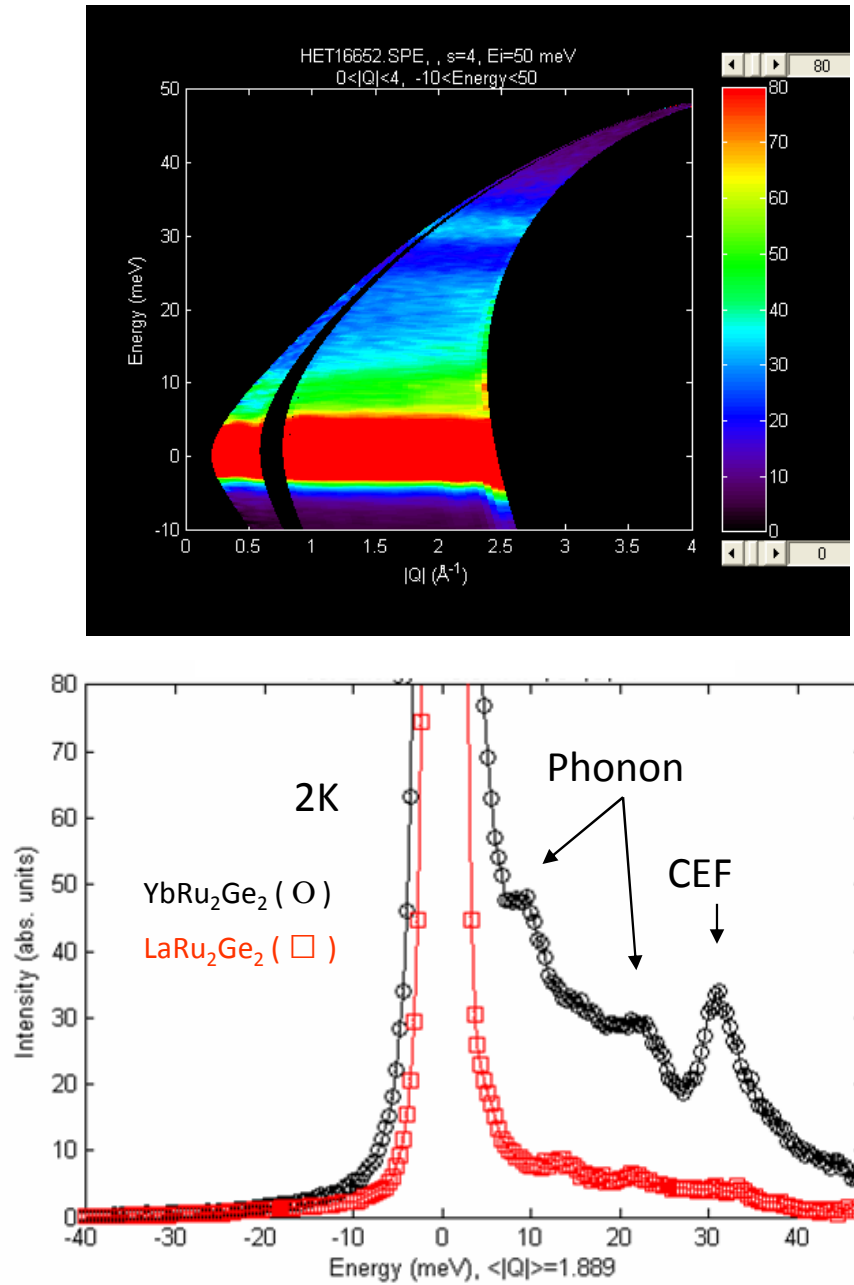


Figure 5.32: Upper part shows the raw data for YbRu₂Ge₂ with the Q and energy-dependence at 2 K. Only one well defined crystal field excitation is observed at 32 meV. Lower part compares the inelastic spectra of YbRu₂Ge₂ and LaRu₂Ge₂ at 2 K.

that purpose additional inelastic neutron experiments were also performed on non-magnetic LaRu_2Ge_2 (LuRu_2Ge_2 does not form) to check the phonon contribution. Both YbRu_2Ge_2 and LaRu_2Ge_2 powder samples were loaded in Al foil.

In the tetragonal ThCr_2Si_2 structure type, all Yb sites are equivalent. The magnetic susceptibility and specific heat confirm that in YbRu_2Ge_2 the Yb ion is in a stable $3+$ state. Then one expects the CEF to split the $J = 7/2$ multiplets into four doublets. Accordingly one would in general expect to observe three crystal-field excitations in the inelastic neutron scattering spectra at low temperatures. As mentioned earlier, in the isostructural compounds YbRh_2Si_2 three excitations have indeed been observed in the inelastic neutron scattering at 17 meV (first excited level), 25 meV (second excited level) and 43 meV (third excited level) [21].

Fig. 5.32 (lower part) shows the neutron spectra of YbRu_2Ge_2 and LaRu_2Ge_2 at $T = 2$ K for incoming energy $E = 50$ meV. The upper part of Fig. 5.32 shows the raw data of the Q dependence. A direct subtraction of a nonmagnetic spectra is not possible because the Lu compound does not form and the mass difference (thus the difference in phonon frequency) between La and Yb is too large.

There is a clear strong excitation at 32 meV and two further weak excitations at lower energy. An analysis of the Q dependence of these data indicates that only the peak at 32 meV corresponds to a magnetic excitation, while the other structures in the plot correspond to the phonon contribution [27]. This suggests that the third excited CEF level is at a much higher energy while the first excited level is at lower energy, within the quasi elastic line as expected from the specific heat.

Using the information from the entropy that the first excited CEF state lies below 10 K (1 meV) and locating the second excited level at 32 meV based on inelastic

⇒ preliminary CEF-scheme

———— Γ_6 91 meV

———— Γ_7 32 meV

===== Γ_7 0.9 meV
 ===== Γ_6 0 meV

- Ground state

$$0.99 \cdot |1/2\rangle + 0.08 \cdot |-7/2\rangle$$

- First excited state

$$0.98 \cdot |3/2\rangle - 0.15 \cdot |-5/2\rangle$$

Figure 5.33: Preliminary CEF scheme of YbRu_2Ge_2 .

neutron measurements. M. Rotter [32] analyzed the strong anisotropy in the magnetic susceptibility, and performed a first estimation of the CEF scheme of YbRu_2Ge_2 with Mcphase [29]. Fig. 5.33 shows the deduced preliminary CEF scheme, which gives a Γ_6 as the ground state and a Γ_7 as the first excited state, close to the ground state with a separation of only 0.9 meV. While the second excited level is a Γ_7 at 32 meV, the third one (Γ_6) is at much higher energy, around 91 meV. Despite the anisotropy of the magnetic susceptibility it is similar in YbRu_2Ge_2 and YbRh_2Si_2 , the CEF schemes are quite different. However, the CEF scheme of YbRu_2Ge_2 is somewhat similar to that proposed for YbFe_2Ge_2 , where also a first excited CEF level at a rather low energy $\Delta \simeq 2.3 \text{ meV} \sim 26 \text{ K}$ has been suggested. The total number of valence electrons in YbRu_2Ge_2 and YbFe_2Ge_2 is the same, thus one can expect similar CEF scheme in both compounds.

5.5 Discussion and Conclusion

The presence of a quasiquartet CEF ground state is a unique situation among Yb-based compounds crystallizing in the ThCr_2Si_2 structure type. With such a quasiquartet CEF ground state and taking into account the anomalous behaviour of T_0 , like large specific heat anomaly contrasting an extremely weak anomaly in $\chi(T)$, quadrupolar ordering becomes more relevant and has to be considered. For the transition at T_1 , the situation is rather simple: the strong decrease of $\chi_{ab}(T)$ and $\chi_c(T)$ below T_1 indicate that this transition corresponds to antiferromagnetic ordering, as confirmed by neutron and μSR experiments. As a consequence, the transition at T_2 is likely related to a change of the magnetic structure. By contrast, for T_0 the situation is less clear. At first we note that T_0 is larger than the highest magnetic ordering temperature reported up to now in intermetallic Yb compounds, which is $T_N = 7.5$ K in $\text{Yb}_3\text{Cu}_4\text{Ge}_4$ [30]. The absence of a visible anomaly in the easy plane susceptibility at T_0 , despite a large mean-field like anomaly in $C(T)$ and a weak anomaly in the susceptibility along the hard direction, is unusual for a pure magnetic ordering. Also the increase of T_0 for fields along the easy direction is not expected for an antiferromagnetic transition in a three-dimensional system. By contrast, these results correspond to the behavior expected for quadrupolar ordering. As an example, our observations in YbRu_2Ge_2 are almost identical to those reported for TmAu_2 , where the upper transition was revealed to be ferroquadrupolar ordering. The behavior we observe at T_0 and the similarities with TmAu_2 strongly suggest that the transition at T_0 in YbRu_2Ge_2 corresponds to quadrupolar ordering. While for some compounds of the rare-earth elements quadrupolar ordering is quite common, there is no well established example for quadrupolar ordering in a Yb-based compound.

As discussed in the introduction, the claim of a mixing type quadrupolar order in YbSb is controversial, while the claim for such an order in YbAl_3C_2 was proven to be inappropriate. One of the main problem is that there was up to now no example for a Yb compound with a stable trivalent magnetic Yb and a quartet CEF ground state. Thus, YbRu_2Ge_2 likely presents a unique type of ordering among Yb compounds. Our results might also have some consequences for the interpretation of the unusual properties of YbRh_2Si_2 .

Finally, we discuss the partial $H - T$ phase diagram. From the phase diagram (Fig. 5.22) it is clear that there are three ordered phases in zero magnetic field and at least one more at higher field. All the zero applied magnetic-field transitions were observed in both polycrystalline samples as well as in single crystals. A small difference in transition temperature were detected because the transition is quite broad in polycrystalline samples, but sharp in single crystals. Polycrystalline samples were synthesized using a solid-state synthesis route which possibly induces more disorder in the sample. The strong drop of magnetic susceptibility measurements in single crystals at T_1 corresponds to AF ordering and accordingly this transition shifts to lower temperatures upon increasing the magnetic field. The same applies also for the transition at T_2 . By contrast, T_0 presents a very different field dependence, T_0 shifts to higher temperatures with increasing magnetic field along the easy basal plane but it shifts to the low-temperature side when the field is applied along the hard c axis. Recently, motivated by our results on YbRu_2Ge_2 , Takimoto and Thalmeier [31] proposed a mean field model for YbRu_2Ge_2 based on a quasi-quartet ground state. They could reproduce both the $H - T$ phase diagram as well as the anomalies observed in the susceptibility, magnetization and specific heat. In this model T_0 indeed

corresponds to ferroquadrupolar order, and T_1 to additional magnetic order.

Recent thermal expansion measurements on YbRu_2Ge_2 also support quadrupolar ordering at 10 K [32]. In zero magnetic field one observes strong changes in the thermal expansion measured along c direction at the ordering temperature $T_0 = 10$ K. Upon applying a magnetic field along the basal plane, the temperature where the thermal expansion displays this strong change in the slope increases. For magnetic fields larger than 2 T this 10 K anomaly becomes broad and finally disappears.

In conclusion, we have investigated the physical properties of YbRu_2Ge_2 compound by means of susceptibility, specific heat and resistivity measurements. The susceptibility is strongly anisotropic, being much larger for fields in the basal plane than along the c direction. For fields along the easy plane $\chi_{ab}(T)$ follows a Curie-Weiss law with an effective moment close to the value for free Yb^{3+} , while for fields along the hard direction the curve $1/\chi_c(T)$ versus T shows a strong negative curvature indicating a large overall CEF splitting. The temperature dependence of the resistivity follows a standard metallic behavior above 50 K and shows a weak Kondo type increase below 50 K. At lower temperatures, anomalies in $C(T)$, $\rho(T)$ and $\chi(T)$ evidence three successive phase transitions at $T_0 = 10.2$ K, $T_1 = 6.5$ K and $T_2 = 5.7$ K, T_0 being larger than the highest Yb-magnetic ordering temperature observed up to now in intermetallic Yb compounds. Just above T_0 , the magnetic entropy calculated from the specific heat reaches almost $R\ln 4$ instead of $R\ln 2$ as expected for a CEF ground-state doublet. The large anisotropy of the susceptibility, the Curie Weiss behavior of $\chi(T)$ along the easy plane, the large magnetic entropy collected at low temperatures and the weakness of the Kondo like increase in $\rho(T)$ demonstrate that Yb is in a stable trivalent state. $S(T \geq T_0) \approx R\ln 4$ proves that the energy

of the first CEF excited doublet is lower than 10 K, leading to a quasiquartet CEF ground state, a unique situation among Yb compounds. The shape of the anomalies at T_0 in $\chi(T)$ and its behavior in a magnetic field are unusual for magnetic ordering, but very similar to those reported at the ferroquadrupolar ordering in TmAu_2 . In view of the quasiquartet CEF ground state, this strongly suggests the transition at T_0 to be of quadrupolar ordering. By contrast, the strong decrease of $\chi(T)$ at T_1 indicates antiferromagnetic ordering, while the transition T_2 is likely related to a change in the magnetic structure. The combination of a quasiquartet CEF ground state, a high ordering temperature and the likely relevance of quadrupolar interactions makes YbRu_2Ge_2 a very interesting system among Yb-based compounds. Neutron diffraction and μSR experiments were performed in order to reveal the nature of the different transitions. Both experiments confirm magnetic order below T_1 and its absence above T_1 , supporting quadrupolar ordering as origin for the transition at T_0 . The neutron scattering allowed the determination of the magnetic structure at 2 K as an incommensurate magnetic structure with the propagation vector $Q_{AF} = (0.3516, 0, 0)$ and a large ordered moment of $\mu_{AF} = 3.95 \mu_B$ aligned perpendicular to Q_{AF} within the basal plane.

Bibliography

- [1] T. Onimaru, T. Sakakibara, K. Aso, H. Yoshizawa, H. Suzuki, and Y. Takeuchi, Phys. Rev. Lett. **94**, 197201 (1995).
- [2] K. Hirota, N. Oumi, T. Matsumura, H. Nakao, Y. Wakabayashi, Y. Murakami, and Y. Endoh, Phys. Rev. Lett. **84**, 2706 (2000).
- [3] T. Yanagisawa, T. Goto, Y. Nemoto, S. Miyata, R. Watanuki, and Y. Suzuki, Phys. Rev. B **67**, 115129 (2003).
- [4] M. Kosaka, H. Onodera, K. Ohoyama, M. Ohashi, Y. Yamaguchi, S. Nakamura, T. Goto, H. Kobayashi, and S. Ikeda, Phys. Rev. B **58**, 6339 (1998).
- [5] P. Morin, and J. Rouchy, Phys. Rev. B **48**, 256 (1993).
- [6] F. J. Ohkawa, J. Phys. Soc. Jpn. **54**, 3909 (1985).
- [7] T. Suzuki, T. Komatsubara, K. Kunii, H. Kasuya, and Y. Ohtsuka, Solid State Communications **35**, 569 (1980).
- [8] A. Yamamoto, J. Takeda, T. Koyama, T. Mito, S. Wada, I. Shirotnani, and C. Sekine, Phys. Rev. B **70**, 220402 (2004).

- [9] M. Kosaka, Y. Kato, C. Araki, N. Mri, Y. Nakanishi, M. Yoshizawa, K. Ohoyama, C. Martin, and S. W. Tozer, *J. Phys. Soc. Jpn.* **74** 2413 (2005).
- [10] O. Akira, I. Takaki, M. Takeshi, O. Akira, K. Kenichi, *J. Phys. Soc. Jpn.* **74**, 123703 (2007).
- [11] P. Haen, J. Flouquet, F. Lapierre, P. Lejay, and G. Remenyi, *J. Low Temp. Phys.* **67**, 779 (1987).
- [12] T. Sakakibara, T. Tayama, K. Matsuhira, H. Mitamura, H. Amitsuka, K. Maezawa, and Y. Onuki, *Phys. Rev. B* **51**, R12030 (1995).
- [13] R. Movshovich, T. Graf, D. Mandrus, J. D. Thompson, J. L. Smith, and Z. Fisk, *Phys. Rev. B* **53**, 8241 (1996).
- [14] O. Trovarelli, C. Geibel, S. Mederle, C. Langhammer, F. M. Grosche, P. Gegenwart, M. Lang, G. Sparn, and F. Steglich, *Phys. Rev. Lett.* **85**, 626 (2000).
- [15] S. Paschen, T. Lühmann, S. Wirth, P. Gegenwart, O. Trovarelli, C. Geibel, F. Steglich, P. Coleman, and Q. Si, *Nature* **432**, 881 (2004).
- [16] Z. Hossain, C. Geibel, F. Weickert, T. Radu, Y. Tokiwa, H. S. Jeevan, P. Gegenwart, and F. Steglich, *Phys. Rev. B* **72**, 94411 (2005).
- [17] M. Francois, G. Venturini, J. F. Mareche, B. Malaman, and B. Roques, *J. Less comm. Metal* **113**, 231 (2005).
- [18] H. S. Jeevan, Z. Hossain and C. Geibel, *Phys. Rev. B* **73**, 779 (2006).
- [19] F. M. Schappachera, K. Katohb, R. Poettgen, *Journal of Solid State Chemistry* **180**, 186 (2007).

- [20] J. Ferstl, F. Weickert and C. Geibel, *Journal of Magnetism and Magnetic Materials* **272-276**, e71 (2004).
- [21] A. Hiess, O Stockert, M. M. Koza, Z. Hossain, and C. Geibel, *Physica B* **378-380**, 748 (2006).
- [22] O. Stockert, M. M. Koza, J. Ferstl, A. P. Murani, C. Geibe, F. Steglich, *Physica B* **378-380**, 157 (2006).
- [23] R. Michalski, A. Blaut, R. J. Radwanski, *Acta Physica Polonica B* **34**, 1565 (2003).
- [24] See e.g. J. C. P. Campoy, E. J. R. Plaza. A. A. Coelho and S. Gama, *Phys. Rev. B* **74**, 134410 (2006).
- [25] A. Schenck, in *Muon Spin Rotation* (Hilger, Bristol, 1985).
- [26] *Muon Science: Muons in Physics, Chemistry and Materials* (ed S.L. Lee, S.H. Kilcoyne and R. Cywinski) (Pub: Scottish University Summer School and IOP) 1998.
- [27] Adroja et al. to be published.
- [28] <http://www.ill.eu/sites/fullprof/>
- [29] M. Rotter, *Journal of Magnetism and Magnetic Materials* **272-276**, e481 (2004).
- [30] S. K. Dhara, S. Singha, P. Bonville, C. Mazumdar, P. Manfrinetti, A. Palenzon, *Physica B* **312-313**, 846 (2002)
- [31] T. Takimoto and P. Thalmeier, *Phys. Rev. B* **77**, 045105 (2008).

[32] M. Rotter et al., to be published.

Chapter 6

Summary and Conclusions

In summary, in the first part of this work we report on the successful synthesis of single crystals of CeCu_2Si_2 with precise ground-state properties and with the masses up to 5 g. We found a clear relation between the ground state and the residual resistivity ratio, which reflects the disorder in the system. The magnetic susceptibility for different types of single crystals shows a small but systematic dependence, being largest for A type and smallest for the S type. The electronic specific heat clearly demonstrates four different ground states with a broader and smaller anomaly in A-type CeCu_2Si_2 due to a magnetic transition and a sharper and much larger anomaly in S type due to a superconducting transition. C/T just above the transition is larger in A-type single crystals and smallest for S-type, indicating an increase of the Kondo scale from A to S type. This increase in C/T is also in agreement with the results of pressure measurements. The low-temperature resistivity shows non-Fermi liquid behavior above T_N or T_c with an almost linear temperature dependence below 3.5 K. The exponent in the power law decreases from S to A type and is slightly larger for current in the basal plane than for current along c axis. The most important result is that our large single crystals allowed for the first time the successful observation of the magnetic

Bragg peaks in A-type single crystals. This proved that the A phase is nothing but a long-range incommensurate antiferromagnetic phase with a propagation vector (0.21 0.21 0.54). In AS-type single crystals, the long-range magnetic order competes with the superconducting phase, i.e., the magnetic order becomes suppressed by the superconducting phase. Interestingly, short-range magnetic correlation coexists with the superconducting phase in S-type single crystals. First inelastic neutron experiments show a possible relation between the superconducting and magnetic phases evidenced by the formation of a spin excitation gap in the magnetic excitation spectra at the antiferromagnetic propagation vector below T_c .

We also performed the single-crystal growth and detailed investigations of $\text{CeCu}_2(\text{Si}_{1-x}\text{Ge}_x)_2$. Here, the 2 % Ge-doped single crystals show competing SC state with $T_c = 0.5$ K and AFM state with $T_N = 0.7$ K, the former one expelling the later one below T_c , as in pure, undoped CeCu_2Si_2 single crystals of A/S type. By contrast, bulk SC was up to now only observed in one of 10% Ge-doped single crystals. However, the SC state in 10% Ge-doped CeCu_2Si_2 seems to be even more sensitive to the stoichiometry and defects than in the undoped CeCu_2Si_2 . The present studies leave many questions still open, but gives some ideas for improvement. Thus, further studies both on the growth and on the physical properties of 5 % to 10 % Ge-doped single crystals are necessary to get a deeper insight into the regime where SC and AFM state coexist.

In the second part of the thesis we have synthesized both polycrystals and single crystals of YbRu_2Ge_2 and investigated the physical properties of this compound by means of susceptibility, specific heat and resistivity measurements. The susceptibility is strongly anisotropic, being much larger for fields in the basal plane than along the c direction. The temperature dependence of the resistivity follows a standard

metallic behavior above 50 K and shows a weak Kondo-type increase below 50 K. At lower temperatures, anomalies in $C(T)$, $\rho(T)$ and $\chi(T)$ evidence three successive phase transitions at $T_0 = 10.2$ K, $T_1 = 6.5$ K and $T_2 = 5.7$ K, T_0 being larger than the highest magnetic ordering temperature observed up to now in intermetallic Yb compounds. Just above T_0 , the magnetic entropy calculated from the specific heat reaches almost $R\ln 4$ instead of $R\ln 2$ expected from the CEF ground-state doublet. The large anisotropy of the susceptibility, the Curie Weiss behavior of $\chi(T)$ along the easy plane, the large magnetic entropy collected at low temperatures and the weakness of the Kondo-like increase in $\rho(T)$ demonstrate that Yb is in a stable trivalent state. $S(T \geq T_0) \approx R\ln 4$ proves that the energy of the first CEF excited doublet is lower than 10 K, leading to a quasiquartet CEF ground state, a unique situation among YbT_2X_2 compounds. The shape of the anomalies at T_0 in $\chi(T)$ and its behavior in a magnetic field are unusual for magnetic ordering, but very similar to those reported for ferroquadrupolar ordering. In view of the quasiquartet CEF ground state, this strongly suggests the transition at T_0 to be quadrupolar ordering. By contrast, the strong decrease of $\chi(T)$ at T_1 indicates antiferromagnetic ordering, while the transition T_2 is likely related to a change in the magnetic structure. Further experiments need to confirm the quadrupolar phase transition, e.g., ultrasonic measurements. However, at present the single crystal are not big enough to perform such experiments.

In order to investigate the nature of various phases, neutron diffraction patterns were obtained at different temperatures from 15 K (paramagnetic region) down to 2K (much below the three transitions). All diffraction patterns were taken in zero applied magnetic field. Refinement of the 8 K spectrum confirms the crystal structure of

YbRu₂Ge₂ to be of the ThCr₂Si₂ type tetragonal structure. The spectrum measured at 2 K clearly shows new peaks corresponding to magnetic order. All new reflections which are of magnetic origin can be indexed by a propagation vector $q = (0.3516, 0, 0)$, which suggests an incommensurate magnetic order below 2 K. The magnetic moment per Yb ion is found to be $3.95 \mu_B$ at 2 K. All magnetic Bragg peaks disappear at 7.4 K and even after data collection at 8.0 K for a very long time, we did not detect any signs of magnetic Bragg peaks. This suggests that the phase transition at 10 K is not associated with magnetic order which is consistent with the μ SR data.

Above T_1 , the zero-field muon spectra can be best described with a single exponential relaxation rate plus a small time-independent background, which implies no magnetic order found above T_1 . Below T_1 , the μ SR spectra require an additional oscillating term, which indicates magnetic order. The magnetic volume fraction at T_1 shows a sharp increase and saturates below 5 K. From the precession frequencies ω one can get the internal magnetic field at the muon site and the temperature dependence of the precession frequencies. It is clear that muon precession starts at the magnetic transition (T_1) and increases further at lower temperatures. This component reflects the development of a magnetic field at muon site below T_1 . The calculated muon-site magnetic field below 5 K is $\simeq 375$ G. Furthermore, there is a clear change in the precession frequencies at T_2 associated with the rearrangement of the spin directions in the magnetic structure at 5.5 K.

The inelastic neutron scattering experiments suggest a clear excitation at 32 meV and two further weak excitations at lower energy. An analysis of the Q dependence of these data indicate that only the peak at 32 meV corresponds to a magnetic excitation. We did not observe more magnetic excitations. Possibly further excitations occur at

very high energy (above 600 K) and at lower energy (<1 meV), which both are consistent with our physical properties.

Acknowledgements

I would like to thank Prof. Dr. F. Steglich for giving me the opportunity to do my doctoral work at the Max Planck Institute for Chemical Physics of Solids in Dresden.

I don't have any word to thank my supervisor, Dr. Christoph Geibel, I learned a lot from him both knowledge of physics and crystal growth technique. and I thank him for everything he has done for me. Especially for the large amount of work he has put into thoroughly reading my thesis.

A special thanks to Dr. M. Deppe for introduced me for all kind of instruments and for all discussion. I am fortunate to work with many nice people in our group, Dr. Z. Hossain, N. Caroca-Canales, Dr. J. Ferstl, Dr. E. Kaul, Dr.N. Kini, Dr. R. Nath, H. Diem, R. Wise, Dr.C. Krellner and A. Jesche .

I have enjoyed many discussions and fruitful collaborations with colleagues, Dr. O. stockert, Dr. E. Lengyel, Dr. T. Nakanishi, Dr. M. Nicklas, Dr. J. Arndt, R. Borth and Dr. T. Cichorek. I Extend my thanks to Dr. D.T. Adroja, Dr. A. D. Hillier and Dr. E. Faulhaber. I would like to express my gratitude to Dr. Ulrich Burkhardt and Petra Scheppan for the EDXS measurements.

I must thank all my friends, Prashanth, Ramesh, Deepa, Shankar, Golden, Nabhinda, Surjeet, Manoj, Micha, Julia, Monica, Edit, Franziska, Corneliu, Stefan, Pradeep, Akash, Sahana, Enrique, Gabriel and Niels.

A special thanks to all administrative and technical staff of the institute for their help. I am very thankful to K. Demian, C. Strohbach and K. Klein for all the help during my stay in Dresden.

I am very gratefull to my parents, my sister and my wife for there constant support and understanding.

Author's declaration

I declare that the work presented in this dissertation was carried out in accordance with the regulations of the Technology University of Dresden. No part of this work has been submitted previously for a degree or other qualification at this or any other university. The research reported herein is original, except where specific reference is acknowledged to the work of others. All the research was carried out under the supervision of Prof. Dr. Frank Steglich and Dr. Cristoph Geibel in Max-Planck-Institute for Chemical Physics of Solids.

Hirale S. Jeevan
Dresden, Germany
27th. October 2010

Versicherung

Hiermit versichere ich, dass ich die vorliegende Arbeit ohne unzulässige Hilfe Dritter und ohne Benutzung anderer als der angegebenen Hilfsmittel angefertigt habe; die aus fremden Quellen direkt oder indirekt übernommenen Gedanken sind als solche kenntlich gemacht. Die Arbeit wurde bisher weder im Inland noch im Ausland in gleicher oder ähnlicher Form einer anderen Prüfungsbehörde vorgelegt.

Die vorliegende Dissertation wurde unter die Betreuung von Prof. Dr. Frank Steglich und Dr. Cristoph Geibel am Max-Planck-Institut für Chemische Physik fester Stoffe in Dresden angefertigt. Ich erkenne die Promotionsordnung an.

Hirale S. Jeevan
Dresden, Deutschland
27th. October 2010